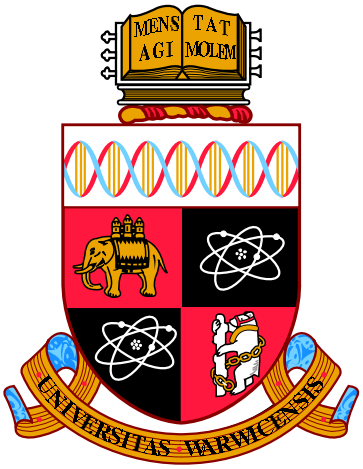

Atomic Structure Study of Pyrochlore Ytterbium Titanate

by

Ali Mostaed

Thesis

Submitted to the University of Warwick

for the degree of

Doctor of Philosophy

Department of Physics

April 2017

THE UNIVERSITY OF WARWICK

Contents

List of Tables

List of Figures

Acknowledgments

Writing this thesis was one of the most significant experiences I have had in my academic life. It is therefore important to extend my gratitude to those whose patience, understanding and support made the completion of this work possible.

First, I thank Dr. Richard Beanland for his encouragement, understanding and counsel. I am particularly grateful for the many hours he has spent with me over the past four years, providing me with valuable comments and feedback on my work.

Also, thank you to Prof. Geetha Balakrishnan, my second supervisor, who has guided and supported me throughout the whole PhD process.

There were other academics who have also helped me through: Dr. Ana Sanchez, for all the lessons in TEM and Dr. Martin Richard Lees, for teaching me so much about frustrated magnetism; as well as Dr. Neil Wilson and Dr. Jeremy Sloan.

I also greatly appreciate the support from the technicians: Steve York and Steve Hindmarsh, whose trainings were really fruitful.

I have benefited from many friends during the past four years: Mazdak Hashempour, Amir Ghalamzan, Mohammad Kalouti, Sahar Salehi, Reza Kashtiban, Jonathan Peters, Samuel Marks, Zachary Laker, Alex Hubert, Alex Marsden, Adam Dyson, Dawn Wood, Mark Skilbeck, Thomas Ward, Kerrie Smith, Grace Wood, Natalie Teutsch, James Gott, Charlie Slade, Xue Xia, Houari Amari and Aruni Fonseka as well as the many others (Nessa, Negin, Soroush, Habib, among many more).

And a big thank you to my family whose consistent support enabled me to concentrate on my studies throughout my PhD. My mum, dad and brother, Ehsan, without whose selfless and generous support I would not have been able to reach this stage of my academic life.

And finally to my wife, Saeede, whose enduring understanding and support, particularly in the final year, taught me about unconditional love and sacrifice; thank you. I dedicate this to her.

Declarations

I declare that the work presented in this thesis carried out by the author under the supervision of Dr. Richard Beanland and Prof. Geetha Balakrishnan at the Department of Physics, University of Warwick. Some of this work presented in chapter 3 has been previously published by author in the following publication:

- A. Mostaed, G. Balakrishnan, M. R. Lees, Y. Yasui, L. J. Chang, and R. Beanland. Atomic structure study of the pyrochlore $Yb_2Ti_2O_7$ and its relationship with low-temperature magnetic order. *Physical Review B*, 95:094431, 2017.

Abstract

There has been great interest in the magnetic behaviour of pyrochlore oxides with the general formula $A_2B_2O_7$, in which rare-earth (A), and transition metal (B) cations are ordered on separate interpenetrating lattices of corner-sharing tetrahedra. Such materials exhibit behaviours including quantum spin-ice, (quantum) spin-liquid, and ordered magnetic ground states. $Yb_2Ti_2O_7$ lies on the boundary between a number of competing magnetic ground states. Features in the low-temperature specific heat capacity that vary in sharpness and temperature from sample to sample suggest that in some cases the magnetic moments order, while in others the moments remain dynamic down to temperatures as low as $\sim$16 mK. In this work, three different $Yb_2Ti_2O_7$ single crystal samples, all grown by the optical floating zone technique but exhibiting quite different heat capacity behaviour, are studied by aberration-corrected scanning transmission microscopy (STEM). Atomic-scale energy-dispersive X-ray (EDX) analysis shows that a crystal with no specific heat anomaly has substitution of Yb atoms on Ti sites ("stuffing"). In fact, EDX analysis shows for the first time that "stuffing" of Yb (A) cations onto Ti (B) sites in the lattice can be observed directly in the pyrochlore structure. Moreover, I show that the detailed intensity distribution around the visible atom columns in annular dark field STEM images is sensitive to the presence of nearby atoms of low atomic number (in this case oxygen) and find significant differences between the samples that correlates both with their magnetic behaviour and measurements of Ti oxidation state using electron energy loss spectroscopy. These measurements support the view that the magnetic ground state of $Yb_2Ti_2O_7$ is extremely sensitive to disorder. On the other hand, structural modification of ytterbium titanate by deviation from stoichiometry as well as electron irradiation is studied in this work. I show that Ti excess is accommodated by Yb cation vacancies while Yb excess is compensated by Yb interstitials. Furthermore, two MATLAB programs, Detect_Columns and BurgersVectors, to analyse STEM images and calculate the dislocation density tensor of STEM images as well as their Burgers vector(s) are respectively introduced in this work.

Abbreviations

ABF annular bright-field.

ac-STEM aberration-corrected scanning transmission electron microscopy.

ac-TEM aberration corrected transmission electron microscopy.

ADF annular dark-field.

ADF-STEM annular dark-field scanning transmission electron microscopy.

AES Auger electron spectroscopy.

BF bright-field.

BF-STEM bright-field scanning transmission electron microscopy.

CBED convergent beam electron diffraction.

CEND coherent electron nano-diffraction.

CL core-loss.

CTEM conventional transmission electron microscopy.

EDX energy dispersive X-ray spectroscopy.

EELS electron energy loss spectroscopy.

ELNES electron energy loss near-edge structure.

EPWF exit plane wave function.

FCC face-centred cubic.

FEG field-emission gun.

FWHM full width at half maximum.

GPA geometric phase analysis.

HAADF high-angle annular dark-field.

HL high-loss.

HRTEM high-resolution transmission electron microscopy.

LAADF low-angle annular dark-field.

LL low-loss.

MAADF medium-angle annular dark-field.

PCTF phase contrast transfer function.

PIPS precision ion polishing system.

SAD selected area diffraction.

SAM scanning Auger microscopy.

SEM scanning electron microscopy.

SES secondary electron spectroscopy.

STEM scanning transmission electron microscopy.

TDS thermal diffuse scattering.

TEM transmission electron microscopy.

VLM visible-light microscopes.

ZLP zero-loss peak.

Nomenclature

C_S the spherical-aberration coefficient.

E the initial kinetic energy of electron.

T_m the maximum transferred energy.

Z the atomic number.

Λ the inelastic mean free path.

α the probe convergence semi-angle.

β the collection semi-angle.

β_I the inner angle of the ADF detector.

β_O the outer angle of the ADF detector.

$\boldsymbol{\varepsilon}$ the two-dimensional local strain field.

λ the wavelength of radiation.

μ the refractive index of the viewing medium.

$\boldsymbol{a}$ the dislocation density tensor.

$\boldsymbol{b}$ the Burgers vector.

$\boldsymbol{e}$ the two-dimensional local distortion field.

$\boldsymbol{g}$ the reciprocal lattice vector.

$\boldsymbol{u}$ the displacement field.

θ_B the Bragg diffraction angle.

c the light speed in vacuum.

e the unit electron charge.

h the Planck constant.

m_0 the rest mass of electron.

t the specimen thickness.

Chapter 1

Introduction

The atomic structure of pyrochlore ytterbium titanate has been studied in this thesis. Results presented in this work have increased our understanding of the nature of mysterious magnetic behaviour of $Yb_2Ti_2O_7$ at low temperatures as well as formation of defects in the pyrochlore structure. Ytterbium titanate samples studied in this work were synthesised at the department of physics of University of Warwick and the department of physics of Meiji University, Japan. In addition, heat capacity measurements as well as electron microscopy investigations presented in this work were performed at the department of physics of University of Warwick.

In this chapter I will first provide information about the pyrochlore structure and its relationship with low-temperature magnetic order. I will then continue by introducing several electron microscopy techniques which are used for characterization of materials at the atomic scale. The procedures used for sample preparation as well as microscopy techniques, which I used to characterize the ytterbium titanate samples in this work, will be presented in chapter 2. Finally, a report of results of structural studies (at atomic scale) of ytterbium titanate with stoichiometric ($Yb_2Ti_2O_7$) and non-stoichiometric ($Yb_{2.05}Ti_2O_{7+\xi}$ and $Yb_{1.95}Ti_2O_{7-\xi}$) compositions will be provided in chapters 3 and 4, respectively.

1.1 Overview of Pyrochlores

Amongst the ternary metallic oxides, compounds with the pyrochlore structure, with general formula $A_2B_2O_7$, in which A is a rare-earth ion and B is usually a transition metal, exhibit a wide variety of interesting physical properties. Most of the pyrochlore oxides are known as (3+, 4+) type, $A_2^{3+}B_2^{4+}O_7$, although there are a few of them known as (2+, 5+) type, $A_2^{2+}B_2^{5+}O_7$ [2]. Possessing remarkable composi-

tional and structural flexibility, pyrochlore oxides can exhibit a variety of properties and, therefore, are used in different areas such as electronic devices [3–5], catalysts [6–9] and disposition of actinides [10, 11]. The properties of pyrochlores, like other materials, are tightly linked to their structural defects which can be induced during synthesis process.

1.1.1 Structure of pyrochlores

The space group of pyrochlores is $Fd\bar{3}m$ and the A site ($16d$) and B site ($16c$) cations ordered into separate interpenetrating lattices of corner-sharing tetrahedra (Fig. 1.1) [12–14]. Seven of eight tetrahedral coordination formed by only A ($8b$) or two A and two B ($48f$) are occupied by oxygen; while the one surrounded by four B ($8a$) is unoccupied [14, 15]. Since the oxygen atoms located in the tetrahedra made by four A atoms ($8b$) are crystallographically non-equivalent to the other oxygen atoms ($48f$), the general pyrochlore formula is written as $A_2B_2O_6O'$. Regardless the type of A and B atoms, the $8b$ oxygen sites are located at the fractional coordinates of 3/8, 3/8, 3/8. However, the fractional coordinates of the oxygen sites at $48f$ position is written as x, 1/8, 1/8 where the value of x is in the range of 5/16 to 3/8 depending the type of A and B atoms [2]. For instance, the value of x is considered 0.3348 in Fig. 1.1.

If we only consider the cation sites in the pyrochlore oxides, structure can be understood by examination of the {1 1 1} planes as shown in Fig. 1.2. On these planes, sheets of metal atoms have a hexagonal Kagome pattern and alternate between A (light brown) and B (dark brown) in Figs. 1.2(a-c). In each A layer, B atoms sit at the centre of a A hexagon (Fig. 1.2(a)). These B atoms also lie at the vertex of a pair of opposing B tetrahedra that link to the B Kagome layers above and below Figs. 1.2(c) and (d). A similar pattern is found for A atoms in the B Kagome layer (Fig. 1.2(e)).

The properties of pyrochlores, like other materials, are tightly linked to their structural defects which can be induced during synthesis process. Since A_2O_3 and BO_2 are usually used as the starting material for synthesis of the pyrochlore oxides, an initial (or even local) excess in the amount of one of the A or B oxide is unavoidable. Stanek et al. [16] indicated in their theoretical investigations that any A_2O_3 excess always is compensated by oxygen vacancies as well as occupying the B site by A atoms while a BO_2 excess led to the formation of A^{3+} vacancies.

Structure of titanate pyrochlores with the stoichiometric and non-stoichiometric compositions has been widely studied [14–19]. Consistent with the theoretical results performed by Stanek et al. [16], X-ray diffraction results conducted by Yang et al.

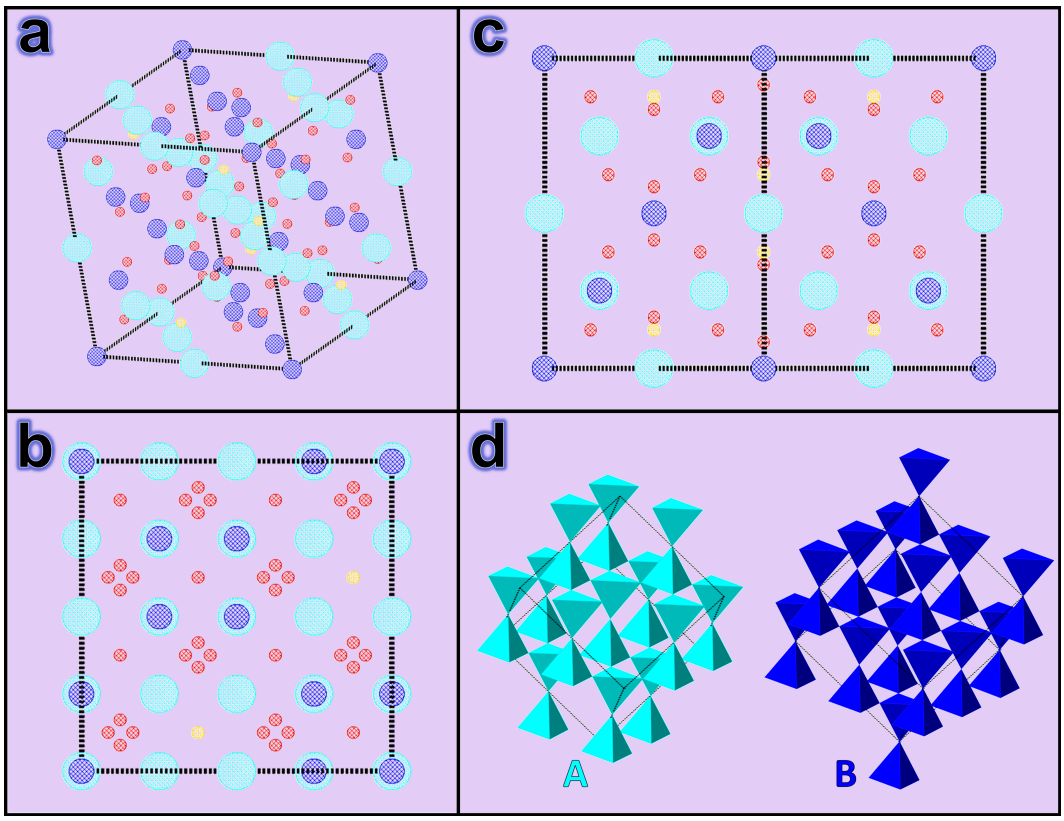

Figure 1.1: (a) shows the position of atoms in a unit-cell of $A_2B_2O_7$ pyrochlore; A, B, O($48f$) and O($8b$) are shown in cyan, blue, red and yellow, respectively. (b) and (c) display the atoms' positions in a unit-cell along [0 0 1] and [1 1 0], respectively. (d) illustrates the separate interpenetrating lattices of corner-sharing tetrahedra formed by A and B cations.

[19] showed that lattice swelling occurs in $Er_2(Ti_{2-x}Er_x)O_{7-x/2}$ by increasing the x values (Er_2O_3 excess). The same trend in lattice swelling has been also reported in $Lu_2(Ti_{2-x}Lu_x)O_{7-x/2}$ [18]. The interpretation of this lattice swelling in the titanate pyrochlores is that excess Er/Lu atoms reside on the Ti sites [18, 19]. In general, excess A cation content is known as "stuffing" [12, 13]. Excess B cation content is less well-studied, and has become known as "anti-stuffing". These terms will be used frequently throughout this thesis.

1.1.2 Radiation resistance of pyrochlores

When an energetic particle, e.g. ion or electron, penetrates a solid material, it collides with the nuclei as well as the electrons of the material [1]. As a result of such collision, the energy of those energetic particles is transferred to the target atoms [1]. If the transmitted energy is high enough to cause the target recoil atoms to leave their positions in the atomic networks, various atomic scale defects may

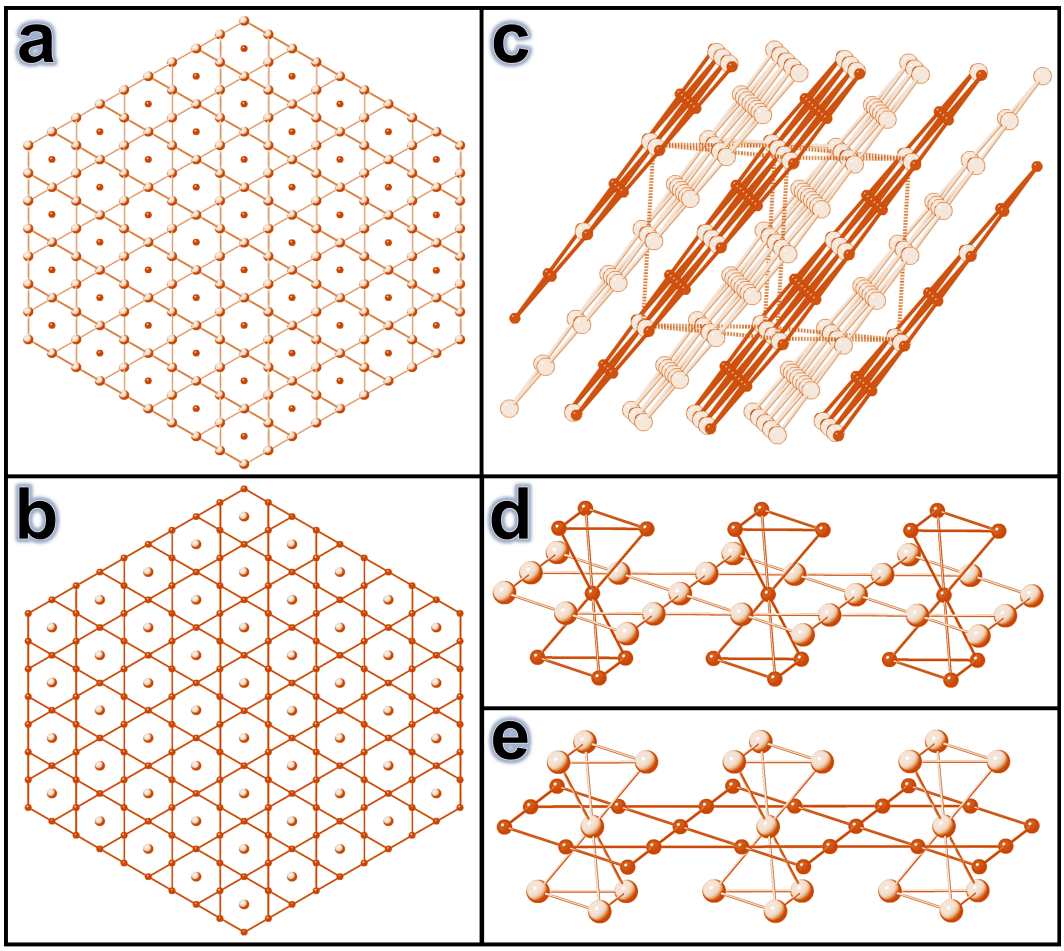

Figure 1.2: (a) and (b) display (1 1 1) Kagome layers of A (light brown) and B (dark brown) cations, respectively. (c) shows how the structure of pyrochlore is formed by the stack of alternate (1 1 1) Kagome layers of A and B cations. (d) and (e) illustrate the configuration of A and B tetrahedra in the Kagome layers, respectively.

induce in the irradiated material [1]. Although many of the induced point defects such as vacancy–interstitial pairs disappear immediately after the irradiation (on the picosecond time scale), some defects could remain in the structure or even form some complex defects [1].

The slowing down process of an energetic ion/electron in a solid target can be separated into two different mechanisms; electronic stopping (energy loss to the target's light electrons) and nuclear stopping (energy loss to the target's atomic positive cores) [1, 20, 21].

Ion irradiation: The nuclear stopping in ion irradiation is as a consequence of ballistic collisions between the ion and the nuclei of atoms in the target [1]. Consequently, the ion kinetic energy is partly transmitted to an atom in the target

material as a whole, leading to its translational motion [1]. It is worth mentioning that the nuclear stopping mechanism is dominant for relatively slow ions, i.e. $E \leq$ 100 keV/amu (Fig. 1.3) [1]. At higher energies, however, the nuclear collisions generally arise as a result of independent binary collisions of target atoms, between which the ion moves in an almost straight path [1]. As for relatively high energy ions, the electronic stopping mechanism is dominant. The electronic stopping in ion irradiation originated from inelastic collisions between the moving ion and the electrons, which can be bound or free, in the target [1]. Hence, the electronic stopping could occur as a result of many physical processes, including ionization of the target atoms, excitation of electrons into the conduction band, collective electronic excitations such as plasmons, etc. [1].

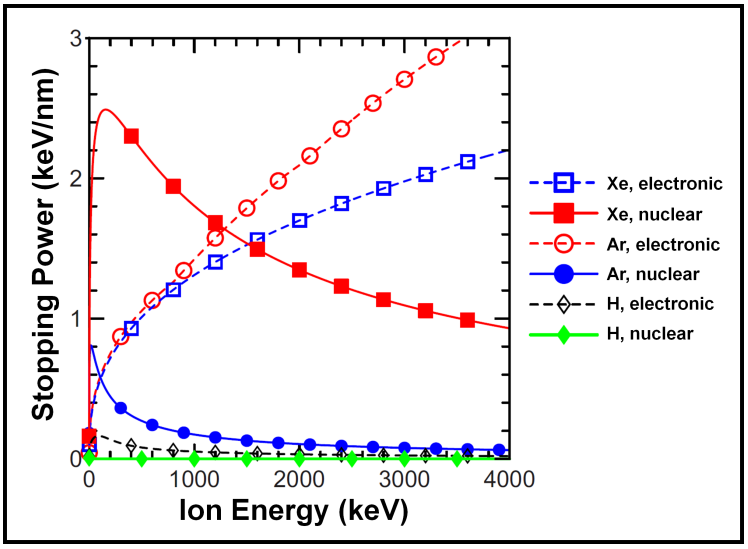

Figure 1.3: Stopping power (electronic and nuclear) as a function of ion energy for H, Ar, and Xe ions moving in a carbon target (adapted from [1]).

Electron irradiation: The slowing down mechanisms in electron irradiation, like in ion irradiation, are the electronic and nuclear stopping. It should be noted that although nuclear stopping occurs in electron irradiation, only a small fraction of the projectile (electron) energy can be transferred to a nucleus of target because of momentum conservation [1, 21]. The maximum transferred energy (T_m) with an elastic collision between the projectile and target atom can be roughly calculated as follows:

$$T_m = \frac{4E}{Mc^2}(E + 2m_0c^2) \tag{1.1}$$

where m_0, M and E are the electron mas (at rest), target atom mass and initial

kinetic energy of the electron [22]. For instance, if $Y_2Ti_2O_7$ pyrochlore is exposed to an electron irradiation of 200 keV, a maximum energy that can be transferred to the Y, Ti and O atoms in the structure are approximately 5, 9 and 27 eV, respectively. According to the calculations performed by Xiao et al. [23], the average threshold displacement energies for Y, Ti and O atoms are 35.1, 35.4, 17.0 and 16.2 eV for Y, Ti, O ($48f$) and O ($8b$) atoms in the $Y_2Ti_2O_7$ structure, respectively. Thus, only oxygen displacement may occur in a perfect $Y_2Ti_2O_7$ pyrochlore at 200 keV electron irradiation.

A radiation-induced order-disorder transformation occurs in many pyrochlores by disordering of the A- and B-site cations, as well as anion vacancies [14]. One of the most important parameters which generally defines the level of cation disordering in these materials is the ratio of the ionic radii of the cations at the A- and B-sites (r_A/r_B) where $1.46 \leq r_A/r_B \leq 1.78$ in the $A_2^{3+}B_2^{4+}O_7$ type oxides [2, 14, 24]. When the cation radii ratio is smaller than 1.46 or larger than 1.78, a structural transformation from the pyrochlore to a defect-fluorite ($(A,B)_4O_7$; see Fig. 1.4 for more information about fluorite and defect-fluorite structures) or a monoclinic layered perovskite-type structure occurs, respectively [14, 24]. On the other hand, imperfection in the anion sites (e.g. displacement of an atom from its lattice position to an interstitial site known as Frenkel defects) is related to the level of cation disordering since the oxidation state of A cations (3+) is not the same as that of B cations (4+) [25].

An order-disorder transition has been observed in ion-irradiated pyrochlores [14]. The results of an experimental work conducted by Lang et al. [26] indicate an increment in the Zr content in $Gd_2Zr_{2-x}Ti_xO_7$ led to an enhancement in the radiation stability of this pyrochlore. In fact, since $Gd_2Zr_2O_7$ ($r_A/r_B = 1.46$) lies at the boundary between an ordered pyrochlore and the defect-fluorite structure, formation of anti-site defects causes a radiation-induced amorphization resistance in this material [14]. However, stuffing Ti atoms onto the Zr sites increases the susceptibility to amorphization as a result of an increment in the formation energy of cation anti-site defects (an increment in r_A/r_B).

Compared to other pyrochlores, the titanate pyrochlores have a lower radiation resistance as a result of a lower tendency to undergo an order-disorder transition due to the higher formation energy of cation anti-site defects (high cation radii ratio) [14, 15]. Nevertheless, Shamblin et al. [24] showed that for the titanate pyrochlores, those with small A-site cations like $Yb_2Ti_2O_7$ – the material of interest in this thesis – exhibit a lower susceptibility to amorphization when they are exposed to ion irradiation. In fact, of all the titanate pyrochlores, $Yb_2Ti_2O_7$ possesses the

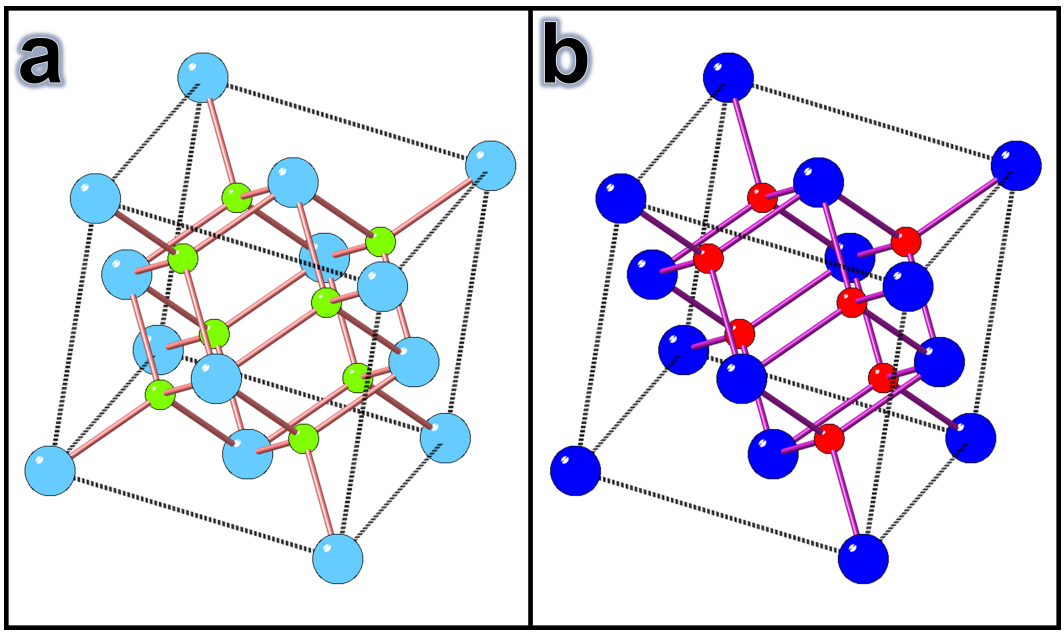

Figure 1.4: (a) Position of atoms in the fluorite (CaF_2) structure; Ca (at face-centred cubic (FCC) sites) and F (tetrahedral sites) are shown in light blue and green respectively. (b) Position of atoms in a defect-fluorite ($(A,B)_4O_7$); cations and oxygen atoms are shown in blue and red respectively. The difference between fluorite and defect-fluorite structure is a missing anion (anion vacancy) in the latter.

lowest cation radii ratio ($r_{Yb}/r_{Ti} = 1.63$ [15]), giving a comparatively low energy anti-site defects and, therefore, the prevention of amorphization during irradiation.

1.1.3 Magnetic frustration in pyrochlores

"Competing interactions, or frustration, are common in systems of interacting degrees of freedom" [12]. The frustration arises when a system cannot minimize all the pairwise interactions simultaneously since each of the interactions in competition tends to favour its own characteristic spatial correlations [12, 27]. There are two classes of frustrated magnetic systems; geometric frustration and random frustration.

Random frustration occurs in systems where the frozen degrees of freedom e.g., positions of the magnetic atoms are not repeated periodically [12]. In AuFe, for instance, the interaction between the Fe magnetic moments can be either ferromagnetic or antiferromagnetic depending on the distance between two magnetic Fe atoms [12]. Such a system, called spin-glass, shows a transition from a paramagnetic state of thermally fluctuating spins to a glasslike state of spins in which, although the spins are frozen in time, they are random in direction [12].

Geometric frustration occurs when magnetic moments, which prefer anti-alignment, reside for example on a triangular crystal lattice [28]. In such a configuration, there is no simple pattern that satisfies all of the bonds since it is impossible for the three spins to align mutually antiparallel to each other (Fig. 1.5(a)) [12, 28]. The picture for an edge-sharing triangular lattice formed from many triangles is complicated since a massive level of configurational spin disorder arises [12]. Hence, such a system exhibits an extensive residual entropy at low temperatures and no phase transition down to absolute zero temperature [12]. As displayed in Figs. 1.5(b-d), there are three types of crystal lattice with triangular geometry which can show geometric magnetic frustration; the triangular, Kagome and pyrochlore lattices [29].

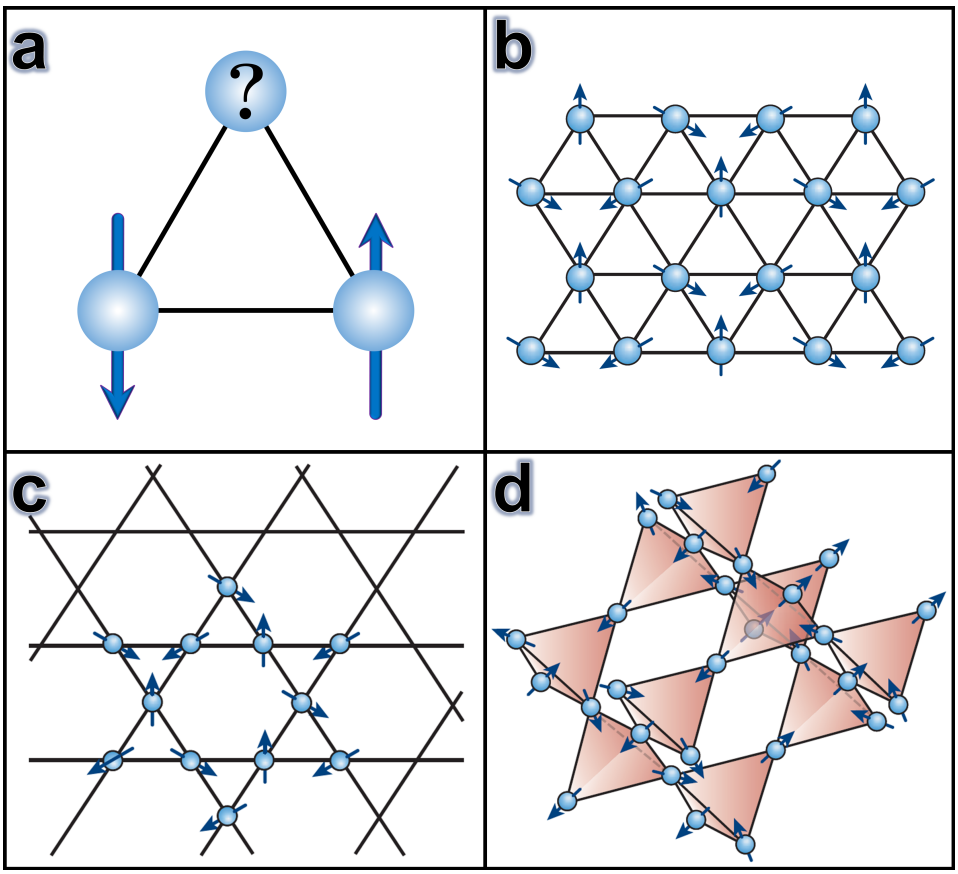

Figure 1.5: (a) When three magnetic cations locate on the vertices of an equilateral triangle, their all three spins cannot be aligned mutually antiparallel to each other. (b), (c) and (d) show the triangular, Kagome, and pyrochlore lattices which can exhibit magnetic frustration, respectively (from [29]).

An antiferromagnet consisting of a two-dimensional triangular lattice of spins, which can only point in two possible (up or down) directions according to the Ising model [30], is one of the prototypes of magnetic frustration [12, 29]. In this lattice

system, although the spins are restricted to the ground states of the Ising antiferromagnet, they continue to fluctuate thermally at low temperatures [29]. By analogy to an ordinary liquid (in which although the molecules establish a dense and correlated state, they are not in a static order state), the spins in the triangular lattice establish a spin-liquid, or cooperative paramagnet [29].

As mentioned before in Section 1.1.1, the A and B cations in the pyrochlore structure lie on distinct but interpenetrating lattices of corner-sharing tetrahedra. Such a lattice is incompatible with a simple organisation of magnetic moments and leads to geometric frustration [12]. By analogy with the large ground-state entropy of crystalline H_2O [31], which has an oxygen lattice of corner-sharing tetrahedra, the ground states of several magnetic $A_2B_2O_7$ materials (e.g. $Dy_2Ti_2O_7$, $Ho_2Ti_2O_7$, $Pr_2Sn_2O_7$ and $Dy_2Sn_2O_7$) have been proposed to be a spin-ice [12, 32]. In a spin-ice, each tetrahedron has two spins pointing inwards and two outwards (so-called ice rules [12, 27]). Nevertheless, other unusual behaviours have been observed in $A_2B_2O_7$ pyrochlores, including spin glass (e.g. $Mn_2Sb_2O_7$ and $Y_2Mo_2O_7$) [32–34], and spin liquid (e.g. $Tb_2Ti_2O_7$ and $Pr_2Ir_2O_7$) [12, 32] states, as well as magnetic configurations modified by quantum fluctuations (e.g. $Y_2Ti_2O_7$ and $Nd_2Ru_2O_7$) [12, 13, 35–37]. The qualities of any given $A_2B_2O_7$ compound are principally dictated by the elements A and B, but can be strongly altered by structural defects, particularly "stuffing" of magnetic A^{3+} ions onto nonmagnetic B^{4+} sites and oxygen, A-site or B-site vacancies [12, 13, 35–37].

In this thesis, the pyrochlore of interest is $Yb_2Ti_2O_7$. The picture for $Yb_2Ti_2O_7$ is complicated by reports of different results for polycrystalline and single crystal samples, and for different samples with nominally identical form, stoichiometry, and structure [38–40]. An early study found a peak in the temperature dependence of the heat capacity of $Yb_2Ti_2O_7$ at 214 mK [41], consistent with later neutron scattering, muon spectroscopy, and magnetization studies that associate the heat capacity anomaly with a first-order transition to ferromagnetic long-range magnetic order [40, 42–45] with a collinear or nearly collinear magnetic structure [42, 43], an ice-like splayed ferromagnetic structure [46] or all-in-all-out splayed ferromagnetic structure [47]. Other works have proposed that this system is a quantum spin-ice [38, 39, 48, 49] or quantum spin liquid [50, 51], or adopts a ground state with short-range correlations where the magnetic moments continue to fluctuate down to temperatures as low as 16 mK [52–54].

The origin of these discrepancies probably lies in subtle structural differences and a proximity to one or more magnetic phase boundaries [55–57]. In such a case, even small perturbations in exchange parameters, which could be driven by a number of

(competing) factors, might be expected to produce significant changes in the nature of the magnetic ground state. Small differences in stoichiometry are known to have significant effects on the properties of $Yb_2Ti_2O_7$. For many rare earth titanate pyrochlores, stuffing of excess A^{3+} ions onto the Ti^{4+} site happens much more readily than "anti-stuffing" of Ti onto the A-site [58]. This also seems to be the case for $Yb_2Ti_2O_7$. Ross and co-workers [38] studied the structure of single crystal and powder samples of $Yb_2Ti_2O_7$ exhibiting different low temperature magnetic properties – different behaviour in their low temperature specific heat transitions (Fig. 1.6) – using neutron powder diffraction. They found that neutron diffraction of $Yb_2Ti_2O_7$ prepared as a powder was best fitted by a stoichiometric model (Fig. 1.7(a)), while a float-zone grown single crystal, (prepared from stoichiometric starting materials), was best described by stuffing of Yb onto 2.3% of Ti sites (Fig. 1.7(b)), rather than Ti vacancies or anti-stuffing [38]. However, Baroudi and co-workers in a synchrotron X-ray diffraction study proposed that Yb, being the smallest of the rare earth atoms, could swap with Ti, producing up to 2% anti-site defects in their $Yb_2Ti_2O_7$ powders [58].

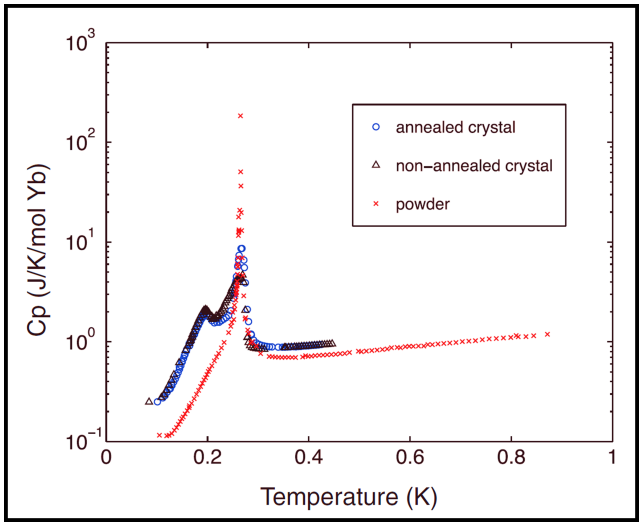

Figure 1.6: "Specific heat of a single crystal annealed in oxygen gas for 10 days (blue circles), compared to a nonannealed slice of the same crystal (black triangles), as well as the powder sample from Ref. [50] (red x's)" [38] (from [38]).

Although, as mentioned above, stuffing of Yb^{3+} ions onto the Ti^{4+} site and anti-stuffing of Ti onto the Yb-site have been proposed to explain the various low temperature magnetic properties of $Yb_2Ti_2O_7$, they have not been directly observed in this material. Hence, I will examine the structure of $Yb_2Ti_2O_7$ at the atomic scale using electron microscopy technique in chapter 3 in order to find a direct evidence

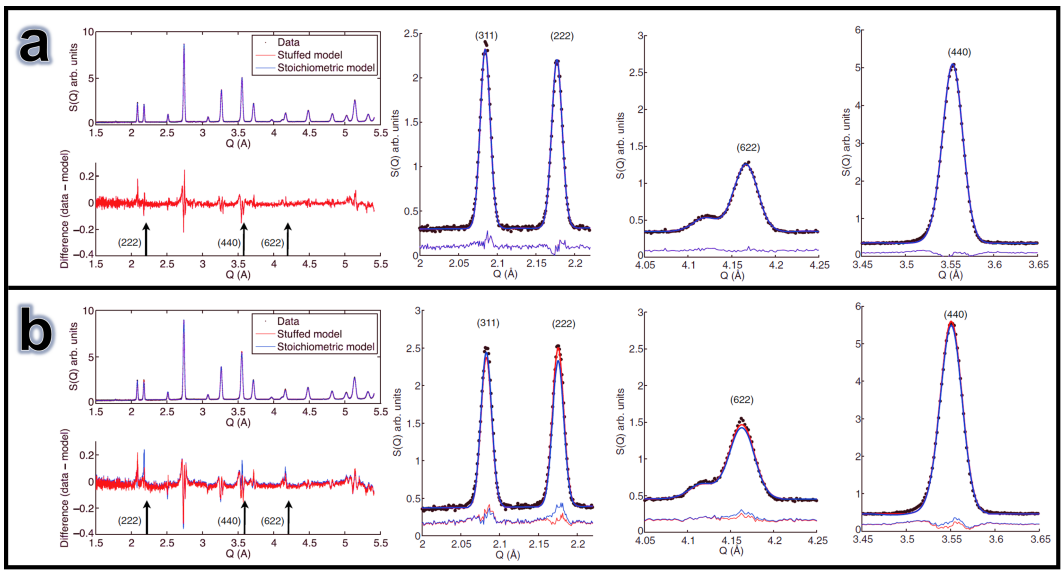

Figure 1.7: "A comparison of two models used in the refinement of (a) the powder sample and (b) crushed crystal sample. This figure shows data at T = 15 K only, as data at all measured temperatures are similar. The stoichiometric model, corresponding to $Yb_2Ti_2O_7$, describes the powder sample well. For the crushed crystal sample, improvements in modeling several peak heights are obtained using a stuffed model corresponding to $Yb_2(Ti_{2-x}Yb_x)O_{7-x/2}$, with x = 0.046(4) (2.3% substitution of Yb^{3+} for Ti^{4+})" [38] (from [38]).

of stuffing or anti stuffing in this material.

1.2 Overview of Electron Microscopy

The human being has always been interested in investigation of their surroundings by observing in order to gain a concrete understanding of the universe. The naked eye can resolve two objects which are about 0.1 mm apart [59]. Therefore, if there are two objects with a distance of less than 0.1 mm, we cannot resolve them and, hence, we see those two as a single object. Such a resolution limit of the naked eye has not satisfied the human's impetuous passion to find an answer for this question "what are materials made of?". Although humans started to use magnifiers since ancient times [60], it took a long time until Hans Janssen and his son Zacharias Janssen, developed the first compound microscope made of two lenses in the late 16th century [59]. The resolving power, defined as the smallest distinguishable distance, of high-quality visible-light microscopes (VLM) are limited by the wavelength of their illumination source as shown in Eq. (1.2) (based on Rayleigh's criterion) to about 200 nm [61, 62].

$$\delta = \frac{0.61\lambda}{\mu \sin \beta} \tag{1.2}$$

where λ, μ and β are the wavelength of radiation, refractive index of the viewing medium and collection semi-angle, respectively. Fluorescence microscopy with super-resolution has been recently developed by W. Hell, W. E. Moerner and E. Betzig, who received the Nobel Prize in Chemistry in 2014 for this development [63]. This technique pushed limits of optical microscopes to nanometre scales [64]. Nevertheless, this technique cannot be used to characterize wide range of materials.

In 1925, Louis de Broglie [65] indicated for the first time that the electron has wave-like characteristics and its wavelength substantially less than that of visible light [62]. Two years later, in 1927, two research groups, Davisson and Germer and Thomson and Reid, separately proved that the electrons have wave nature according to their classic electron-diffraction experiments [62]. Finally, Knoll and Ruska [66] proposed the idea of a transmission electron microscopy (TEM) for the first time in 1932 [62]. According to de Broglie's equation, the wavelength of electrons is related to their momentum and, therefore, can be calculated according to the accelerating voltage, V, of the microscope as shown in Eq. (1.3) [62].

$$\lambda = \frac{h}{p} = \frac{h}{\left[2m_0 eV\left(1 + \frac{eV}{2m_0 c^2}\right)\right]^{1/2}} \tag{1.3}$$

where h, p, m_0, e and c are the Planck constant, momentum of electron, rest mass of electron, unit electron charge and light speed in vacuum, respectively. The wavelength of electrons calculated from Eq. (1.3) according to the accelerating voltage of commercial TEM are listed in Table 1.1. As shown in Table 1.1, the wavelength of the illuminating radiation in the TEM is substantially less than that in optical microscopes which is in the range of ∼100 to 700 nm. That means the resolving power of the TEM is a couple of orders of magnitude better than the optical microscopes (Fig. 1.8).

The majority of the results in this thesis were obtained using aberration-corrected scanning transmission electron microscopy (ac-STEM), and this is covered in section 1.2.2. However, before discussing ac-STEM in detail a brief describing of transmission electron microscopy in general is now given.

Table 1.1: Properties of the electron according to accelerating voltage of an electron microscope (adapted from [62]).

Accelerating voltage (kV)	Relativistic wavelength (nm)	Mass ($\times m_0$)	Velocity ($\times 10^8$m/s)
100	0.00370	1.196	1.644
120	0.00335	1.235	1.759
200	0.00251	1.391	2.086
300	0.00197	1.587	2.330
400	0.00164	1.783	2.484
1000	0.00087	2.957	2.823

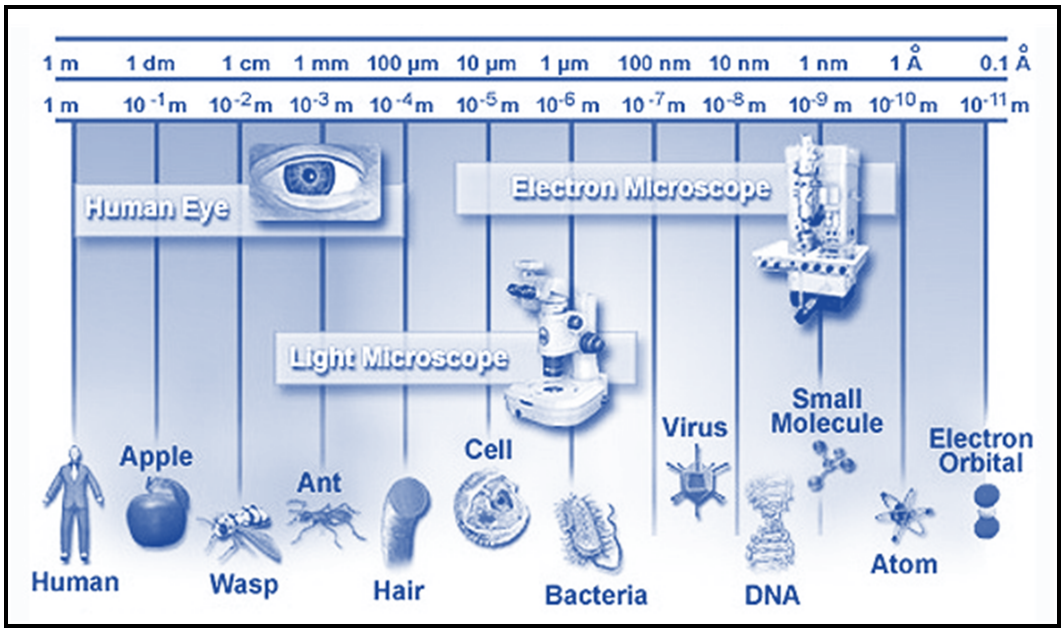

Figure 1.8: The range of resolving power for human eye, VLM and electron microscopes (adapted from [67]).

1.2.1 Transmission electron microscopy

In conventional transmission electron microscopy (CTEM) a wide-beam of electrons is transmitted through a very thin specimen and the structural or chemical data about the specimen can be obtained from interpreting the transmitted electrons. In CTEM images, Contrast, defined as the appearance of a feature in an image, is usually "diffraction contrast" (or the variations in intensity of diffracted electrons across the sample) [68]. As the electron beam is transmitted through a crystalline specimen, it is diffracted by the crystal lattice of the specimen. If specific diffracted electrons screened using an objective aperture and/or tilting specimen

(electron beam) to a specific crystallographic direction, diffraction contrast images can be obtained. This technique is useful to acquire images of defects such as interfaces, dislocations, and second phase particles [68]. In addition to diffraction contrast imaging, phase contrast imaging can be exploited in high-resolution transmission electron microscopy (HRTEM) [68]. In fact, in the phase contrast imaging technique "the phase of the diffracted electron wave is preserved and interferes constructively or destructively with the phase of the transmitted wave" [68]. Using this technique, it is possible to obtain images from atom columns [68]. The schematic of a typical TEM is displayed in Fig. 1.9.

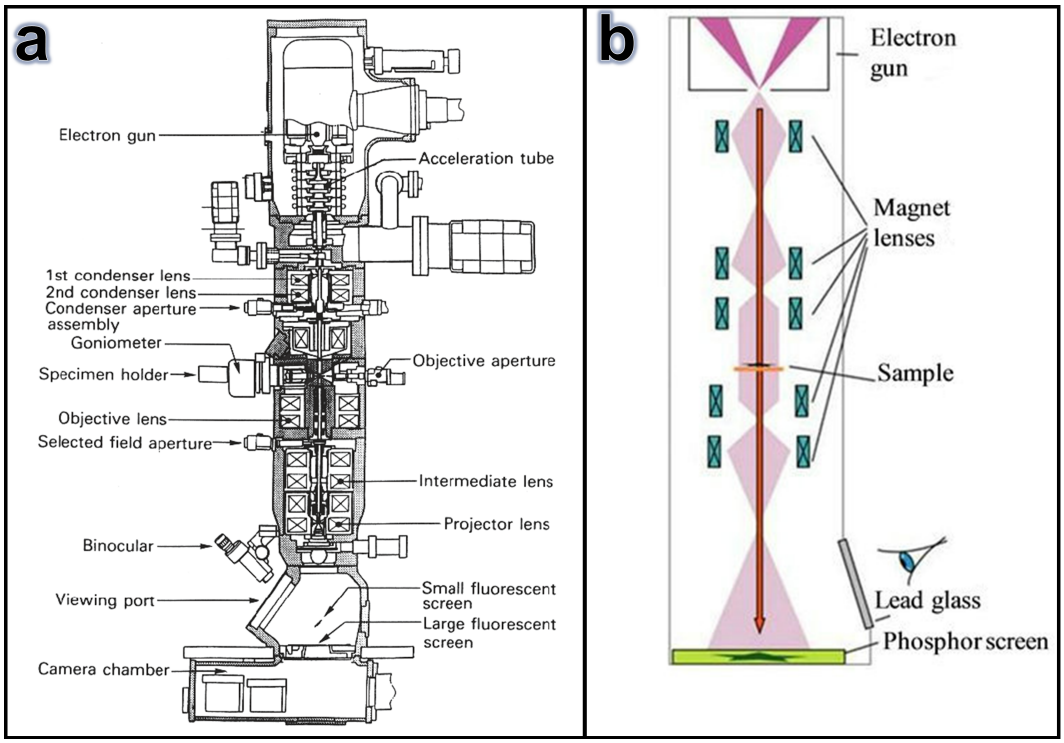

Figure 1.9: The schematic of (a) a transmission electron microscope (from [68]) and (b) the electron path from the electron source to a detector in a TEM (from [69]).

As shown in Fig. 1.9, images are formed using a set of magnetic solenoid lenses in a TEM. Hence, the minimum resolving power of these microscopes – at a certain accelerating voltage – depends highly on the performance of their objective lenses. The TEM lenses, like all magnetic lenses, have aberrations which affect their performance. For example, when a magnetic lens does not have a perfect cylindrical symmetry, the lens distorts the beam to an elliptical shape and, therefore, aberration called "astigmatism" occurs. Another important aberration, spherical aberration (C_S), occurs because of the fact that the focal length depends the beam

off-axis distance. According to the Scherzer's theorem [70], all static round magnetic and electro-static electron lenses have a positive spherical aberration in which the further the ray deviates from the optic axis, the closer focus occurs [68, 71].

TEM has recently undergone a significant advance with the advent of aberration correctors, which push the resolution to a few tens of picometres. In fact, "it is possible today not only to separate atom columns from each other laterally, but also to measure the position of individual atom columns with a precision of up to about a hundredth of an atomic diameter and to determine the occupancy of a given column with atoms" [72]. Nevertheless, detecting light elements, like oxygen, in the presence of heavy elements remains challenging.

Most of the contrast in HRTEM images is based on quantum mechanical phase shifts as a result of interacting the electron wave field with the interatomic potential in the specimen [72]. Since the post-field objective lenses transfer the phase contrast formed by the electron-matter interactions to the image plane, their performance determines the resolving power in the HRTEM images [73].

In TEM, sample is illuminated by an electron plane wave with an incident wave function of $\psi_{in}(\boldsymbol{r}) = \exp(2\pi i \boldsymbol{k}_0.\boldsymbol{r})$ where, $\boldsymbol{k}_0$ is the wave vector [72]. In the crystal, since the wave field interacts with the interatomic potential and, on the other hand, the energy of the incident electrons is high (e.g. 200 keV), the wave function represents a solution of the Dirac equation. Considering small-angle scattering approximation (i.e. considering electrons as free particles), spin polarization can be neglected and, therefore, the Dirac equation adopts a time independent Schrödinger form with relativistically corrected mass and wavelength [72]. Since the wave field decomposes into several plane waves in the specimen, the exit plane wave function (EPWF) can be written as a Fourier integral as below

$$\psi_{ep}(\boldsymbol{r}) = \int_{\boldsymbol{g}} \psi(\boldsymbol{g}) \exp(2\pi i \boldsymbol{g}.\boldsymbol{r}) d\boldsymbol{g} \tag{1.4}$$

here $\boldsymbol{g}$ stands for the reciprocal vector for individual components, representing the spatial frequency [72].

After the specimen, the wave field passes through the electromagnetic lenses suffering aberrations since the lenses are not perfect. It is possible to consider the effect of these aberrations on the EPWF through multiplying its individual components $\psi(\boldsymbol{g})$ by a phase factor which is $\exp(-2\pi i \chi(\boldsymbol{g}))$ [72]. The wave-aberration function,

$\chi(\boldsymbol{g})$, is written as follow:

$$\begin{aligned}\chi(\boldsymbol{g}) =& \frac{1}{2}C_1\lambda\boldsymbol{g}^2 + \frac{1}{2}A_1\lambda\boldsymbol{g}^2\sin\left[2\left(\phi-\phi_{A_1}\right)\right] + \frac{1}{3}A_2\lambda^2\boldsymbol{g}^3\sin\left[3\left(\phi-\phi_{A_2}\right)\right] \\ &+ \frac{1}{3}B_2\lambda^2\boldsymbol{g}^3\sin\left(\phi-\phi_{B_2}\right) + \frac{1}{4}C_3\lambda^3\boldsymbol{g}^4 + ...\end{aligned} \tag{1.5}$$

where the parameters are: C_1, defocus; A_1, two-fold astigmatism; A_2, three-fold astigmatism; B_2, second order coma; C_3, third order spherical aberration [74–76]. ϕ_{A_1}, ϕ_{A_2} and ϕ_{B_2} are the azimuthal orientations of A_1, A_2 and B_2, respectively.

A point in the object plane, as a result of aberrations, is imaged into a disc in the image plane and the disc radius which is the resolving power, R, is calculated by the point spread function [72]

$$R = \max|\frac{\partial\chi}{\partial\boldsymbol{g}}| = \max|C_1\lambda\boldsymbol{g} + A_1\lambda\boldsymbol{g}\sin\left[2\left(\phi-\phi_{A_1}\right)\right] + ...|. \tag{1.6}$$

As electrons pass through the specimen, phase shift is introduced by the interaction of the wave field with the interatomic potential [72]. According to Scherzer [77], phase contrast is proportional to $\sin(2\pi\chi(\boldsymbol{g}))$, hence, as shown in Fig. 1.10(a) for an uncorrected TEM, the resolution is limited by the value of g_s known as the Scherzer point resolution limit. However, Urban et al. [72] showed that it is possible to enhance contrast in the aberration corrected transmission electron microscopy (ac-TEM) under negative spherical aberration conditions and, therefore, make light atoms visible in TEM images (Fig. 1.10).

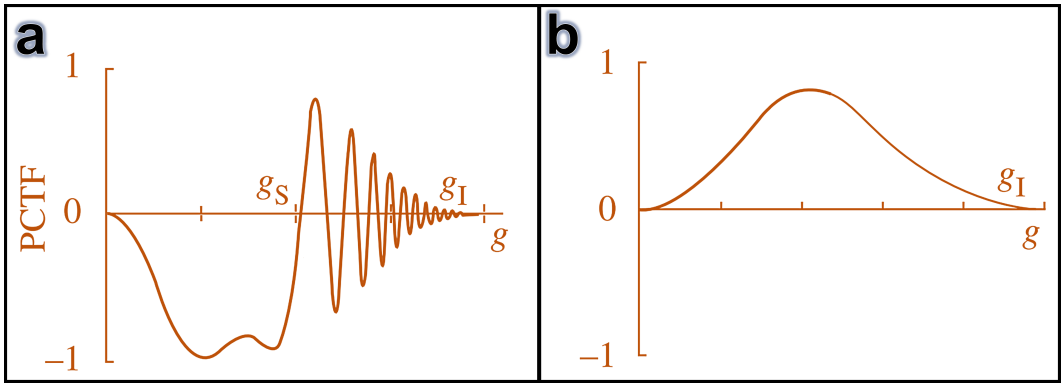

Figure 1.10: Plots of phase contrast transfer function (PCTF), $\sin(2\pi\chi(\boldsymbol{g}))$, as a function of spatial frequency, $\boldsymbol{g}$, for (a) uncorrected microscope and (b) under negative spherical aberration in aberration corrected microscope; g_s and g_I are Scherzer and information resolution limits, respectively (adapted from [72]).

Jia (2001, unpublished data) managed to obtain for the first time ultrahigh resolution images from $SrTiO_3$ using the negative spherical aberration imaging technique

[72]. In this imaging technique, atom columns – even those containing light elements like oxygen – appear bright on dark background in certain settings of the microscope's aberration corrector (Fig. 1.11) [72]. However, using this technique is not straight forward since the imaging area must be flat and very thin (a couple of nanometres). In addition, careful simulation studies are required to optimise the aberration values for a certain sample thickness in order to be used as the settings of the microscope's aberration corrector. A deviation from these optimised values may result in contrast that looks like an atom column somewhere in image which is not related to the position of any column. For instance, as shown in the HRTEM image obtained from a $Yb_2Ti_2O_7$ crystal under negative spherical aberration (Fig. 1.12), all atom columns in this material has not been projected at their real positions.

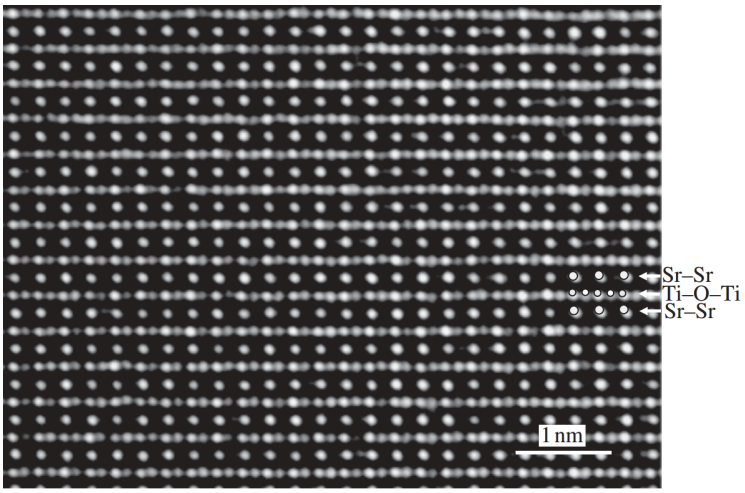

Figure 1.11: [1 1 0] experimental TEM image of $SrTiO_3$ in which all three atom columns are visible (from [72]).

1.2.2 Scanning transmission electron microscopy

In scanning transmission electron microscopy (STEM), in contrast to CTEM, a fine focused beam formed by a probe forming lens is transmitted through and scanned across the thin specimen [78, 79]. Thus, the performance of a STEM highly depends on the magnetic lenses which focus the electron beam on a specimen. In the STEM technique, while the electron beam scans a thin specimen pixel by pixel, the structural or chemical data from the specimen can be collected by different detectors (Fig. 1.13) [79]. A variety of structural and chemical data such as atomic resolution images, diffraction patterns from nanometre regions and atomic resolution compositional maps can be acquired either simultaneously or sequentially from the

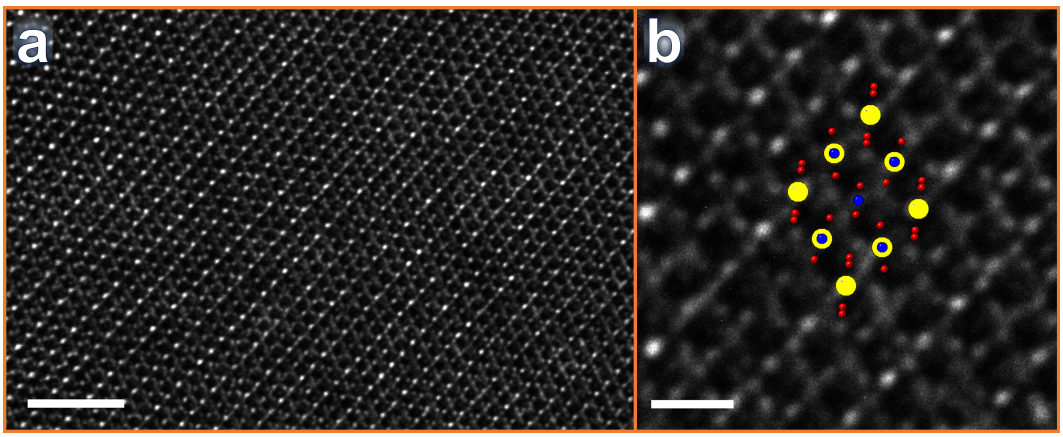

Figure 1.12: (a) [1 1 0] HRTEM image of $Yb_2Ti_2O_7$ taken under negative spherical aberration (scale bar is 2 nm). (b) shows an area from (a) at higher magnification with overlaid schematic of atom columns' positions in $Yb_2Ti_2O_7$; Yb, Ti and O are in yellow, blue and red, respectively (scale bar is 0.5 nm). Note: the presence of significant bright spots and streaks in positions unrelated to the atom columns.

same area of the specimen using this technique [80]. This makes STEM the most powerful method to characterize materials at the atomic scale [80]. In this section a number of imaging as well as analytical techniques which can be exploited in STEM to characterize the atomic structure of materials will be introduced.

The resolving power in STEM also depends on the probe-forming lens's aberrations. These aberrations cause a point object to be projected as a Gaussian image with a finite radius [62]. Even if the convergent lens is free of aberrations, it cannot collect all the electron waves of the electron source (aperture) and, therefore, cannot form a perfect image of the source as a fine focused beam [81]. In this case, as illustrated in Fig. 1.14(a), the image of the source is a bright disc, known as the Airy disc, in the centre and a series of concentric bright rings around the disc. Therefore, the resolving power (diffraction limit, r_{dif}) of even an aberration-free lens is limited by the radius of the Airy disc as defined in Eq. (1.7).

$$r_{dif} \approx \frac{0.61\lambda}{\alpha} \tag{1.7}$$

where α is the probe convergence semi-angle.

Since magnetic lenses are not free of aberration, the resolving power in STEM depends on a combination of diffraction limit and lens's aberrations. The most important aberration in electron microscopes are defocus, astigmatism, spherical aberration and coma. The effect of a certain amount of each one of these aberrations and also a combination of all of them on the probe's shape are shown in Figs. 1.14(b–

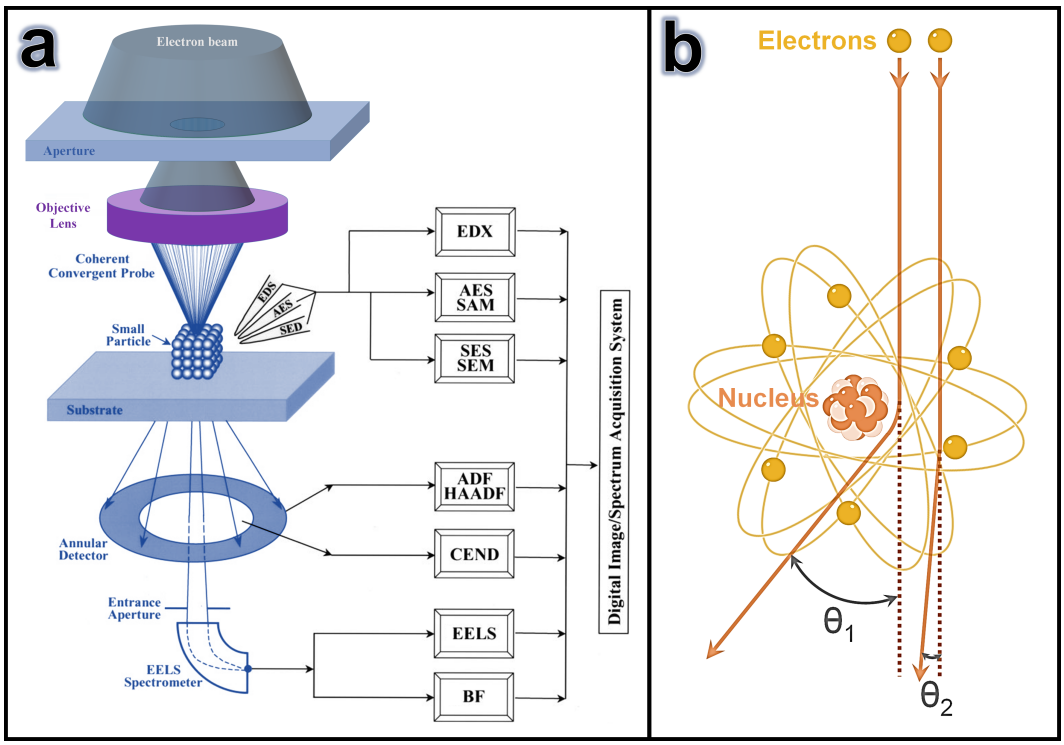

Figure 1.13: (a) Schematic diagram shows the various structural and chemical data (including EDX, Auger electron spectroscopy (AES), scanning Auger microscopy (SAM), secondary electron spectroscopy (SES), scanning electron microscopy (SEM), annular dark-field (ADF), high-angle annular dark-field (HAADF), coherent electron nano-diffraction (CEND), electron energy loss spectroscopy (EELS) and bright-field (BF)) which can be acquired in STEM, see Ref. [80] for more information (adapted from [80]). (b) Schematic of electrons scattered by an isolated atom.

f).

Defocusing the lens produces a position error in the electron trajectory of the beam [76]. Hence, it can change the radius of the probe at the objective lens's focal plane. However, defocus can be easily corrected by moving the specimen or changing the magnetic field of the lens [76]. In addition, when the magnetic field of the lens is not uniform, the electrons which spiral round the optic axis suffer a non-uniform magnetic field and, therefore, astigmatism occurs (Fig. 1.15(a)) [62]. In such a condition, images are distorted with an amount of r_{ast} where

$$r_{ast} = \alpha \Delta f \tag{1.8}$$

and Δf is the maximum difference in focus induced by the astigmatism [62]. Although astigmatism can be corrected theoretically in the ac-STEM, small amounts may remain in the image in practice [76].

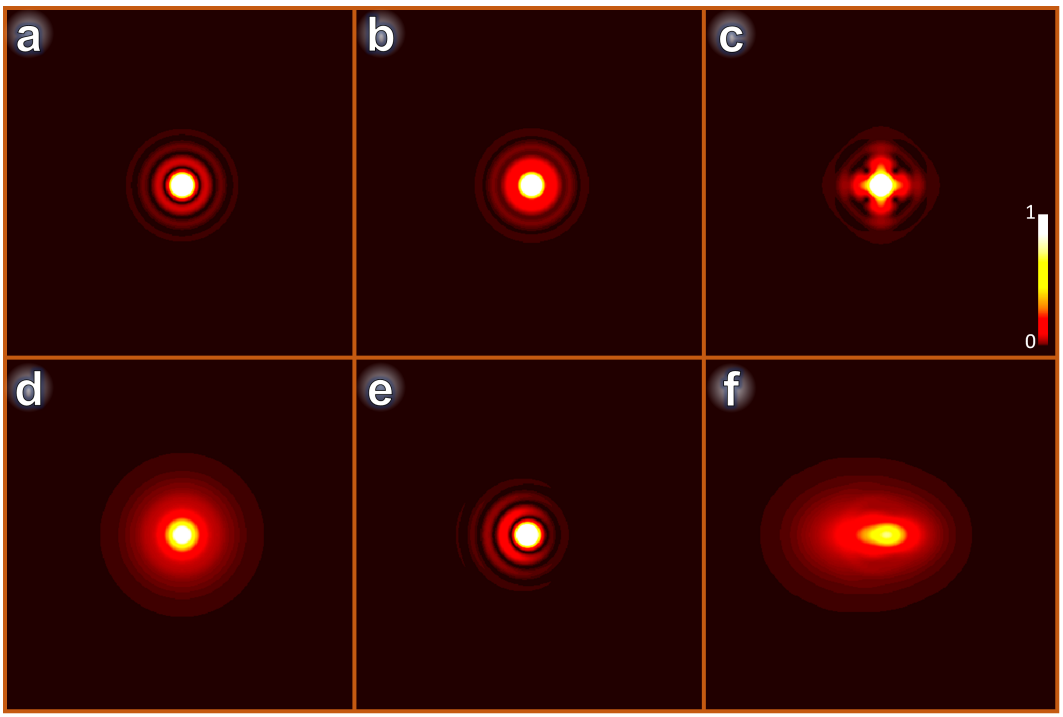

Figure 1.14: Simulated images (the images are 4 nm by 4 nm) for the probe formed by using 15 mrad aperture at the objective lens's focal plane where the objective lens has (a) no aberration, (b) 5 nm defocus, (c) 5 nm astigmatism, (d) 100 μm spherical aberration, (e) 500 nm coma and (f) all the aberrations mentioned in (b–e). Image simulations performed with QSTEM [82] multislice software.

Spherical aberration occurs when the lens field behaves differently for off-axis rays since the magnetic field further away from the axis is stronger than is required (Fig. 1.15(b)) [62, 76]. Therefore, as shown in Fig. 1.15(b), a point object (P) is imaged as two discs, one in the plane of least confusion with a minimum radius and another in the Gaussian image plane with a larger radius (P') [62]. Hence, the image of a point is a high-intensity disc surrounded by a halo of decreasing intensity (Fig. 1.14(d)) [62]. Spherical aberration also distorts the image by an amount of r_{sph} where

$$r_{sph} = \frac{1}{2} C_S \alpha^3 \tag{1.9}$$

and C_S is the spherical-aberration coefficient [62].

When an object point is slightly off the optic axis, all the rays passing through the centre of the lens will travel in their direction without any deflection [81]. However, those rays passing through the peripheral field of the lens will be focussed at different points (Fig. 1.15(c)) as they will experience different magnetic fields and, thus, the point object may appear distorted (Fig. 1.14(e)) [62, 81]. Such a distortion is known

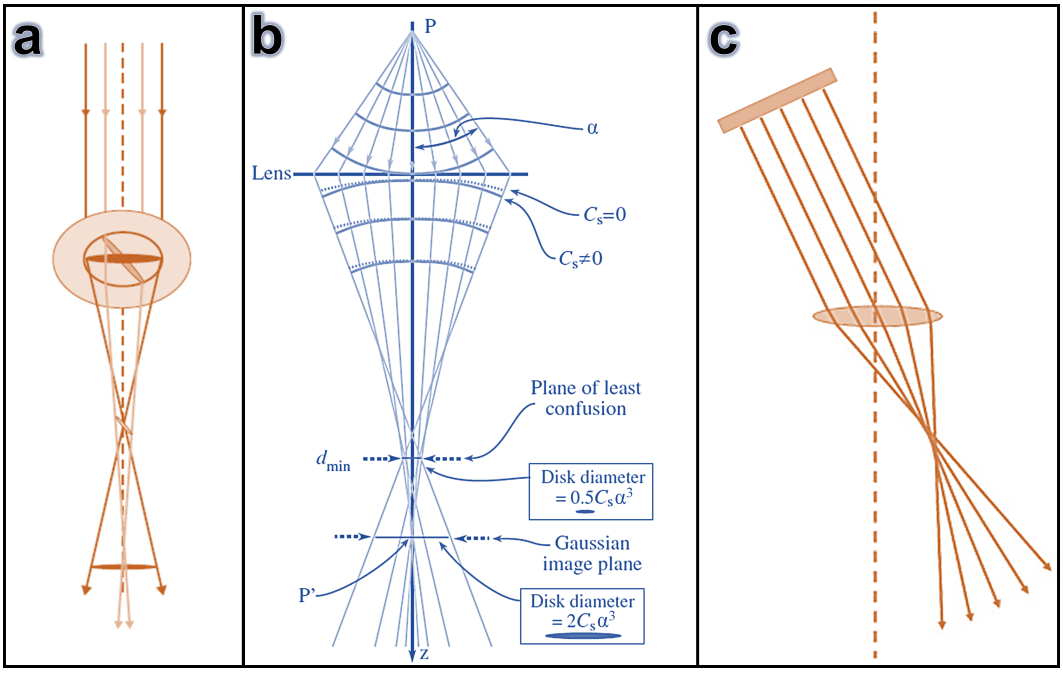

Figure 1.15: Schematic of electron trajectories in the presence of (a) astigmatism, (b) spherical and (c) comatic aberrations (adapted from [62, 81]).

as Coma or comatic aberration.

It is possible to calculate the beam size in STEM. The initial value for the beam radius is the initial Gaussian radius at the source (r_{source}) which defined as

$$r_{source} = \frac{1}{\pi\alpha}\left(\frac{I}{\boldsymbol{B}}\right)^{1/2} \tag{1.10}$$

where I and $\boldsymbol{B}$ are the probe's emission current and brightness, respectively [62, 81]. However, this radius is broadened by the effect of the aberrations. A rough calculation of the beam radius can be obtained using Eq. (1.11). As shown in Fig. 1.16, although an increase in the α value decreases both r_{source} and r_{dif}, there is a limitation for this increment since above a certain point the α value dramatically increases the beam radius (Eqs. (1.7), (1.9), (1.10) and (1.11)). Thus, it is very important to calculate the optimum value for α before choosing an aperture in STEM in order to obtain the best resolution.

$$r_{beam} = \left(r_{source}^2 + r_{dif}^2 + r_{sph}^2\right)^{1/2} \tag{1.11}$$

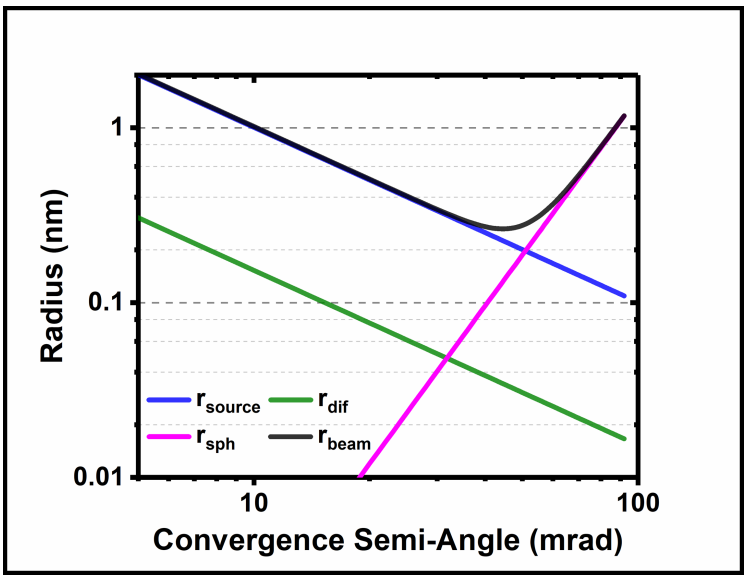

Figure 1.16: Calculation of the beam radius as a function of the convergence semi angle with a lens's spherical aberration of 3 μm and the probe's emission current and brightness of 10 nA and 10 Anm^{-2}Sr^{-1}, respectively.

I. Imaging techniques

In STEM, while the convergent beam transmitted through the specimen, it is diffracted and/or scattered resulting in the formation of convergent beam electron diffraction (CBED) patterns on the back focal plane of the objective lens. As illustrated in Fig. 1.17(a), a CBED pattern consists of sets of convergent beam discs, the radii of which are determined by the angular size of the objective aperture, at the specimen [80]. If α is bigger than the Bragg diffraction angle of the diffracting planes, θ_B, then the convergent beam diffraction discs overlaps as displayed in Fig. 1.17(b) [80]. By placing a detector at the diffraction plane (or an equivalent plane below the intermediate and projector lenses), to collect the diffracted electrons as the electron nanoprobe is scanned across the specimen, a STEM image is formed [80]. As described below, various forms of images can be obtained using different detector configurations in STEM [80].

a. Annular Dark-Field

In the annular dark-field scanning transmission electron microscopy (ADF-STEM), while a probe (focused beam of electrons) scans an area of the sample step by step, scattered electrons are collecting by an annular detector (Fig. 1.18). Usually, the inner radius of the detector is chosen such that no directly transmitted electrons are detected and the signal depends only on electrons deflected by a sufficiently large

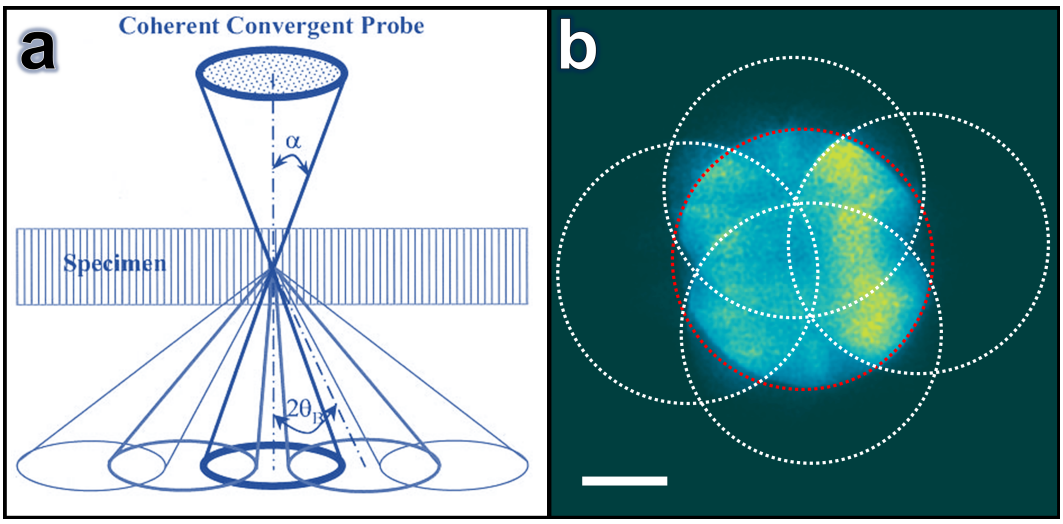

Figure 1.17: (a) a schematic diagram displaying the formation of a CBED pattern (adapted from [80]) and (b) an experimental example of a CBED pattern from $Yb_2Ti_2O_7$ with a convergence semi angle of 15 mrad along [2 1 1] zone axis (scale bar is 10 mrad). The red circle in (b) shows non-diffracted disc while the white ones show the diffracted discs.

angle. Thus, the intensity of each pixel in the ADF image is proportional to the total number of scattered electrons collected by the detector. In addition, since data are collected pixel by pixel in this technique, the size of the scanning area determines the image magnification.

If the inner angle, β_I, of the ADF detector is a little larger than the probe convergence angle α (Fig. 1.18), electrons from the electron beam diffracted coherently can reach the detector and, therefore, contribute the overall signal recorded by the detector [83]. This kind of imaging mode, known as medium-angle annular dark-field (MAADF) or low-angle annular dark-field (LAADF), can be utilized to show features which diffract strongly such as strained areas [83]. In contrast, when the ADF detector inner angle is at least three times bigger than α, there will be little diffracted intensity on the detector and the main source of electrons arriving at the detector will be from high-angle, Rutherford scattering of electrons by atomic nuclei (Fig. 1.13(b)) [83, 84]. In this case, since high-angle scattered electrons are collected by the detector, this imaging technique is called HAADF. Therefore, the images contain quantifiable composition information [83, 84] due to the atomic number sensitivity of Rutherford electron scattering [85–90]. Intensity in the HAADF images increases with atomic number $Z^{1.5}$ to Z^2 [76, 91], giving different contrast for atom columns of different composition when a crystal is viewed along a zone axis; hence this technique is also called Z contrast imaging. Numerous quantitative STEM studies have successfully applied compositional analysis – even with an atom

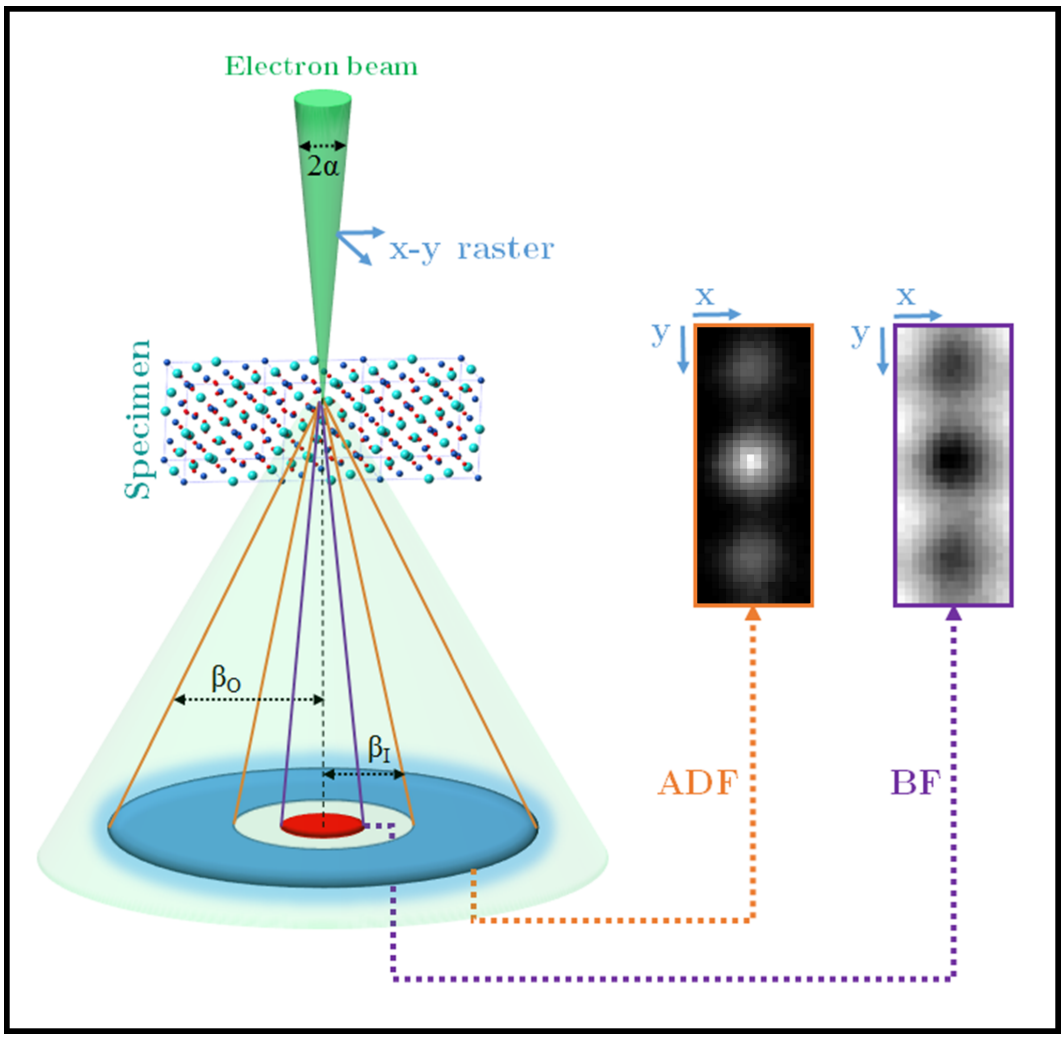

Figure 1.18: Operating principle of simultaneous acquisition of ADF and BF images. α, β_I and β_O are the probe convergence angle, inner and outer angles of the ADF detector, respectively.

precision – on a wide range of materials [83, 85, 89, 92–99].

Light elements in HAADF images, of materials containing a mix of light and relatively heavy elements, are often invisible as a result of their low signal to noise ratio. For instance, oxygen is invisible in the ADF images of oxide materials containing cations with relatively high atomic numbers. Although there is a widely-held opinion that the oxygen atoms are not visible in the dark-field ADF images [100–102], Lu et al. [103] devised a method to make the oxygen columns visible by processing HAADF images of titania nanocrystals with the thickness smaller than 8 nm. However, apart from the thickness limitation, applying this method may not work for other materials in which the oxygen columns are very close to the cations' columns.

b. Bright-Field

In bright-field scanning transmission electron microscopy (BF-STEM) imaging, shown schematically in Fig. 1.18, the direct beam as well as inelastic scattered electron with the angles usually smaller than 1° (∼20 mrad) are collected by a circular detector [62]. While the ADF images contain incoherent contrast roughly proportional to the projected mass thickness of the sample, the BF images contain coherent contrast similar to CTEM [104]. Hence, BF is considered as a phase contrast imaging technique.

Since atom columns – even those containing light atoms – can scatter the electrons by angles higher than the detector radius, they appear with dark contrast in the BF images. In 1974, H. Rose [105] proposed the concept of annular bright-field (ABF) imaging technique. However, many years elapsed before it was used effectively. In 2009, Okunishi et al. [106] successfully used the ABF for imaging the light atoms like oxygen in the structure of $SrTiO_3$ and Fe_3O_4. In fact, they used an annular detector instead of a circular one and obtained better resolution than conventional BF-STEM as a result of removing the oscillating contrast transfer (Fig. 1.10) from the detected signal. The ABF method have been successfully used to observe the atom columns of light elements such as O, Li and even H in the materials containing relatively heavy columns (e.g. Y, Sr, Ti, Fe and Co) [106–109].

II. Analytical techniques

Today, modern STEM are equipped with chemical composition measuring instruments such as EDX and EELS. Using a combination of the STEM imaging and the above mentioned compositional analysis techniques, it is possible to obtain a comprehensive information about both the atoms' positions and their composition materials.

a. Energy dispersive X-ray spectroscopy

High energy electrons can excite an atom if they kick out an electron from one of the inner shell orbitals of the atom and leave a core-hole. The created core-hole can be filled by migration of an electron from the outer shell and consequently the excess energy of the migrant electron emits as a characteristic X-ray (Fig. 1.19(a)). In STEM, while the ADF and/or BF signals are acquiring, an element distribution image (EDX map) can be simultaneously acquired by counting the X-ray photons emitted from the scanned area. However, the resolution of the EDX map may be quite different from that of the STEM images since the EDX's spatial resolution is controlled by not only the incident probe size but also its broadening in the

specimen depending the specimen thickness [110]. In general, EDX resolution can be improved by minimizing both the probe size and its broadening. As displayed in Fig. 1.19(b), the latter can be achieved using thinner specimens and the former can be obtained by exploiting higher brightness field-emission gun (FEG) sources (acquiring enough signals while using a small probe) [110]. In the ac-STEM, where sub-angstrom probe sizes can be achieved, it is feasible to obtain atomic resolution EDX map from materials. Recently, measurement of composition at the atomic scale has been demonstrated using EDX in several research works [111–114].

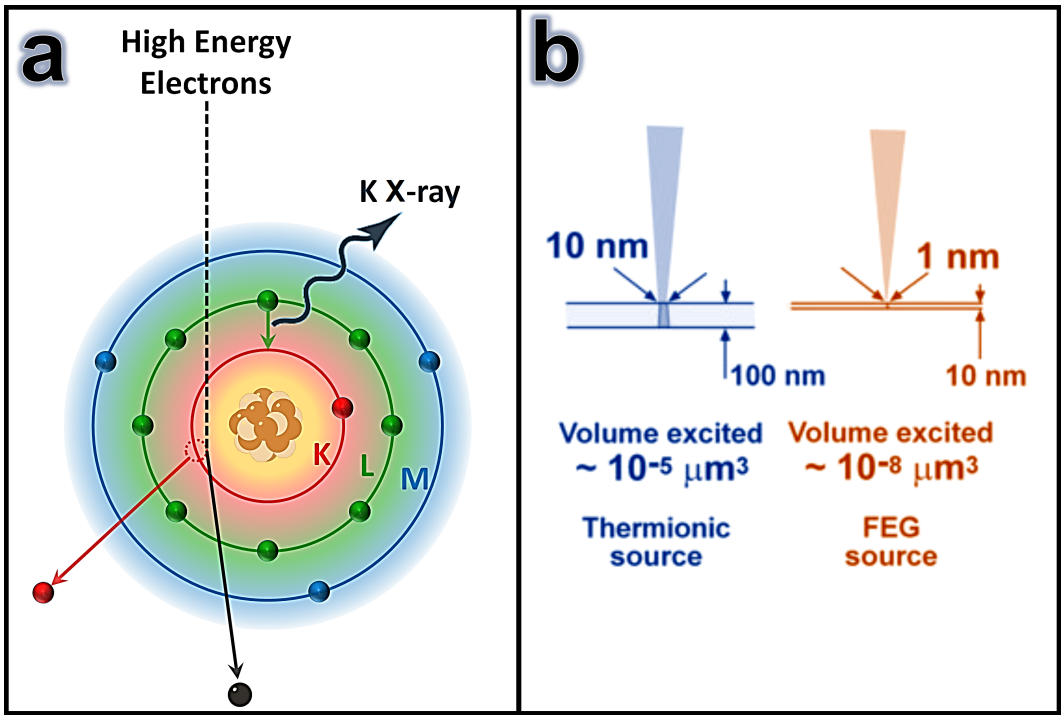

Figure 1.19: (a) schematic of K X-ray emission as a consequence of electron bombardment of an atom and (b) comparison of the excitation volume of an specimen in a thermionic source and FEG-STEM, respectively (adapted from [110]).

b. Electron energy loss spectroscopy

"EELS involves analysing the energy distribution of initially monoenergetic electrons after they have interacted with a specimen" [115]. When high energy electrons travel through a solid specimen, they interact with the specimen's atoms by electrostatic (Coulomb) forces [115]. As a consequence of these forces, a fraction of the incident electrons is scattered while the direction of their momentum is changed [115]. Furthermore, in many cases the scattered electrons transfer a certain amount of energy to the specimen [115]. In the case of single scattering (very thin speci-

men) where the incident beam only loses energy to one atom of the specimen, the transferred energy from the incident beam to the specimen is equal to the amount of energy required to transfer an electron from a lower energy level to a higher one (Fig. 1.20(a)). An EELS spectrum is composed of three main regions, as shown in Fig. 1.20(b), which are the zero-loss peak (ZLP) as well as low-loss (LL) and core-loss (CL) regions [110].

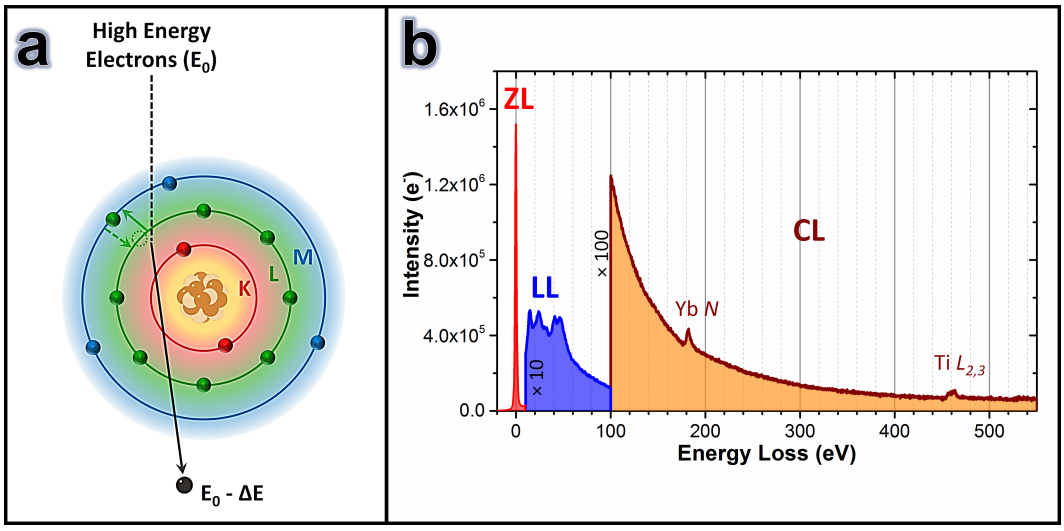

Figure 1.20: (a) shows schematically the inelastic scattering of an electron as a result of the Coulomb repulsion by an outer-shell atomic electron; the arrows show the excitation and de-excitation transitions of the atom and (b) shows a typical EELS spectrum.

The ZLP or elastic peak represents unscattered electrons as well as electrons that are transmitted without suffering measurable energy loss [115]. Considering the fact that the outer-shell electrons can undergo single-electron excitation as well as collective electron excitation known as plasma resonance, inelastic scattering from outer-shell electrons gives rise to appearance of a series of peaks in LL region of the spectrum [115]. Since the outer-shell electrons of the atoms govern the optical and electronic properties of materials, the LL region of EELS spectrum can be used to investigate such properties of materials. In addition, the natural logarithm of the ratio of the integrated area under the LL region to the ZLP is a good indication of the specimen thickness at the position where the spectrum has been acquired [110].

At the CL region, at typically energy losses higher than 100 eV, the number of collected electrons decreases rapidly, making it convenient to use a logarithmic scale for the recorded intensity [110, 115]. "Superimposed on this smoothly decreasing intensity (in the logarithmic scale) are features that represent inner-shell excitation; they take the form of edges rather than peaks, the inner-shell intensity rising rapidly

and then falling more slowly with increasing energy loss" [115]. The energy-loss value at which the sharp rise of each edge appears is approximately the binding energy of the corresponding atomic shell and, thus, it is an excellent signature of the chemical species' identity [110, 115]. Nevertheless, the exact value of the transition energy may have a few electron volts deviation from the binding energy of the corresponding atomic shell since it depends on the environment in the specimen [110].

Both the LL peaks and CL edges, when they are acquired with a high energy distribution resolution, contain a fine structure related to the crystallographic or energy band structure of the specimen [115]. For instance, as illustrated in Fig. 1.21, different allotropes of carbon can be identified even with an energy distribution resolution of 2 eV [115].

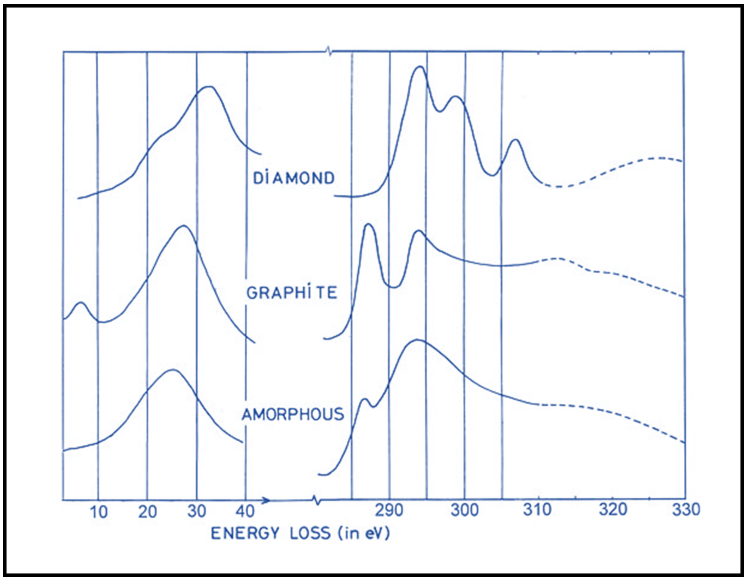

Figure 1.21: EELS spectra (containing LL and CL) of diamond, graphite and amorphous carbon (from [115]).

Moreover, measurement of composition at the atomic scale is also possible using EELS [115, 116]. As the beam scans an area of the specimen and the ADF signal is obtained pixel by pixel, it is possible to acquire simultaneously an EELS spectrum for each pixel. In this case, the data can be stored as a four-dimensional dataset containing compositional information for each pixel of the image. Using this technique, measurement of composition – even at the atomic scale – has been demonstrated in several research works [83, 117–119].

Chapter 2

Experimental procedures

In this thesis I investigate the atomic structure of ytterbium titanate pyrochlore with both stoichiometric and non-stoichiometric compositions using STEM. Information about sample preparation and electron microscopy techniques which I use to characterize the samples is provided in this chapter. I will present results of structural characterization for the stoichiometric and non-stoichiometric samples in chapter 3 and chapter 4, respectively.

2.1 Materials

2.1.1 Synthesis of ytterbium titanate pyrochlore

General information about samples which I characterize in this work are listed in Table 2.1. Polycrystalline (powder) samples of ytterbium titanate with deviations from perfect stoichiometry, i.e. $Yb_{1.95}Ti_2O_{7-\xi}$ and $Yb_{2.05}Ti_2O_{7+\xi}$, were synthesized using a solid state reaction method. Stoichiometric quantities of Yb_2O_3 and TiO_2 powders were repeatedly ground, pressed into pellets, and sintered at 1150 °C for 12 hours, with a final firing at 1350 °C for 24 hours.

Table 2.1: Information about samples characterized in this work.

Sample name	Compositions	Crystallinity	Where made
sample 1	$Yb_2O_3 + 2TiO_2$	single crystal	Meiji University, Japan
sample 2	$Yb_2O_3 + 2TiO_2$	single crystal	University of Warwick
sample 3	$Yb_2O_3 + 2TiO_2$	single crystal	Meiji University, Japan
$\mathbf{Yb_{1.95}Ti_2O_{7-\xi}}$	$0.975Yb_2O_3 + 2TiO_2$	polycrystalline	University of Warwick
$\mathbf{Yb_{2.05}Ti_2O_{7+\xi}}$	$1.025Yb_2O_3 + 2TiO_2$	polycrystalline	University of Warwick

Stoichiometric $Yb_2Ti_2O_7$ samples were prepared as single crystals by the floating zone method. Stoichiometric quantities of Yb_2O_3 and TiO_2 powder were mixed, pressed into rods and then sintered at 1150 °C (sample 1 and sample 3) or 1350 °C (sample 2) for 24 hours. Using these rods, single crystals were grown in air at a rate of 1.5 mm/h (sample 1 and sample 3) or 2 mm/h (sample 2). The crystals had a typical diameter of ∼6 mm and a length of 20 to 30 mm. The samples were used in previous published works [42, 43, 45].

2.1.2 Structure of $Yb_2Ti_2O_7$

As mentioned in Section 1.1.1, the structure of $Yb_2Ti_2O_7$, like other pyrochlores, can be described as a repetition of alternating {1 1 1} Yb and Ti Kagome layers. In each Yb layer, Ti atoms sit at the centre of an Yb hexagon (top, Fig. 2.1(a); most oxygen atoms have been omitted for clarity). These Ti atoms also lie at the vertex of a pair of opposing Ti tetrahedra that link to the Ti Kagome layers above and below. A similar pattern is found for Yb atoms in the Ti Kagome layer (bottom, Fig. 2.1(a)). Each metal atom is surrounded by an octahedron of oxygen ions that either lie on a Wyckoff f-site (red) or b-site (yellow). Note that all the cations of the same type are symmetrically identical, and this pattern is found on all of the symmetrically equivalent {1 1 1} layers. Crystallographic parameters for a perfect $Yb_2Ti_2O_7$ crystal [120] are listed in Table 2.2.

Table 2.2: Crystallographic parameters considered for a perfect $Yb_2Ti_2O_7$ crystal with the lattice parameter of 10.03 Å (adapted from [120]).

Atom	**Wyckoff position**	**Fractional coordinates**			**Debye Waller factor (Å²)**
O1	$48f$	0.3750	0.3750	0.3750	0.0105
O2	$8b$	0.3348	0.1250	0.1250	0.0101
Ti	$16c$	0.0000	0.0000	0.0000	0.0178
Yb	$16d$	0.5000	0.5000	0.5000	0.0215

When viewed along [2 1 1], one set of {1 1 1} planes is seen edge-on. In this projection there are four types of heavy atom column (Fig. 2.1(c)); those containing only Yb, those containing only Ti, and two different mixed (M) columns containing 50% Ti and 50% Yb. The difference in M columns arises because there are twice as many oxygen atoms around 50:50 columns in the Yb Kagome layer ($M1$) in comparison with 50:50 columns in the Ti Kagome layer ($M2$). In this projection the oxygen atom columns lie ∼72 pm from the $M1$ columns while those next to

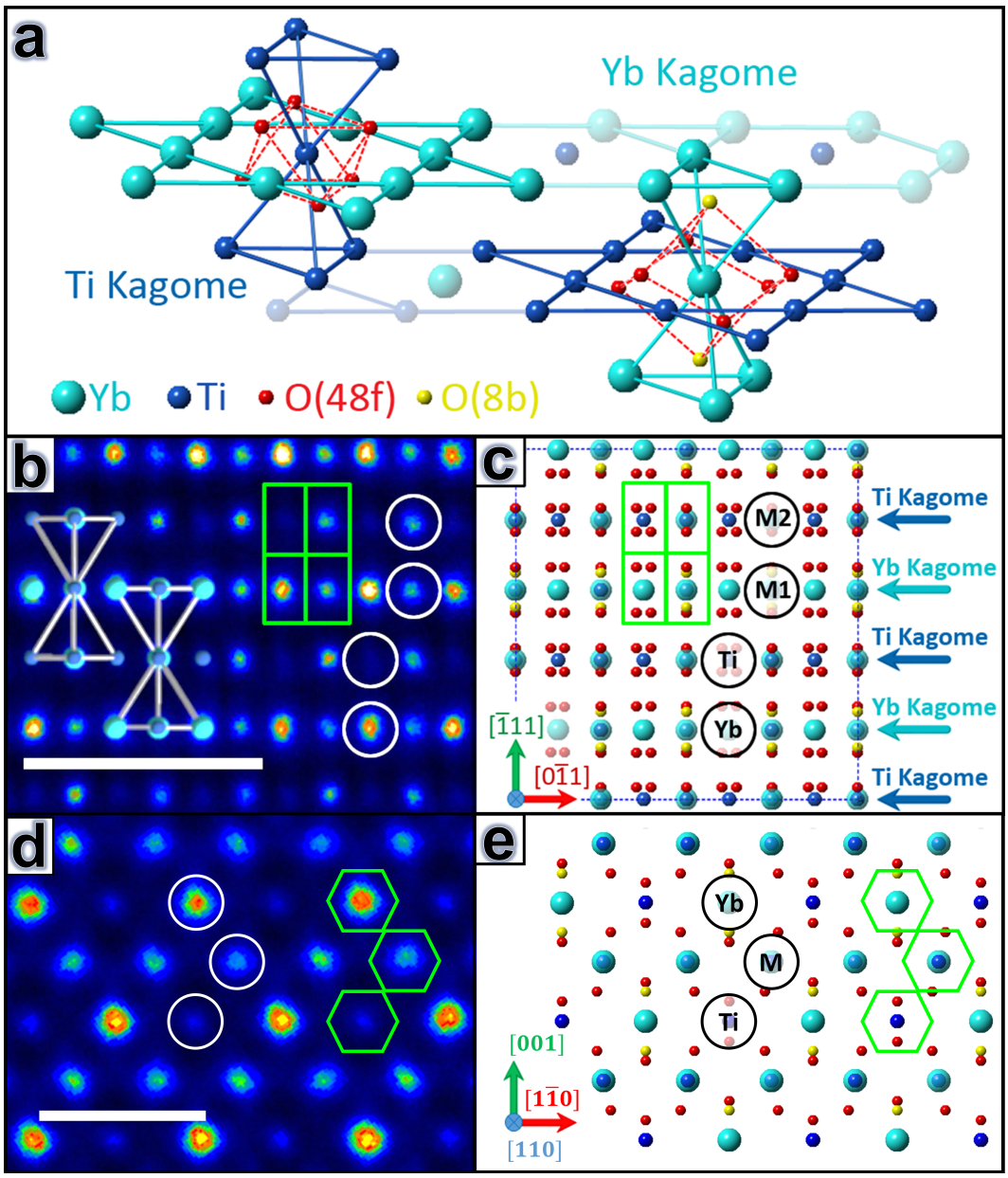

Figure 2.1: (a) The pyrochlore structure of $Yb_2Ti_2O_7$ (see text for details). (b) [2 1 1] ADF-STEM image of $Yb_2Ti_2O_7$ with Yb and Ti tetrahedra overlaid (scale bar is 1 nm). Four different types of atom columns are visible, marked by circles. The Yb columns are the brightest, followed by mixed columns $M1$ and $M2$, while the Ti columns are the faintest. (c) Corresponding projection of the crystal structure showing the Kagome layers and the four different types of atom column. (d) [1 1 0] ADF-STEM image of $Yb_2Ti_2O_7$ (scale bar is 1 nm). (e) Corresponding projection of the crystal structure showing the three different types of atom column in this direction. Voronoi cells, used for measurement of intensities in the images along both the [2 1 1] and [1 1 0] directions, are illustrated in green in (b-e).

$M2$ columns lie at a distance of ∼49 pm. Furthermore, in each atom column the distance between one cation and the next along [2 1 1] is large (∼6.14 Å) leading to a relatively low number of atoms in each column for a thin specimen. This provides favourable conditions to detect the substitution of Ti on a Yb column (or vice versa) through a difference in HAADF-STEM contrast. On the other hand, in [1 1 0] direction the distance between one atom column and the next is large enough (∼3.07 Å) to overcome limitation of spatial resolution due to delocalization effects [115] and, therefore, acquire high-quality atomic resolution EDX/EELS elemental maps.

2.1.3 Magnetic properties

As described in section 1.1.3, different $Yb_2Ti_2O_7$ single crystals with nominally identical form, stoichiometry, and structure show different magnetic properties at low temperatures. Hence, in order to discover the origin of such mysterious behaviour of this material, I am characterizing the atomic structure of three $Yb_2Ti_2O_7$ single crystals showing different low-temperature specific heat characteristics although they have the same composition (stoichiometry). As shown in Fig. 2.2(a), sample 1 exhibits a sharp transition at ∼200 mK, consistent with the onset of long-range magnetic order, typical of stoichiometric powder samples [50] although at a reduced temperature. Sample 2 shows two relatively broad anomalies at ∼200 and 280 mK. This type of behavior could be explained by short-range magnetic ordering, with the magnetic correlation length limited by defects [38]. Finally, sample 3 exhibits no clear specific heat anomaly, consistent with a disordered magnetic state, and is thus expected to have significant stuffing of Yb^{3+} onto the Ti^{4+} sites [38].

For the polycrystalline samples, the sample with less Yb than the stoichiometric composition, $Yb_{1.95}Ti_2O_{7-\xi}$, exhibits a transition at ∼270 mK (Fig. 2.2(b)), like the stoichiometric powder samples [50]; however, the transition peak is not as sharp. This means that this sample has some of the characteristics of a magnetically ordered system but the extent of the magnetic correlations may be less in this sample than the stoichiometric powder samples. In contrast, the $Yb_{2.05}Ti_2O_{7+\xi}$, exhibits no clear specific heat anomaly, consistent with a disordered magnetic state.

2.2 TEM sample preparation

In order to avoid any issues associated with sample inhomogeneity and to be able to compare the microscopy and heat capacity results directly, the TEM specimens were taken from the same sections of the single crystal or powder used for the specific

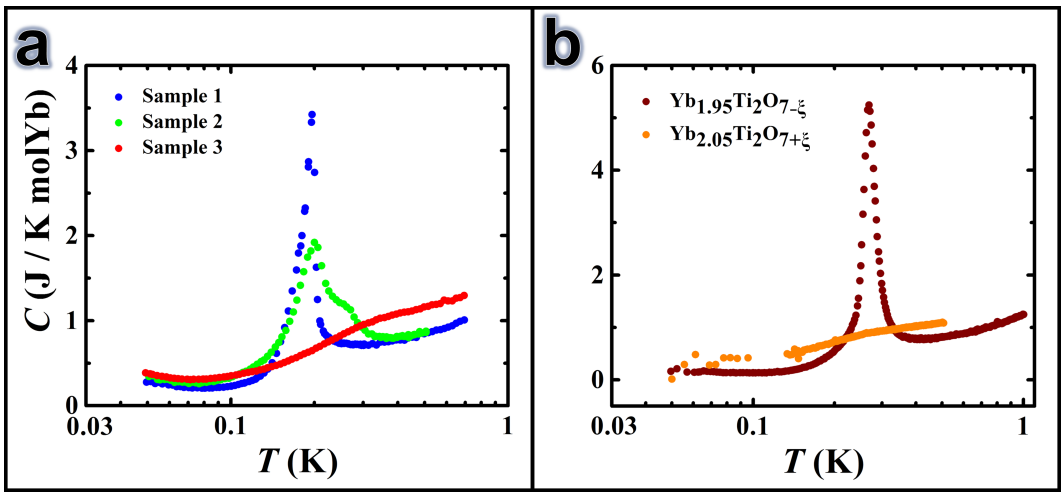

Figure 2.2: Specific heat as a function of temperature in zero magnetic field for (a) the three $Yb_2Ti_2O_7$ single crystal samples [42, 43, 45] and (b) non-stoichiometric samples [M.R. Lees unpublished data].

heat capacity measurements.

The powder samples were mixed with fine ($\sim$1 μm) aluminium powder in a volume ratio of 1:4 placing in an aluminium foil wrap and then cold rolling the mixed powder. This produced a solid aluminium sheet encasing the powder approximately 5 $\times$ 10 mm in size and 100 μm in thickness.

A disc of 3 mm in diameter was cut out of each sample (Al sheet or single crystal) and then mounted on a copper ring. Then, the TEM specimens were prepared using standard routes, i.e. mechanical grinding followed by ion milling. In the first step, the specimens were pre-thinned to a thickness of 20 – 50 μm by mechanical grinding and polishing. In the next step, the mechanically polished specimens were thinned down further to electron transparency using a GATAN (Model 691) precision ion polishing system (PIPS). In this method, continuous bombardment of the specimens by accelerated Ar^+ ions at 6 keV decreases gradually the thickness of the specimens down to electron transparency. Finally, surface damage was minimised by a final low energy milling step at 500 eV for about seven minutes.

2.3 Transmission electron microscopy procedures

The principal microscope used to analyse the samples described in this thesis was a doubly-corrected JEOL ARM200F microscope, operating at 200 keV. In this microscope, the sub-angstrom probe size (full width at half maximum (FWHM) $<$ 80 pm) and image resolution (resolution $<$ 80 pm) allow atomic resolution imaging

both in STEM and TEM modes [121].

The microscope is equipped with a Gatan Quantum EELS which enables detection and quantification of the elemental composition of materials at the atomic scale [121]. The microscope is also equipped with a 100 mm^2 Oxford Instruments windowless EDX detector which enables the acquisition of composition maps of materials with atomic resolution [121]. Moreover, it is possible to obtain both the EDX and EELS signals simultaneously using this microscope.

2.3.1 STEM imaging

The main aspects of interest for this work is the resolution and quantification of intensities in STEM images. Therefore, the probe's aberrations were corrected to achieve both A_2 and B_2 values less than 10 nm as well as all the values for $|C_3|$, A_3 and S_3 smaller than 1 μm (see Eq. (1.11) for more information). In addition, the emission current and brightness were typically 200 μA and 70 $Anm^{-2}Sr^{-1}$, respectively. According to Eqs. (1.7), (1.9), (1.10) and (1.11), a sub-angstrom resolution can be achieved using a probe convergence semi-angle (α) in the range of ~15 to 50 mrad for this microscope (Fig. 2.3). Hence, the images in this work obtained with the α value of 15 or 29 mrad.

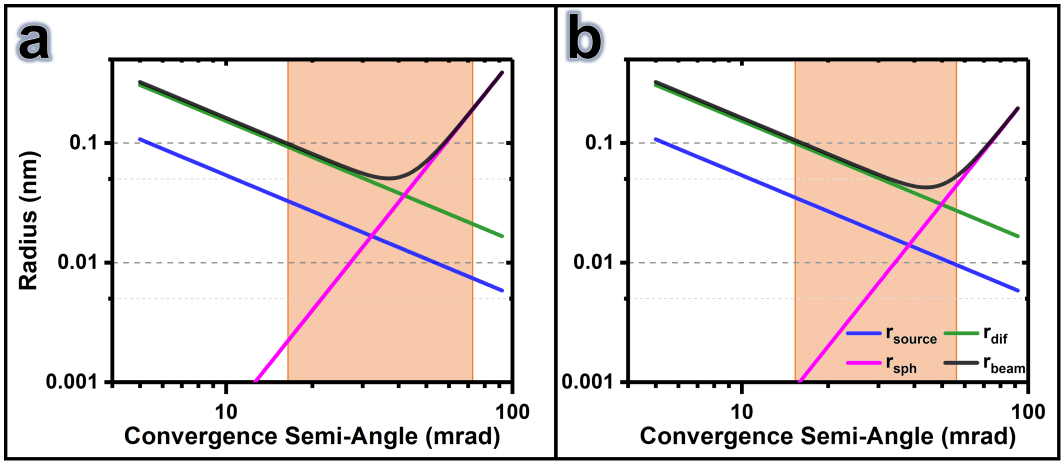

Figure 2.3: Calculations of the probe size as a function of α with a probe current of 200 μA and brightness of 70 $Anm^{-2}Sr^{-1}$ at the C_S values of (a) 500 nm and (b) 1 μm (see Eqs. (1.7), (1.9), (1.10) and (1.11) for more information). A sub-angstrom resolution can be achieved using a probe convergence semi-angle in the ranges filled in orange in (a) and (b).

Defect-free, flat and uniform regions of interest were selected for high-quality STEM images. In order to obtain data with a good signal to noise ratio, unaffected by specimen drift, up to sixty images were collected sequentially, all with a short time of 10 μs/pixel using Schaffer's stack builder plugin for Digital Micrograph [122].

The resulting set of images was aligned using in-house code assuming a rigid-body shift and normalized cross-correlation and summed to produce high quality, low noise data.

At small scattering angles, i.e. when the inner angle of the ADF detector is only a little larger than the probe convergence semi-angle α, coherent diffraction effects can produce strain contrast that is very sensitive to crystal orientation [83]. This contrast compromises the ability to relate intensities to atomic number [83]. Here, therefore, for images intended to be sensitive to composition I use an ADF detector inner angle at least 4.6 times the probe convergence semi-angle α, giving a scattered intensity proportional to a small power of the atomic number, $Z^{1.5}$ to Z^2 [76, 91]. For images that show greater sensitivity to the configurations of oxygen atoms I use an ADF detector inner angle of only $\sim 2.4\alpha$. Data were normalized to the incident beam intensity using calibrated brightness/contrast levels, a map of the ADF detector response and an image of the diffraction pattern falling on the detector (Fig. 2.4), following an approach similar to that of LeBeau and Stemmer [123] and Rosenauer et al. [124].

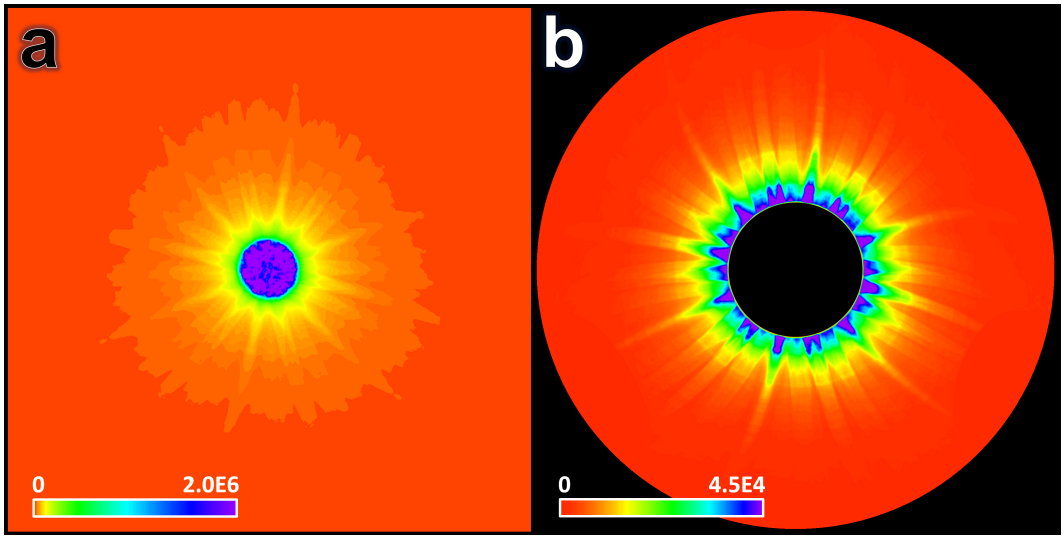

Figure 2.4: (a) An experimental diffraction pattern of electron beam scattered by $Yb_2Ti_2O_7$ with a convergence semi-angle of 29 mrad along [1 1 0] zone axis and (b) a part of the diffraction pattern shown in (a) falling on an ADF detector with inner and outer radii of 70 and 280 mrad, respectively. The diameter of the solid black circle in the center of (b) is 140 mrad.

The intensity in the ADF images (I_{img}) is normalized according to Eq. (2.1),

$$I_{img} = \frac{I_{img} - I_{vac}}{I_{det} - I_{vac}} \tag{2.1}$$

where, I_{det} and I_{vac} are the mean intensity found on detector (beam intensity) and vacuum region in the detector map, respectively [124]. Fig. 2.5(a) shows an example of the detector output when the beam is scanned over it. As illustrated in Fig. 2.5(b), there is a linear relationship between the beam intensity and brightness. Thus, it is possible to extrapolate the beam intensity at a desired brightness at which an ADF image is acquired. The vacuum intensity can also be calculated by acquiring an ADF image at vacuum.

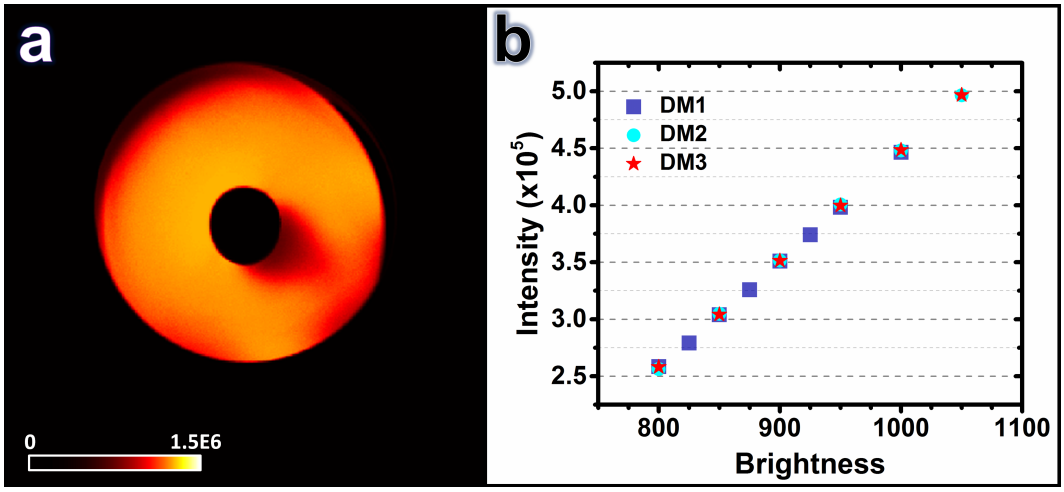

Figure 2.5: (a) an image of the ADF detector acquired at contrast and brightness of 1100 and 1800, respectively. (b) the beam intensity as a function of the brightness calculated from detector maps acquired at different times ($DM1$, $DM2$ and $DM3$).

2.3.2 EDX

EDX measurements were obtained with a windowless Oxford Instruments X-max 100 silicon drift X-ray detector. EDX line scans as well as EDX compositional maps for the ytterbium titanate samples made using Ti $K\alpha$ (4.51 keV) and Yb $L\alpha$ (7.41 keV) X-rays. The parameters used to acquire both the line scan and map data in this work are listed in Table 2.3. Acquired EDX spectra from the samples contain characteristic peaks for O, Ti and Yb which are superimposed on a noisy background (Fig. 2.6) due to statistical variations. On the other hand, they contain overlapped peaks e.g. O $K\alpha$ (∼0.53 keV) and Ti $L\alpha$ (∼0.45 keV) as shown in Fig. 2.6. Thus, AZtecTEM software [125] was used to process the acquired EDX data (i.e. peak deconvolution and background subtraction) in order to make the data quantifiable.

Table 2.3: Parameters used to acquire EDX data.

Parameters	Line Scan	Map
Accelerating voltage	200 keV	200 keV
Probe size	5C (~0.5 nm)	5C (~0.5 nm)
Convergence semi-angle*	29 mrad	29 mrad
Number of pixels	500	256 × 256
Dwell time	5 ms	50 μs
Total time for a pixel	$>$ 1.5 s	$>$ 0.2 s

*Although large convergence angle is usually not recommended for acquiring atomically-resolved EDX data, a large convergence angle is used here to obtain a good signal-to-noise ratio.

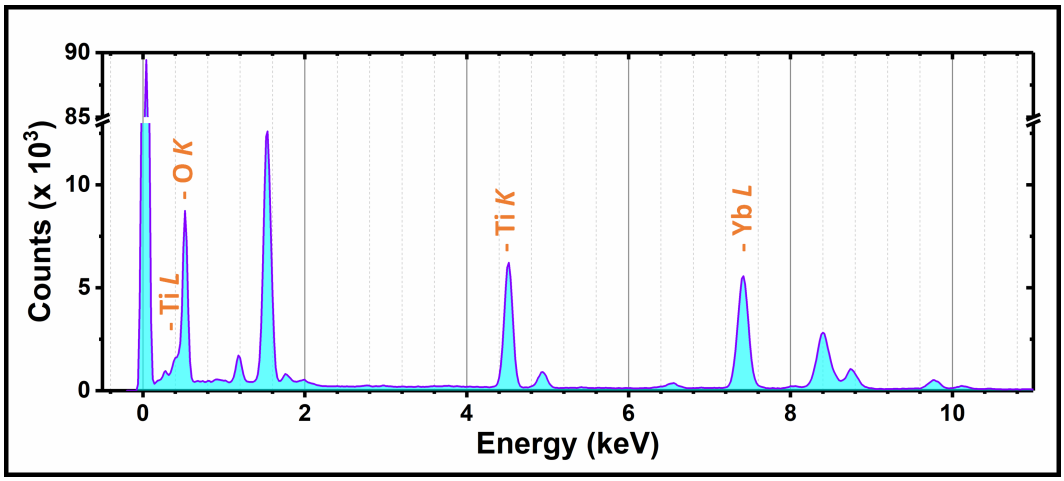

Figure 2.6: A typical EDX spectrum obtained from $Yb_2Ti_2O_7$.

2.3.3 EELS

EELS spectra were obtained with a Gatan Quantum EELS system operating in dual EELS mode, allowing correction of ZLP offsets and removal of multiple scattering from high energy CL edges by Fourier-log deconvolution calculated from the LL spectrum. The obtained data were processed by DigitalMicrograph software [126].

EELS maps were acquired with pixel exposure times of 0.1 and 10 ms for LL and CL (or high-loss (HL)) spectrum images, respectively. In addition, the Yb N, Ti L and O K edges were used to extract elemental maps from the spectrum images (Fig. 2.7). On the other hand, electron energy loss near-edge structure (ELNES) spectra for the Ti $L_{2,3}$ and O K edges as well as LL peaks were obtained using the total exposure times of 50, 100 and 0.01 s, respectively. The other parameters used to acquire the EELS data in this work are listed in Table 2.4.

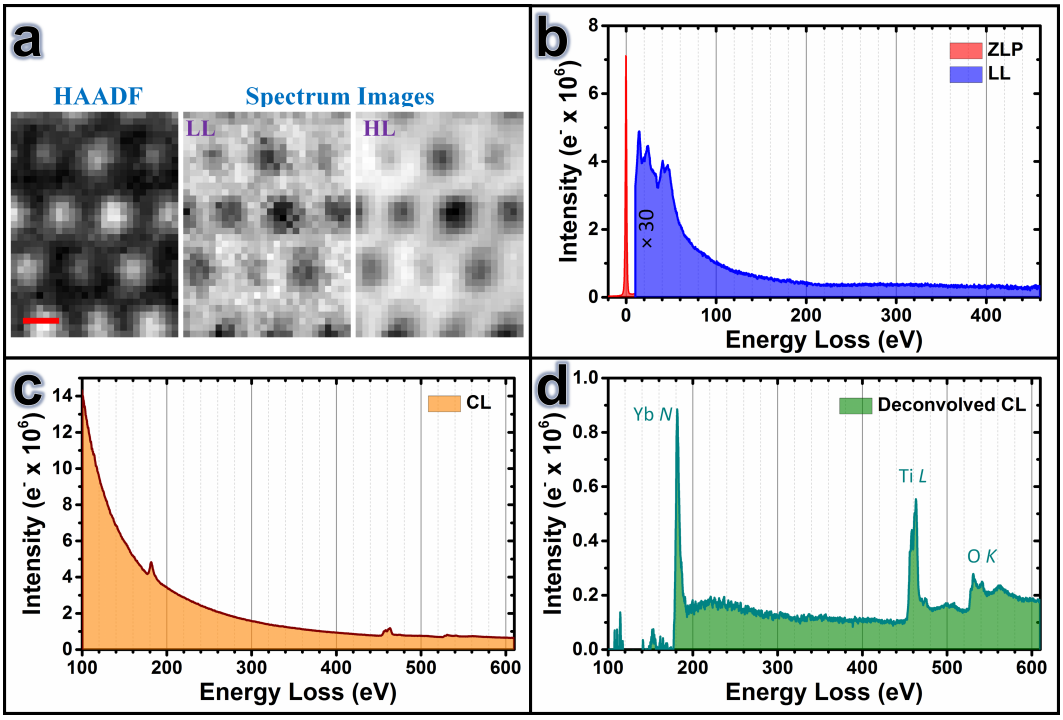

Figure 2.7: (a) HAADF and EELS spectrum images acquired from ytterbium titanate viewed along [1 1 0] (scale bar is 2 Å). (b) and (c) show the spectra calculated by averaging the LL and HL spectra presented in the spectrum images. (d) the CL spectrum shown in (c) after Fourier-log deconvolution and background subtraction calculated from the LL spectrum displayed in (b).

The log-ratio method is used to calculate the specimen thickness from the LL spectra according to the formula:

$$\frac{t}{\Lambda} = \ln \frac{I_t}{I_0} \tag{2.2}$$

where, t, Λ, I_t and I_0 are the specimen thickness, inelastic mean free path for the material in the specimen, total area under the whole spectrum and area under ZLP, respectively [127–129]. The inelastic mean free path for a specimen can be calculated from Eq. (2.3) [128, 129].

$$\Lambda = \frac{106 F E_0}{E_m \ln(2\beta E_0 / E_m)} \tag{2.3}$$

here, E_0 is the electron energy expresses in keV, F is a relativistic factor calculated from Eq. (2.4) and E_m is the average energy loss expresses in eV calculated from Eq. (2.5) [128].

Table 2.4: Parameters used to acquire EELS data.

Parameters	Spectrum	Map
Accelerating voltage	200 kcV	200 kcV
Probe size	5C (~0.5 nm)	5C (~0.5 nm)
Convergence semi-angle	29 mrad	15 mrad
Collection semi-angle	70 mrad	60 mrad
Acquisition area	10×10 nm^2	vary
Energy range	0.05 eV/ch	0.25 eV/ch

$$F = \frac{1 + E_0/1022}{(1 + E_0/511)^2} \tag{2.4}$$

$$E_m = 7.6 \left(\frac{\sum_i f_i Z_i^{1.3}}{\sum_i f_i Z_i^{0.3}} \right)^{0.36} \tag{2.5}$$

where, Z_i and f_i are the atomic number and atomic fraction of the component i present in a compound specimen [128].

2.4 ADF image simulations

Image simulation is required for the interpretation of the experimental TEM images. In the current work, image simulations for a perfect $Yb_2Ti_2O_7$ crystal (see Table 2.2) were performed with QSTEM [82] multislice software. However, STEMsim [130] multislice program was used to simulate the ADF images from stuffed ytterbium titanate crystals since a change in the occupancy of atoms in QSTEM is not straight forward.

The high-angle scattered electrons collected by the ADF detector are predominantly those scattered by phonons (i.e. thermal vibration of the atoms) [131]. Hence, the inelastic phonon excitation, known as thermal diffuse scattering (TDS) [131], is considered in the performed simulations. The number of TDS configurations, using the Einstein model [132], and other parameters which were used for image simulations are listed in Table 2.5.

Table 2.5: Parameters used for the ADF image simulations.

Parameters	QSTEM	STEMsim
Accelerating voltage	200 keV	200 keV
Convergence semi-angle	15 & 29 mrad	15 & 29 mrad
TDS	20	15
Supercell size	69.50 × 56.74 × 491.41 Å^3	52.12 × 42.56 × 200 Å^3
Slice thickness	1 Å	2 Å

2.5 Image analysis

2.5.1 Atom column intensities

Several schemes for quantitative analysis of ADF images have been proposed. LeBeau and co-workers [92] have used the maximum pixel intensity in the vicinity of the centroid of each atom image, while Van Aert and co-workers [99] assume the intensity of each atom column is a cylindrically-symmetric $2D$ Gaussian, and perform a least-squares fit. Neither of these is appropriate for the current case, where unresolved oxygen atoms lie close to the metal atoms; rather, I use intensities integrated over a Voronoi cell surrounding the atom column of interest. A Voronoi cell is an area bounded by the perpendicular bisectors of all vectors that link adjacent atom columns [85, 93, 133, 134]. The mean integrated intensity in a Voronoi cell is proportional to the scattering cross section of the atom column, while retaining a useful degree of insensitivity to exact experimental conditions such as defocus and spatial incoherence [88]. For the [2 1 1] projection, the Voronoi cell is a simple rectangle as shown in Figs. 2.1(b) and (c). Nevertheless, the contrast of atom columns may not be directly interpretable in terms of composition, e.g. due to static atomic displacements [135, 136] that may be a result of stuffing.

I developed a MATLAB program, Detect_Columns, to analyse the ADF images. A screenshot of the Detect_Columns program is displayed in Fig. 2.8. This program can perform the followings:

- find the position of each atom column using $2D$ Gaussian fitting,
- calculate the intensity of the atom columns inside the Voronoi cells or FWHM area,
- classify the atom columns according to their intensities,
- plot the intensity histograms for the atom columns,
- plot radial intensity profiles of the atom columns.

Using this program, it is possible to find columns with anomalously bright/dark contrast in comparison to their nearby columns with the same compositions. I will use this program to analyse the intensity of atom columns in ADF-STEM images in chapters 3 and 4.

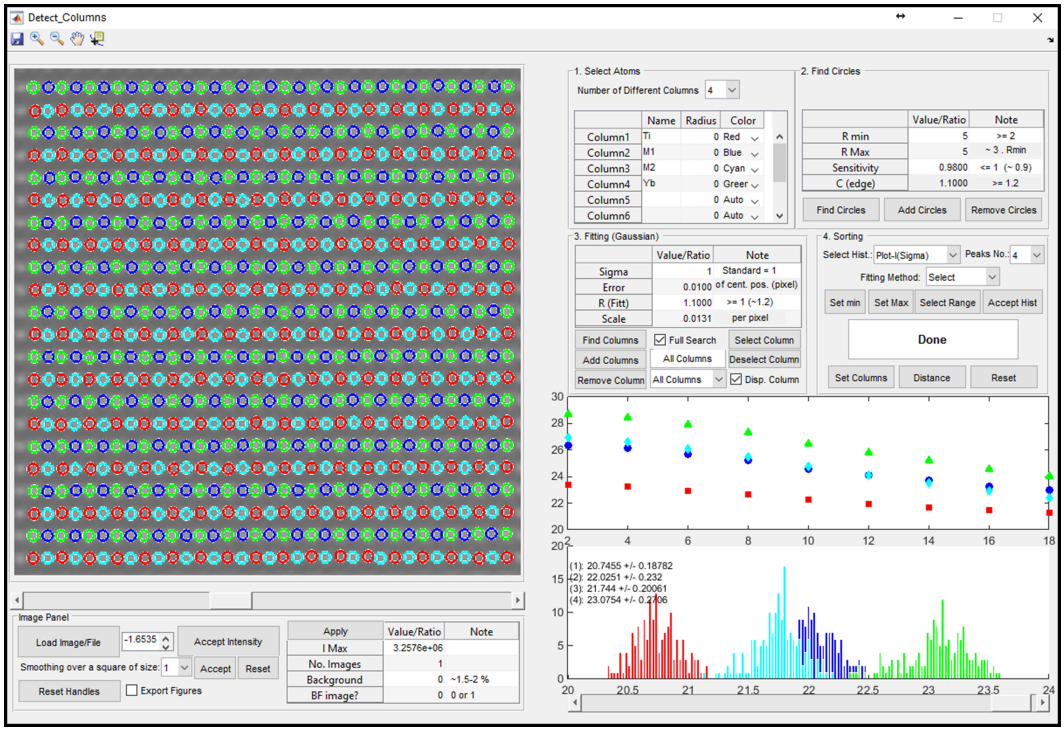

Figure 2.8: A screenshot of the Detect_Columns program used to analyse the intensity of atom column in the ADF images.

2.5.2 Defect analysis

I observed electron irradiation-induced dislocation loops in the $Yb_{1.95}Ti_2O_{7-\xi}$ sample (chapter 4). Although it is possible to calculate the Burgers vector of dislocations in HRTEM images using a simple method like Burgers circuit [137], characterization of dislocations – specially partial dislocations – in HRTEM images of materials with complex structure, like pyrochlore, using such simple methods is not possible in some cases. However, the core location and size of dislocations (even partial dislocations) can be obtained experimentally by applying a combination of geometric phase analysis (GPA), developed by Hÿtch et al. [138], and dislocation density tensor analysis on the HRTEM images of the defects in materials with complex structures [139, 140]. Hence, I will use these techniques to characterize irradiation-induced defects in chapter 4.

In the GPA technique, the displacement field, $\boldsymbol{u}$, of lattice fringes in an HRTEM image is measured with respect to a perfect lattice (unstrained part in the image) [138]. The displacement field can be measured from the phase shift in the image with respect to unstrained part in the image as follows:

$$\boldsymbol{u}(\boldsymbol{r}) = -\frac{1}{2\pi}\boldsymbol{g}^{-1}P_g(\boldsymbol{r}) \tag{2.6}$$

where $\boldsymbol{g}$ and $P_g(\boldsymbol{r})$ are the reciprocal lattice vector and phase of the local Fourier components (Geometric phase), respectively [138]. Finally, the displacement field in the real space can be calculated by choosing two reciprocal lattice vectors ($\boldsymbol{g}_1$ and $\boldsymbol{g}_2$), provided that they are non-colinear, as follows [138]:

$$\begin{pmatrix} u_x \\ u_y \end{pmatrix} = -\frac{1}{2\pi}\begin{pmatrix} g_{1x} & g_{1y} \\ g_{2x} & g_{2y} \end{pmatrix}^{-1}\begin{pmatrix} P_{g_1} \\ P_{g_2} \end{pmatrix} \tag{2.7}$$

The two-dimensional local distortion of the lattice, $\boldsymbol{e}$, and also strain field, $\boldsymbol{\varepsilon}$, in an HRTEM image can be calculated from the measured displacement fields map according to Eqs. (2.8) and (2.9) [138].

$$\boldsymbol{e} = \begin{pmatrix} e_{xx} & e_{xy} \\ e_{yx} & e_{yy} \end{pmatrix} = \begin{pmatrix} \dfrac{\partial u_x}{\partial x} & \dfrac{\partial u_x}{\partial y} \\ \dfrac{\partial u_y}{\partial x} & \dfrac{\partial u_y}{\partial y} \end{pmatrix} \tag{2.8}$$

$$\boldsymbol{\varepsilon} = \frac{1}{2}\left(\boldsymbol{e} + \boldsymbol{e}^T\right) \tag{2.9}$$

where T denotes the transpose of the matrix.

The (projected) Burgers vector of dislocation, $\boldsymbol{b}$, in an HRTEM image can be calculated as the surface ($\boldsymbol{S}$) integral of the dislocation density tensor, $\boldsymbol{a}$, around the dislocation core [139–142]:

$$\boldsymbol{b} = \iint_{\boldsymbol{S}} \boldsymbol{a}.d\boldsymbol{S} \tag{2.10}$$

where,

$$\boldsymbol{a} = \begin{pmatrix} a_x \\ a_y \end{pmatrix} = \begin{pmatrix} \dfrac{\partial e_{xx}}{\partial y} - \dfrac{\partial e_{xy}}{\partial x} \\ -\dfrac{\partial e_{yy}}{\partial x} + \dfrac{\partial e_{yx}}{\partial y} \end{pmatrix} \tag{2.11}$$

In this work, Peters's program, Strain++, [143, 144] was used to calculate the strain distribution in the ADF images containing defects. In addition, I developed another program, BurgersVectors, to calculate the dislocation density tensor of the

image, or a sub-region of it, as well as their Burgers vector. A screenshot of the BurgersVectors program is displayed in Fig. 2.9.

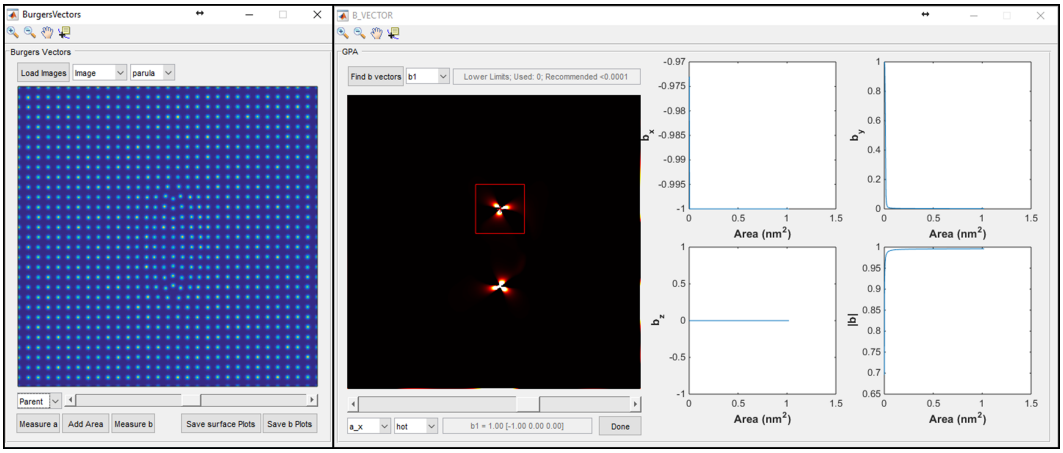

Figure 2.9: A screenshot of the BurgersVectors program; (left) simulated ADF-STEM image (by QSTEM) of a dislocation loop in Si viewed along [0 0 $\bar{1}$] and (right) calculated Burgers vector ([$\bar{1}$ 0 0]) for the top dislocation.

Chapter 3

Atomic structure study of the stoichiometric pyrochlore $Yb_2Ti_2O_7$

3.1 Introduction

This chapter describes a study of three $Yb_2Ti_2O_7$ single crystals prepared by the floating zone method with quite different low-temperature specific heat characteristics (see Section 2.1.3). The difference in the low-temperature magnetic properties of these samples is probably due to variations in structure that deviate from the nominal stoichiometry. Since the three samples all have nominally the same composition and were prepared in almost identical ways, the variation is unusual in comparison with most materials and indicates that the flexibility in the structure for $Yb_2Ti_2O_7$ is different to other materials. Hence, ac-STEM is employed to investigate the samples, in conjunction with atomically-resolved EDX and EELS. While diffraction studies, such as X-ray and neutron diffraction, measure average structure, electron microscopy at atomic resolution offers the opportunity to directly observe defects such as stuffing and atom swapping between cation sites as well as providing average measurements from regions several nm in size. It is demonstrated that there are significant differences between the samples that correlate with their magnetic behaviour. It is shown that oxygen vacancies, along with stuffing of Yb atoms onto the Ti sites, are responsible for the breakdown of the long-range magnetic ordering in $Yb_2Ti_2O_7$ pyrochlore, resulting in a material that exhibits only short-range order or in which magnetic ordering is absent down to the lowest temperatures measured.

3.2 Electron diffraction

Fig. 3.1 shows representative [1 1 0] selected area diffraction (SAD) patterns obtained from the single crystal samples as well as simulated SAD pattern for a perfect $Yb_2Ti_2O_7$ crystal. The interplanar spacing of {2 2 0}, {0 0 2} and {1 1 1} planes calculated from the SAD patterns are listed in Table 3.1. According to the electron diffraction data presented in Fig. 3.1 and Table 3.1, there is no detectable difference in the structure of the samples. As it is mentioned before, since diffraction studies measure average structure, I am using STEM at atomic resolution to study the structure of the samples locally.

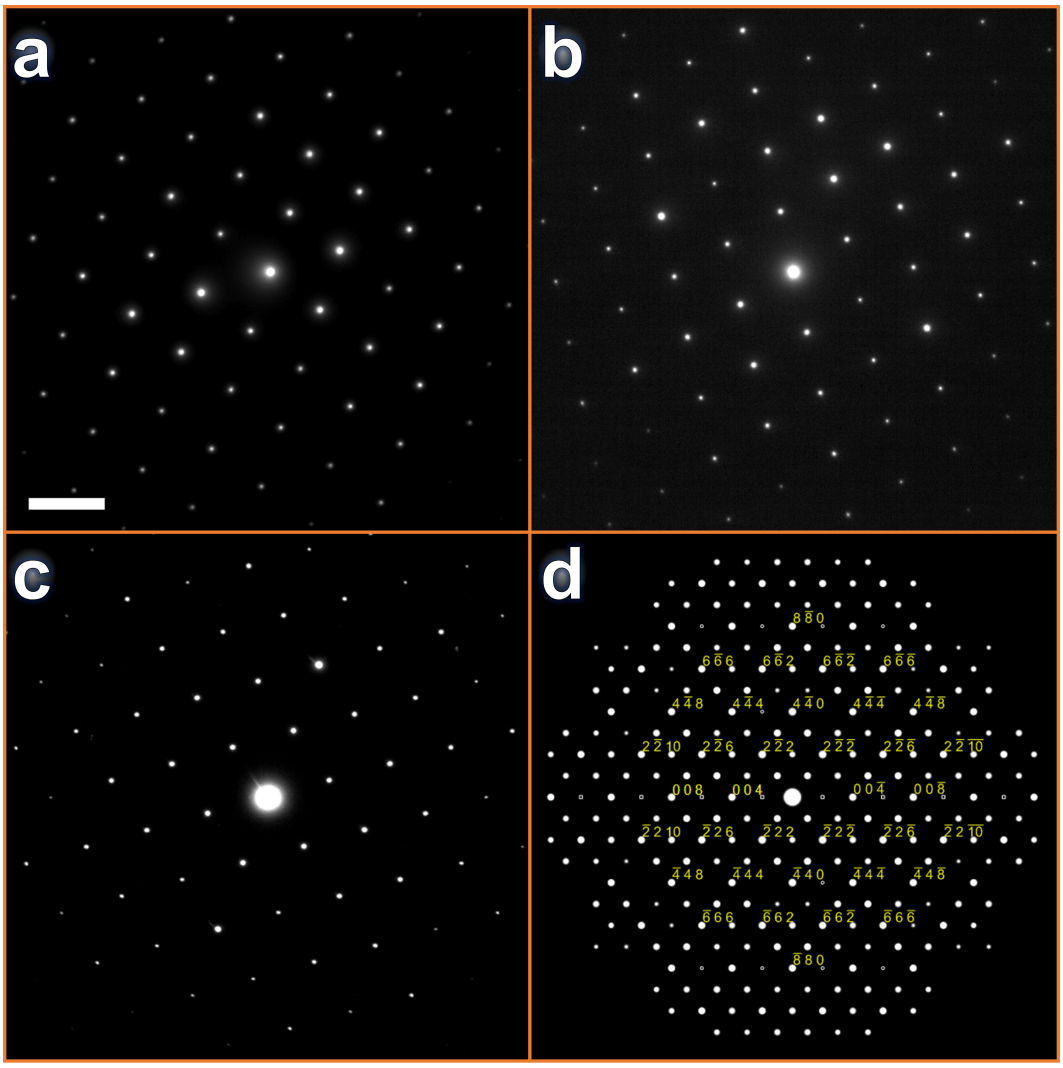

Figure 3.1: Representative [1 1 0] SAD patterns obtained from (a) sample 1 (scale bar is 2 1/nm), (b) sample 2 and (c) sample 3. (d) Simulated SAD pattern for a perfect $Yb_2Ti_2O_7$ crystal.

Table 3.1: The interplanar spacing of {2 2 0}, {0 0 2} and {1 1 1} planes calculated from the SAD patterns shown in Fig. 3.1(a-c).

Sample name	d_{220} (Å)	d_{002} (Å)	d_{111} (Å)
Sample 1	3.76 ± 0.02	5.26 ± 0.05	6.10 ± 0.06
Sample 2	3.77 ± 0.02	5.29 ± 0.05	6.13 ± 0.06
Sample 3	3.75 ± 0.02	5.35 ± 0.05	6.15 ± 0.06

3.3 STEM imaging

When the $Yb_2Ti_2O_7$ crystal viewed along [2 1 1], one set of {1 1 1} planes is seen edge-on. In this projection, as discussed in Section 1.1.1, there are four types of heavy atom column; those containing only Yb, those containing only Ti, and two different mixed columns ($M1$ and $M2$) containing 50% Ti and 50% Yb. Our interest lies in the purity of the Yb and Ti sub-lattices – and the effect on adjacent oxygen atoms – that may result from the presence of an Yb atom on a Ti site, or vice versa. Thus a simple model in which an atom column, which is nominally comprised completely of atoms of type X in perfect material, has some atoms replaced by others of type Y has been considered. Now, moving atoms between different cation sub-lattices must involve changes in oxidation state and/or anion populations in order to maintain charge balance; rearrangements of oxygen atoms or oxygen vacancies may be necessary. We will return to these points later, but begin by assuming that there is no correlation between the different substitution sites, i.e. that there is no clustering or repulsion between substituted sites and there are no vacancies, interstitials or impurity atoms. In such a simple case, with a probability p_{XY} for an atom of type X to be replaced by one of type Y, the probability of finding a column of n atoms which contains m type Y atoms is given by the binomial distribution, i.e.

$$P\binom{n}{m} = \frac{n!}{m!(n-m)!}(1-p_{XY})^{n-m}p_{XY}^{m} \tag{3.1}$$

Thus, even stuffing of a few percent should be detectable in compositional analysis sensitive to single atoms at the atomic scale (Fig. 3.2). For the [2 1 1] zone axis and a moderate specimen thickness of 45 nm, replacement of 1% gives more than 50% of atom columns that contain at least one foreign atom (yellow curve). Even if only 0.4% of atoms are replaced by a different type, more than 20% of atom columns will have one foreign atom (red curve). Conversely, unaffected columns only form a

small fraction of the image if significant amounts of stuffing occur; only 10% have no foreign atom at a stuffing of 3% (violet curve). Importantly, at stuffing fractions of a few percent, adjacent columns with widely differing substitutions should be quite common.

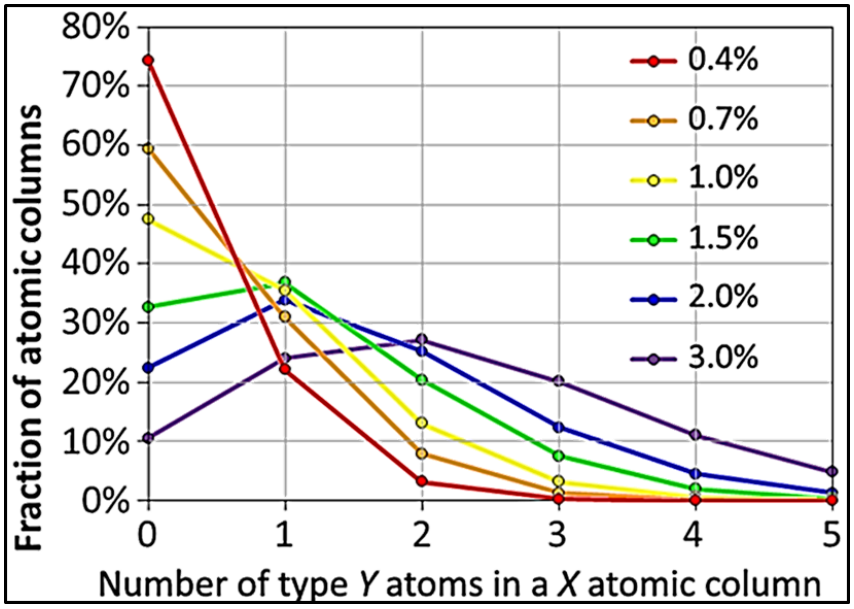

Figure 3.2: The fraction of columns with 73 atoms that have between zero and five foreign atoms predicted by (Eq. (3.1)), for different amounts of average atom swapping (0.4% to 3%). This is equivalent to a [2 1 1] $Yb_2Ti_2O_7$ specimen with thickness 45 nm.

ac-STEM images contain quantifiable composition information [83, 84] due to the atomic number sensitivity of high-angle (Rutherford) electron scattering [85–88]. Thus, it may be expected that analysis of image intensities may provide data that is sensitive to the composition of the Yb and Ti sub-lattices.

3.3.1 Annular dark-field STEM imaging

Representative [2 1 1] ADF-STEM images from the three single crystal samples are shown in Fig. 3.3(a-c), taken with an ADF detector inner angle of 2.4α. Voronoi intensity measurements for the three samples are shown in Figs. 3.3(d-i). The four sub-lattices in the ADF images, Figs. 3.3(a-c), are readily distinguished in the false colour images Figs. 3.3(d-f) and the intensity histograms Figs. 3.3(g-i). As is clearly illustrated in the histograms, the total number of electrons scattered from the $M1$ columns are more than those scattered by the $M2$ columns in all samples (see also Figs. 3.4, 3.5 and 3.6). The higher mean intensity of $M1$ in comparison with $M2$ is caused by the presence of four oxygen columns in the Voronoi cell of every $M1$

column in comparison with two for $M2$ (Fig. 2.1). Thus, even though oxygen atoms cannot be resolved in these ADF-STEM images it is clear that their effect can be seen in quantitative intensity measurements.

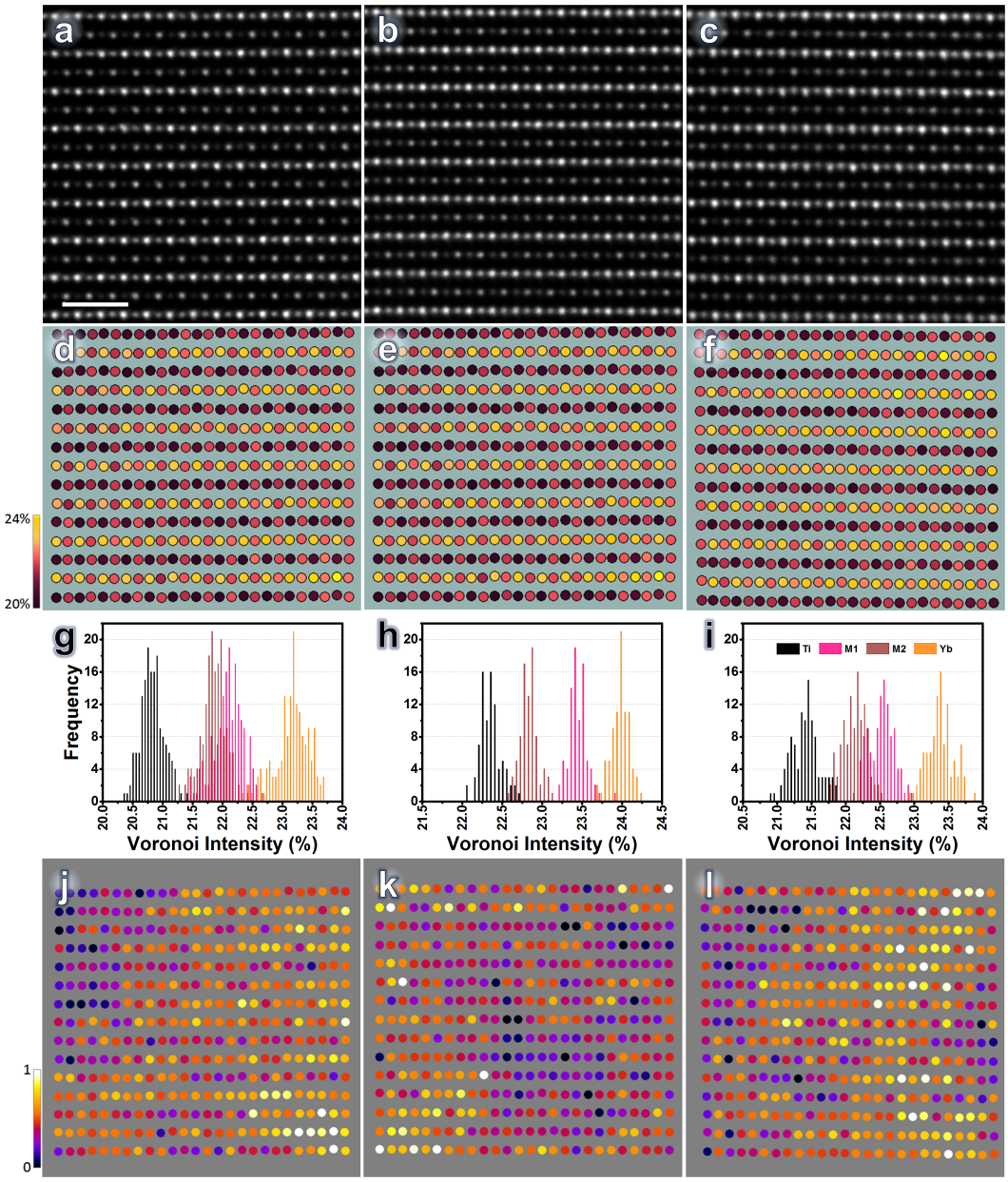

Figure 3.3: ADF-STEM images taken with an ADF detector inner angle of 2.4α, (a) sample 1, (b) sample 2 and (c) sample 3, viewed along [2 1 1] (scale bar is 1 nm). (d), (e) and (f) show extracted mean integrated intensities from (a), (b) and (c) using Voronoi cells centred on each atom column, plotted as histograms in (g), (h) and (i), respectively. Normalizing the intensities from each sub-lattice separately in (g), (h) and (i) shows the intensity variations across the images (j), (k) and (l), respectively.

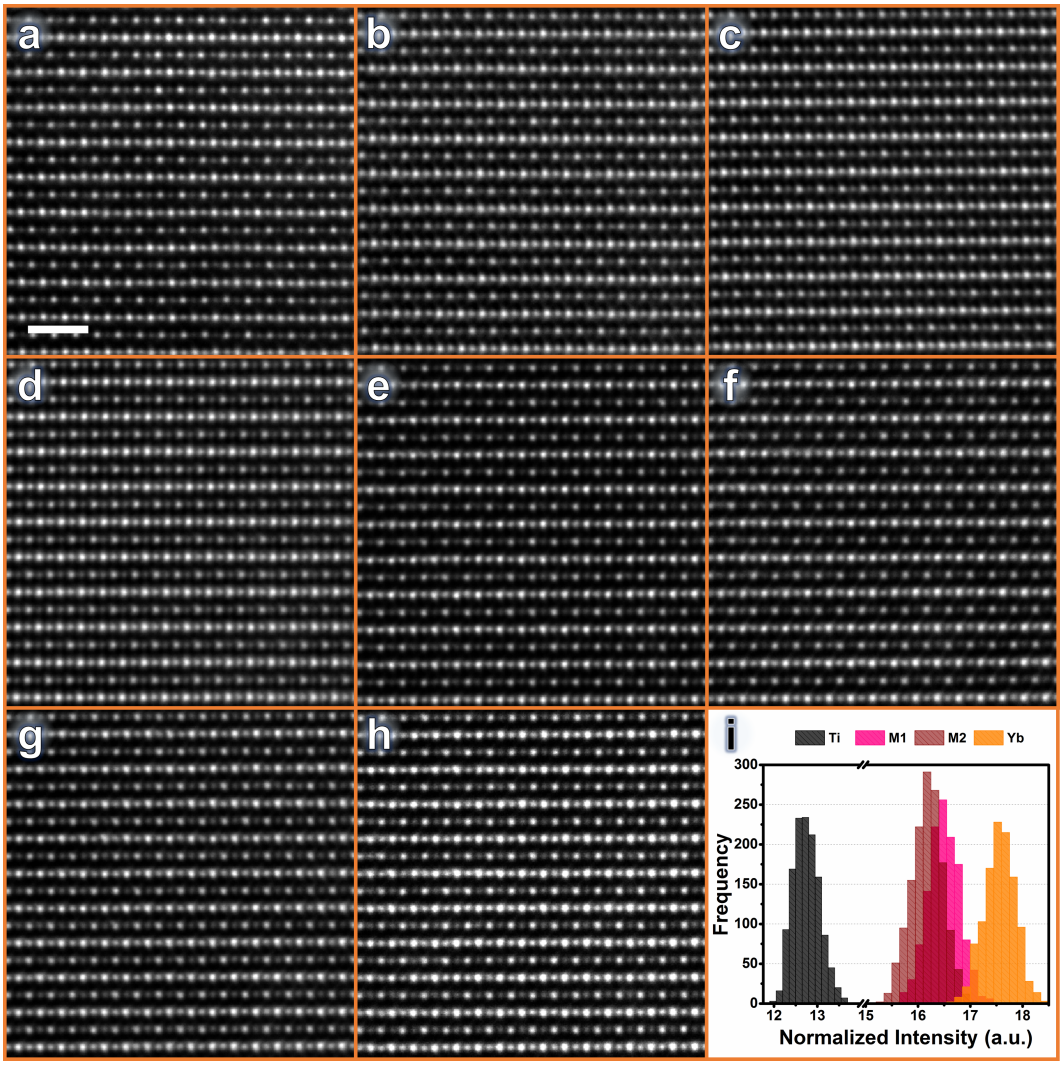

Figure 3.4: (a) to (h) ADF-STEM images taken with an ADF detector inner angle of 2.4α from different regions of sample 1. Extracted mean integrated intensities from (a) to (h) using Voronoi cells centred on each atom column are normalized and plotted as histograms in (i).

One might hope that the range of intensities in the histograms for each type of atom might be governed in some way by Eq. (3.1). However, if the four sublattice intensities are each normalized separately to a range between zero and one (Figs. 3.3(j-l)) it becomes apparent that there is a systematic variation across the ADF images, presumably due to a small variation in specimen thickness. The width of the intensity histograms in Figs. 3.3(g-i) is thus mainly caused by this thickness variation rather than atomic substitutions. These thickness variations and/or damage/contamination of the specimen surface are sufficient to mask statistical mea-

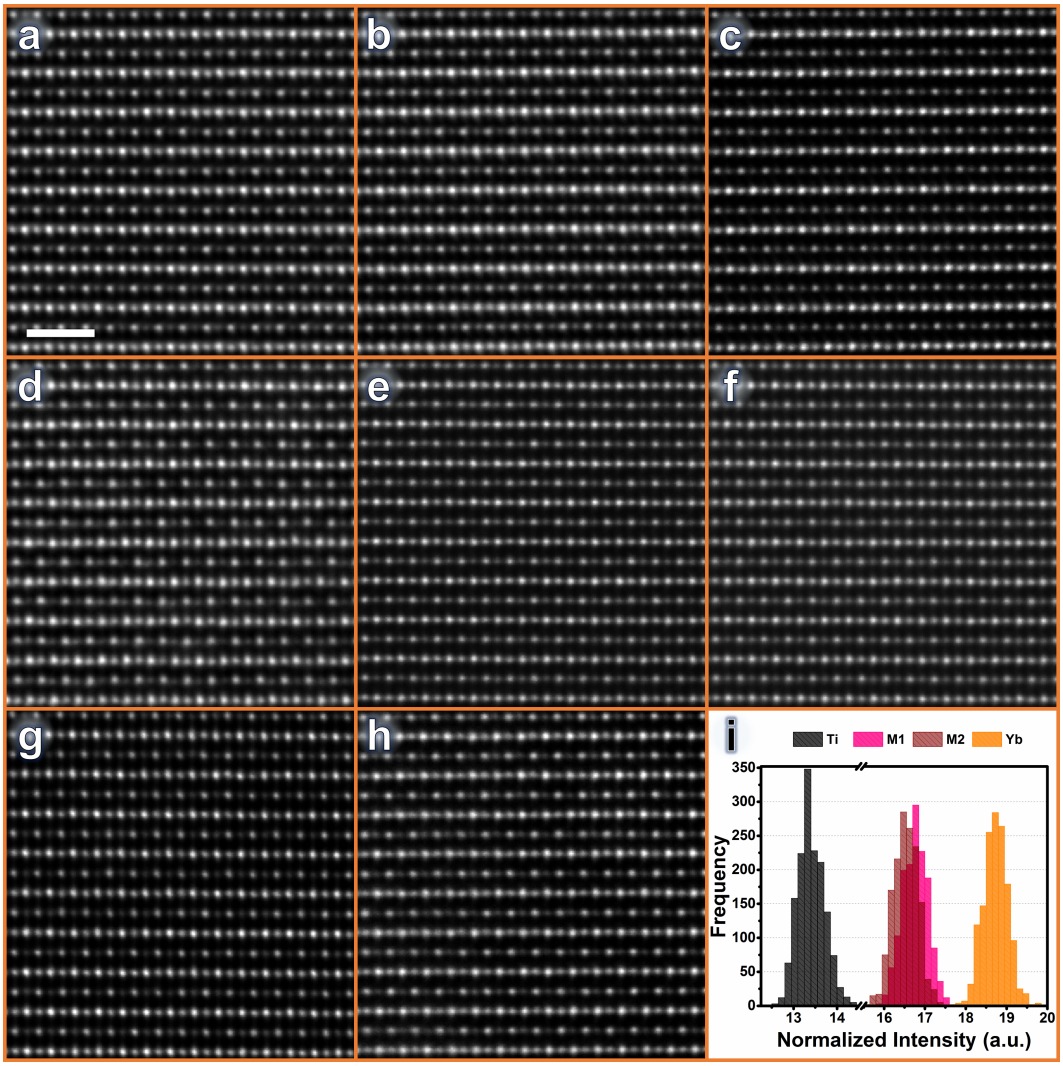

Figure 3.5: (a) to (h) ADF-STEM images taken with an ADF detector inner angle of 2.4α from different regions of sample 2. Extracted mean integrated intensities from (a) to (h) using Voronoi cells centred on each atom column are normalized and plotted as histograms in (i).

surements of stuffing, or anti-stuffing, from the ADF intensities of atom columns, i.e. changes in the number of atoms per column n (Eq. (3.1)) easily produce differences that are equal to or larger than the effect of a few atomic substitutions.

The difference in $M1$ and $M2$ column intensities indicates a sensitivity of ADF data to nearby oxygen atoms. I therefore investigated mean radial intensity as a function of distance from the centre of the visible atom columns (Fig. 3.7), averaged over all equivalent columns in the images of Figs. 3.3(a-c). These mean radial intensity profiles are shown in Figs. 3.8(a-c), where the centre of the atom column is

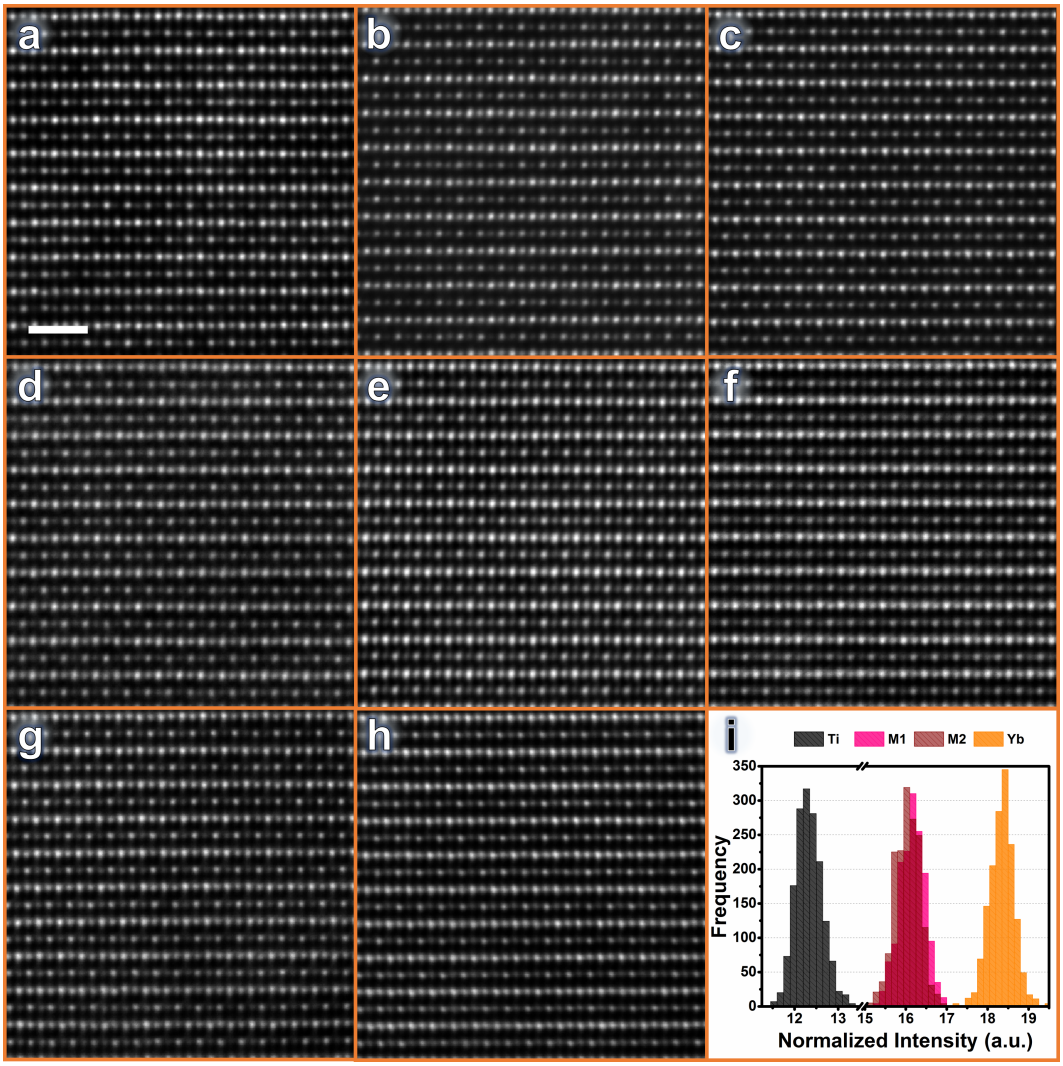

Figure 3.6: (a) to (h) ADF-STEM images taken with an ADF detector inner angle of 2.4α from different regions of sample 3. Extracted mean integrated intensities from (a) to (h) using Voronoi cells centred on each atom column are normalized and plotted as histograms in (i).

at the origin and the mean radial intensity decays following a quasi-Gaussian profile. In sample 1, the $M2$ columns have a higher peak intensity (Fig. 3.8(a)), consistent with oxygen atom columns close to their centres (49 pm in the nominal structure). The radial intensity of the $M1$ columns decays more slowly, consistent with more oxygen atom columns at larger distances (72 pm in the nominal structure). The intensity of $M1$ columns exceeds that of $M2$ columns at a radius of $\sim$65 pm. To provide a clear understanding, Fig. 3.9 illustrate this trend for only a pair of $M1$ and $M2$ atom columns in the ADF image of sample 1. The same trend is observed in

ADF images obtained from other areas of sample 1 at different sample thicknesses (Fig. 3.8(d)) as well as multislice simulations of the nominal $Yb_2Ti_2O_7$ structure (Fig. 3.10(b)), with the intensity at $M2$ columns becoming smaller than that of $M1$ columns at a certain radius depending the sample thickness.

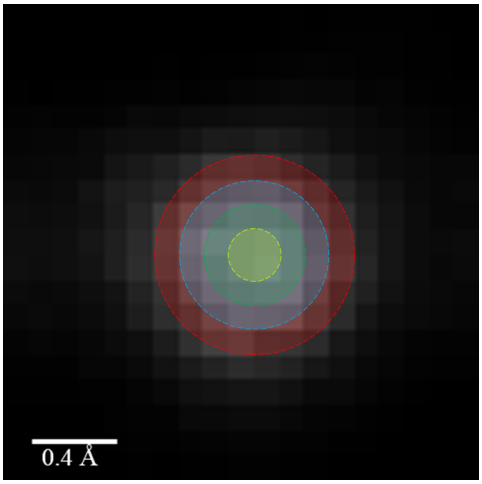

Figure 3.7: Circles with different radii (yellow, 0.013 nm; green, 0.026 nm; cyan, 0.039 nm; red, 0.052 nm) from the center of an atom column. The radial intensity corresponds to each radious is measured as the mean intensity of all pixels inside each circle.

In contrast, the radial intensity of the $M2$ columns never exceeds that of $M1$ columns for samples 2 and 3 (Figs. 3.8(b), (c), (e) and (f)). This effect could be caused by fewer oxygen atoms in the Wyckoff f-site or their movement away from $M2$ columns, which would reduce the $M2$ intensity at small radii, and/or movements of f-site and b-site oxygen atoms closer to $M1$ columns, which would increase their intensity at small radii.

3.3.2 *Z* contrast imaging

Although a statistical analysis of atom column composition is not possible due to the variations in intensity over several nm (Fig. 3.3), individual atom columns that have anomalous bright or dark contrast in comparison with their immediate neighbours (with the same nominal composition) may still be detected in compositionally-sensitive STEM images. Thus, the Z contrast (HAADF) imaging technique can be used to investigate whether the samples exhibit stuffing or not. Hence, HAADF data were collected with an ADF detector inner angle at least 4.6 times α. Considering that in the $Yb_2Ti_2O_7$ crystal all Yb as well as Ti atoms are crystallographically equivalent and Yb atoms ($Z^2 = 4900$) have higher contribution to the image contrast in comparison with Ti atoms ($Z^2 = 484$), the intensity changes of Yb and Ti

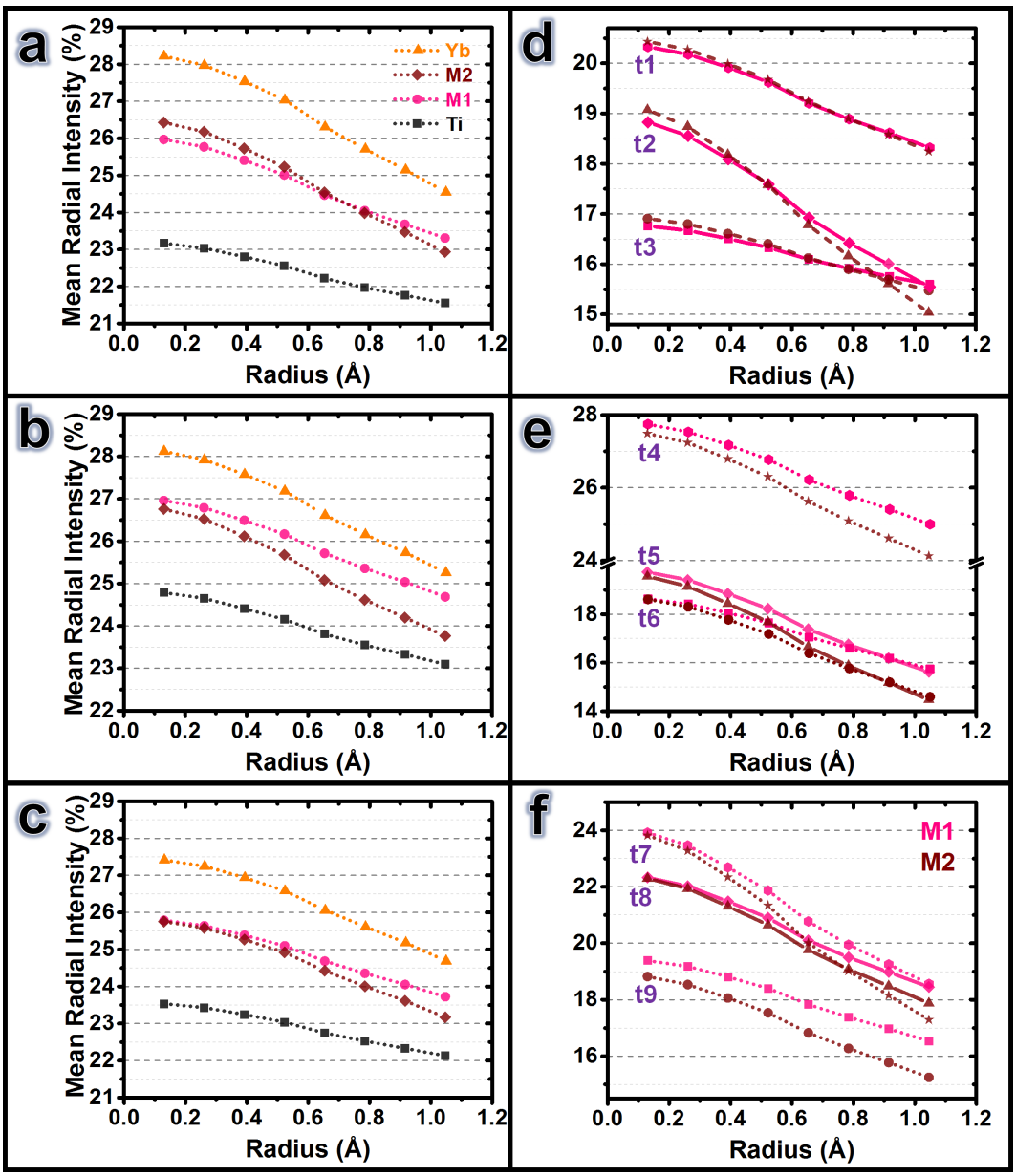

Figure 3.8: (a), (b) and (c) show mean radial intensity profiles for the ADF-STEM images illustrated in Fig. 3.3(a) (sample 1), Fig. 3.3(b) (sample 2) and Fig. 3.3(c) (sample 3), respectively. (d), (e) and (f) show mean radial intensity profiles of the $M1$ amd $M2$ columns for ADF images obtained from sample 1, sample 2 and sample 3 at different sample thicknesses (t1 to t9), respectively.

columns is examined to find whether any Yb (Ti) atom occupied Ti (Yb) site in the samples or not.

In the ADF images obtained from both sample 2 and sample 3, a significant drop was observed in the peak intensity of some Yb columns in comparison to that

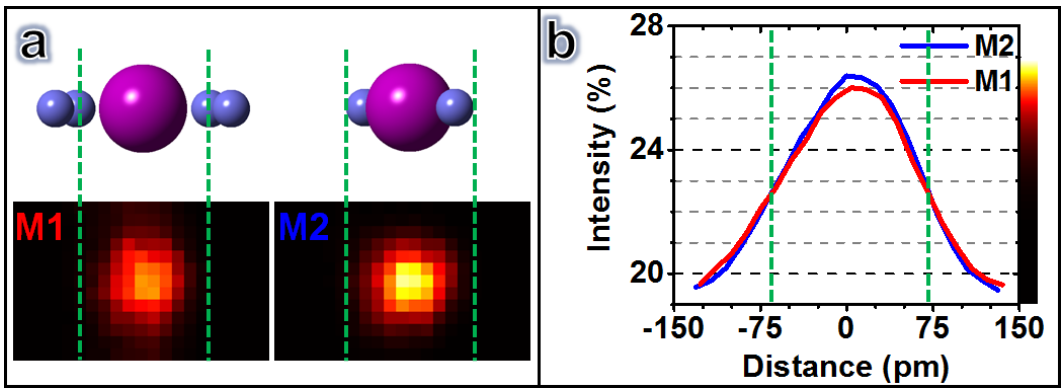

Figure 3.9: (a) [2 1 1] projection of oxygen atoms (blue) around the $M1$ and $M2$ columns (magenta) in the nominal $Yb_2Ti_2O_7$ structure. The $M2$ column has two oxygens 49 pm away in this projection, while $M1$ has four, at 72 pm and 95 pm. Dotted green lines at ~72 pm on these models and the ADF-STEM images below match those in (b), a plot of intensity of these columns. The peak intensity is higher for $M2$ while $M1$ has higher intensity tails.

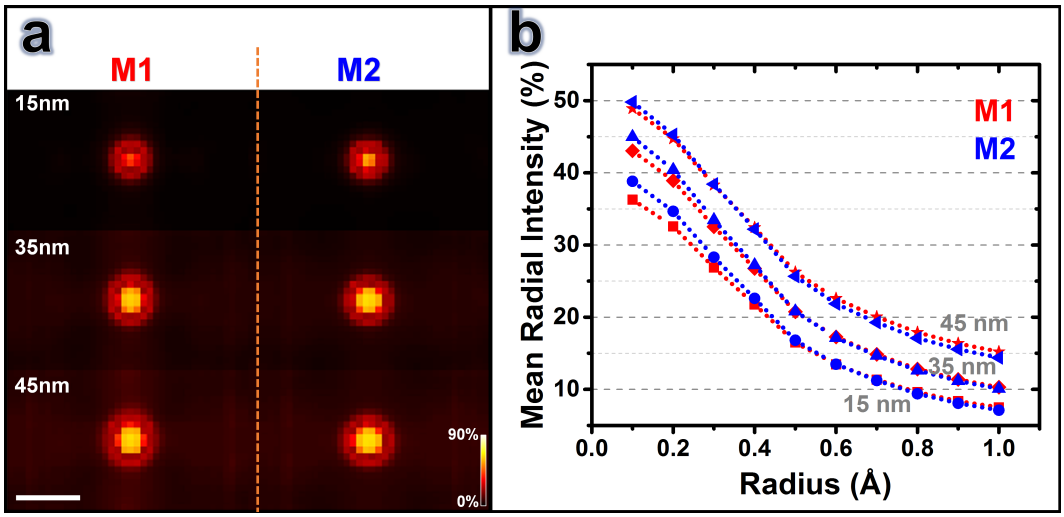

Figure 3.10: (a) The ADF-STEM simulated images of M columns for a perfect $Yb_2Ti_2O_7$ crystal at different thicknesses (scale bar is 1 Å) and (b) mean radial intensity profiles of the M columns shown in (a).

of their immediate neighbours with the same nominal composition (Fig. 3.11). It might be suggested that all of the Yb sites in the Yb columns showing relatively low peak intensity are not occupied by Yb atoms meaning a fraction of Yb sites is either occupied by light atoms (e.g. Ti) or not occupied at all (Yb vacancies). On the other hand, the Voronoi intensity results (drop down lines in Fig. 3.11) indicate there is no large difference in the composition of those anomalously dark Yb columns and their neighbouring Yb columns. Thus, another possibility is that there is no compositional difference among the Yb columns in these samples but a number of

atoms in those dark Yb columns are displaced from their nominal positions (i.e. static atomic displacements or atomic-level strain).

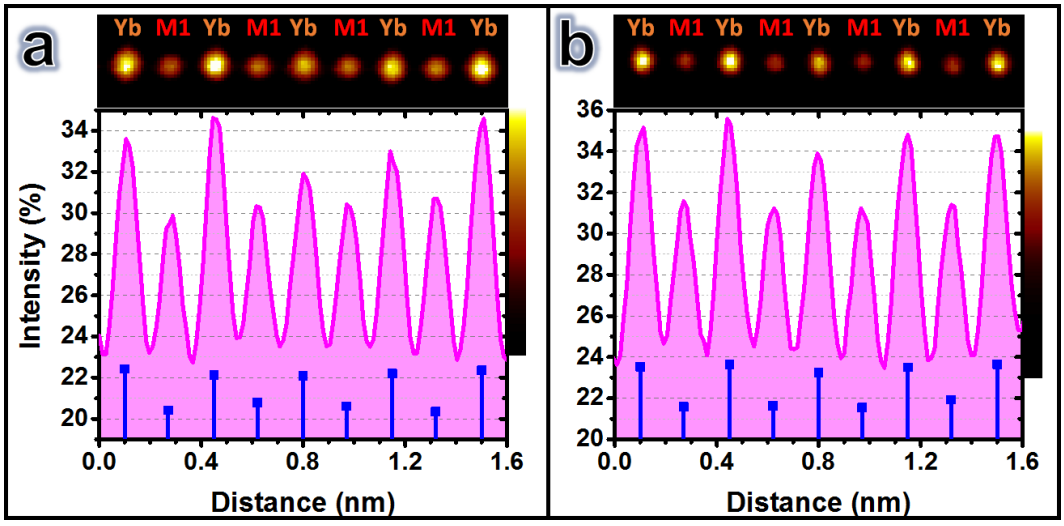

Figure 3.11: [2 1 1] ADF-STEM images, taken with an ADF detector inner angle of 4.6α, from Yb columns exhibiting anomalously weak intensity and their corresponding intensity profiles for (a) sample 2 and (b) sample 3. The calculated Voronoi intensity for each atom column is displayed by a blue drop down line.

In order to examine the above mentioned proposals and, therefore, find the origin of such changes in the peak intensity of Yb columns, ADF-STEM image simulations of Yb columns having the nominal crystallographic parameters, stuffed Ti atom(s) and atomic-level strain were performed at different thicknesses (Fig. 3.12). As illustrated in the intensity profiles of the simulated ADF images, Fig. 3.12, introduction of either the stuffed Ti atoms or atomic-level strain to a perfect Yb column considerably decreases the column peak intensity. However, these imperfections do not considerably affect the column's Voronoi intensity especially when the sample is relatively thick. Although these experimental and simulation data failed to show whether any Yb site is occupied by a Ti atom in sample 2 as well as sample 3, they reviled the fact that the Yb sub-lattice is imperfect in both samples.

In the ADF images obtained from sample 3, apart from anomalously dark Yb columns, anomalously bright Ti columns were observed. As is clearly seen in Fig. 3.13(a), in comparison to adjacent Ti columns, not only does the Ti column marked with an asterisk exhibit higher peak intensity but also it shows significantly higher Voronoi intensity. Furthermore, as displayed in Fig. 3.13(b), this Ti column demonstrates anomalously dark contrast in the BF image, acquired simultaneously with the ADF image shown in Fig. 3.13(a). These results, together with the ADF image simulation results, indicate that the substitution of Yb atoms on Ti sites lead

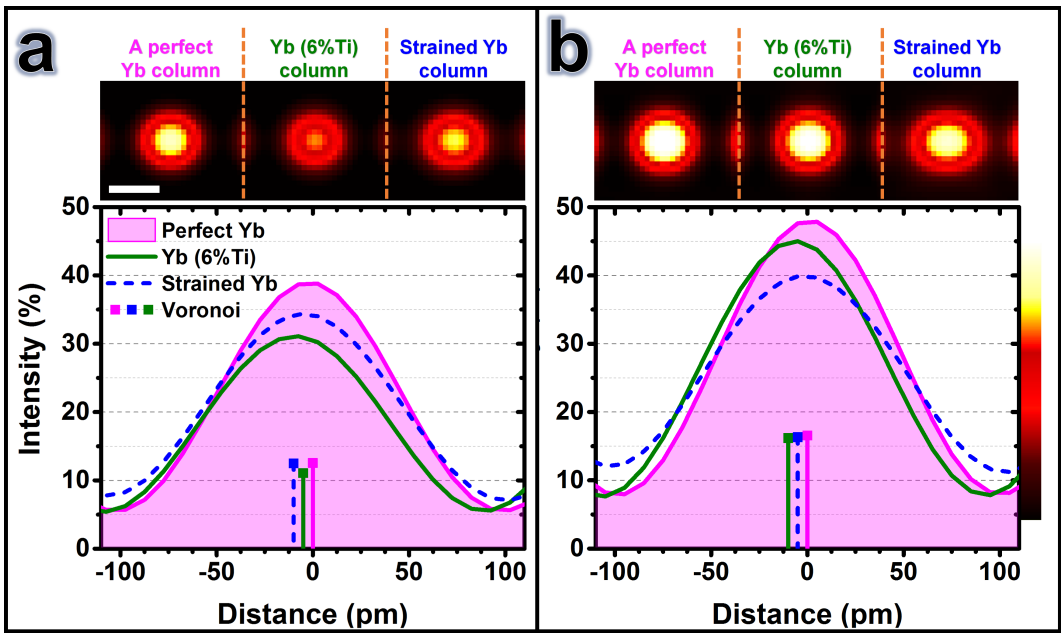

Figure 3.12: Simulated [2 1 1] ADF-STEM images (scale bar is 1 Å) and their corresponding intensity profiles from a perfect Yb column, a Yb column containing 6% Ti atoms and a Yb column in which 20% of its atoms are displaced by 0.242 Å along [1 1 1] direction at thicknesses of (a) 10 nm and (b) 20 nm. The Voronoi intensity corresponding to each atom column is displayed by a drop down line in the intensity plots.

to a significant increment in both the peak and Voronoi intensities of Ti columns (Fig. 3.14), are consistent with this proposal that a fraction of Ti sites has been occupied by heavy atoms (e.g. Yb) in sample 3. However, analytical techniques such as EDX and EELS are required to prove whether those stuffed atoms are Yb or not.

3.4 EDX

Sample 3 is the most likely of the three samples to exhibit stuffing according to its low-temperature magnetic properties (see Section 2.1.3). Atom columns with anomalous contrast in comparison with their neighbours in ADF images were observed, as shown in Figs. 3.11 and 3.13. Anomalously bright Ti columns, consistent with stuffing of Yb onto Ti sites were observed as well as anomalously dark Yb columns, consistent with anti-stuffing of Ti onto Yb sites or atomic level strain, were examined with atomic resolution EDX. Fig. 3.15(a) shows an EDX line scan across an anomalously bright Ti column, made using Ti $K\alpha$ (4.51 keV) and Yb $L\alpha$ (7.41 keV) X-rays. There is an obvious drop in Ti signal, and an increase in the

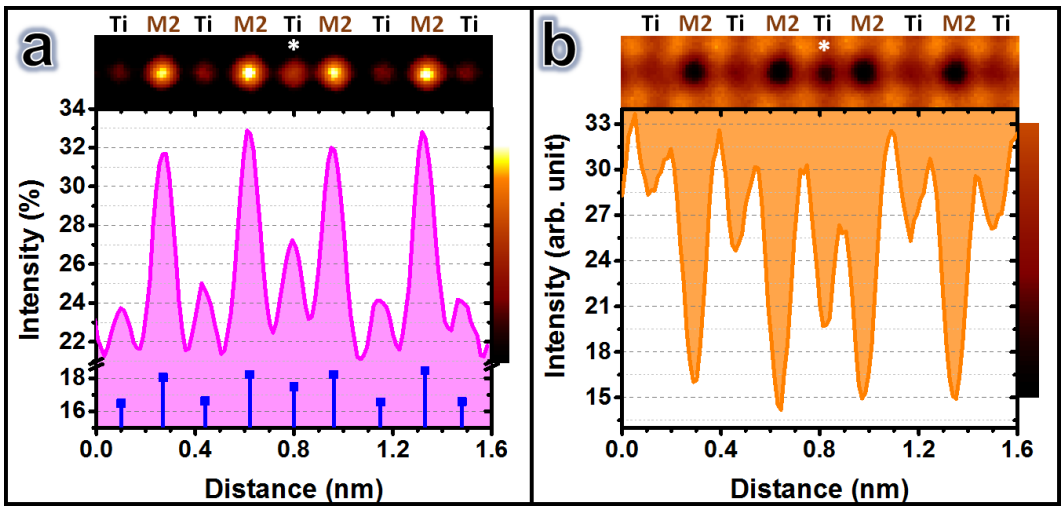

Figure 3.13: (a) Anomalously bright intensity from a Ti column marked with an asterisk in the [2 1 1] ADF-STEM image, taken with an ADF detector inner angle of 4.6α from sample 3. The calculated Voronoi intensity for each atom column in the ADF image is displayed in the intensity profile by a blue drop down line and (b) the BF image, acquired simultaneously with the ADF image shown in (a), and its corresponding intensity profile.

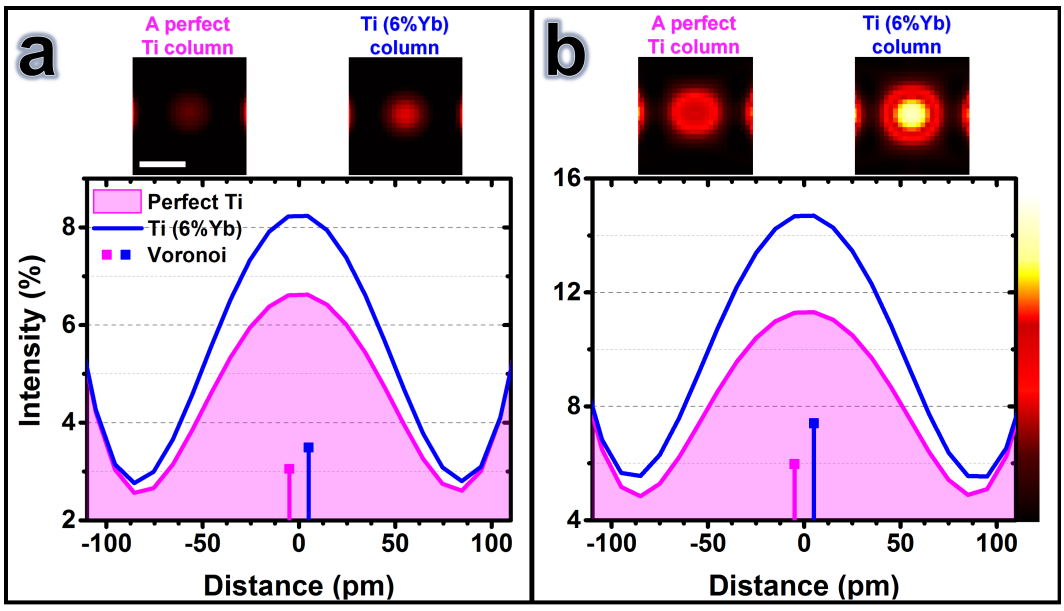

Figure 3.14: The simulated [2 1 1] ADF-STEM images (scale bar is 1 Å) and their corresponding intensity profiles from a perfect Ti column and a Ti column containing 6% Yb atoms at thicknesses of (a) 10 nm and (b) 20 nm. The Voronoi intensity corresponding to each atom column is displayed by a drop down line in the intensity plots.

Yb signal, for the brighter column in comparison with the others, particularly those to the left. The correlation between bright atom column contrast and a lower Ti /

higher Yb signal was observed several times and is direct evidence for stuffing in this sample (see also the atomic scale EDX map from sample 3 displayed in Fig. 3.16). Fig. 3.15(b) shows a line of Yb-$M2$ columns, in which a small Ti signal can be seen at each Yb column as well as the expected signal at the $M2$ columns. While this may indicate anti-stuffing of Ti onto Yb sites, it is also possible that a small amount of specimen drift (0.2 nm) during acquisition introduced some signal from the adjacent Ti-$M1$ row of atoms.

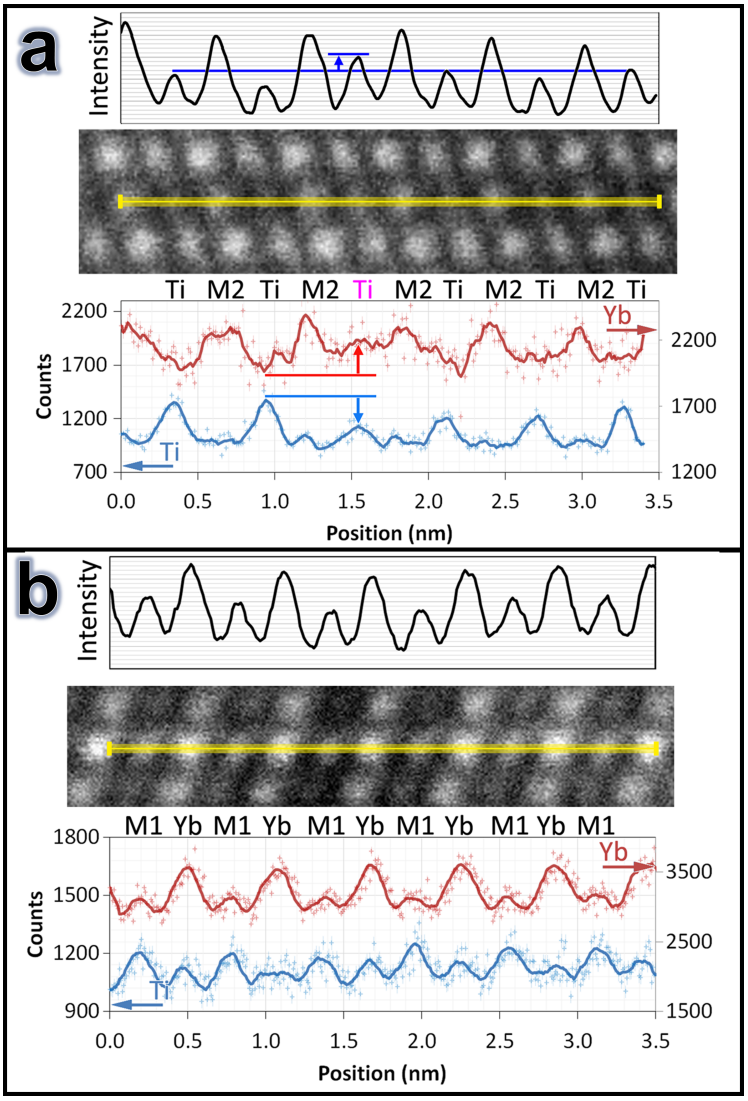

Figure 3.15: EDX analysis of sample 3. (a) Atomic scale EDX analysis along a line of Ti and $M2$ atom columns, showing a decrease in Ti signal and increase in Yb signal at an anomalously bright Ti atom column. (b) Atomic scale EDX analysis along a line of Yb and $M1$ atom columns.

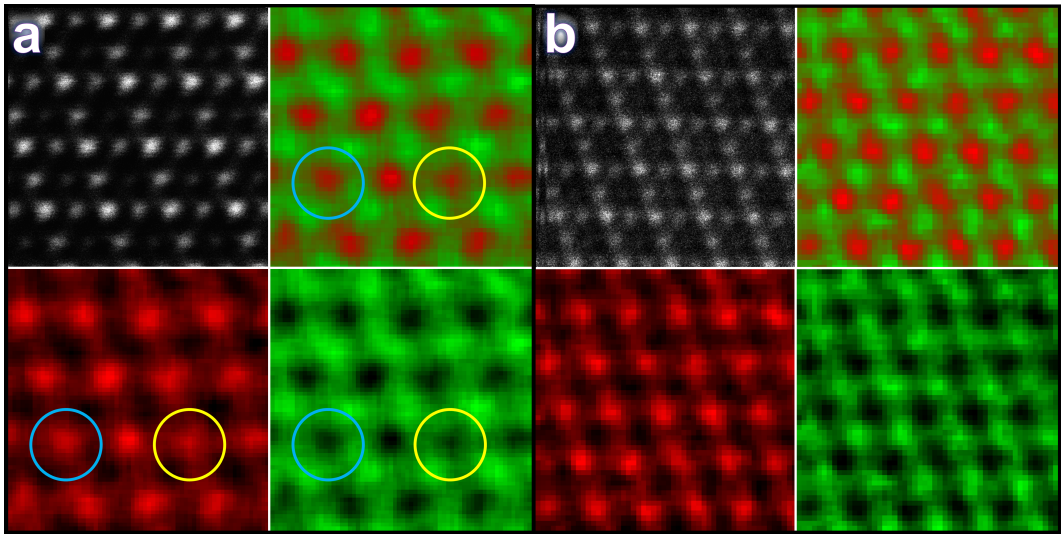

Figure 3.16: Atomic scale EDX maps from (a) sample 3 and (b) sample 2; Yb and Ti are shown in green and red, respectively. Those Ti columns marked by circles in (a) show Yb signals as well as a decrease in Ti signal which can be as a result of Yb atom(s) on the Ti site(s) in sample 3.

3.5 EELS

Analysis of $Yb_2Ti_2O_7$ at atomic resolution using EELS is possible using the Ti-$L_{3,2}$ edge at ~450 eV and the Yb-$N_{4,5}$ edge at 185 eV, although spatial resolution is limited for the latter due to delocalization effects [115], limiting the analysis to the [1 1 0] zone axis. Nevertheless, ELNES spectra can be used to obtain information on Ti bonding configurations [145–147]. Metallic Ti shows two white lines L_3 and L_2 at 456 eV and 462 eV, due to electron transitions from $2p_{3/2}$ and $2p_{1/2}$ subshells to unoccupied $3d$ states respectively. In titanium oxides, the number of peaks in the Ti-$L_{3,2}$ ELNES spectrum depends on valence state, coordination and site symmetry of the Ti atoms [146]. In materials with a Ti oxidation state of +4, like $Yb_2Ti_2O_7$, titanium core-holes created by excitation of $2p$ core electrons can be poorly screened since there is no electron in the Ti^{4+} conduction band. Consequently, both L_3 and L_2 edges are shifted to higher energy losses than for metallic Ti [146]. Octahedral coordination of Ti atoms with oxygen splits the degenerate unoccupied $3d$ states into a lower energy $2t_{2g}$ molecular energy level and a higher $3e_g$ level [148]. Hence, in $Yb_2Ti_2O_7$ the Ti L_3 and L_2 edges both consist of two white lines, α and β for L_3 and γ and δ for L_2. In fact, for each edge the first (α, γ) and second (β, δ) peak are due to transitions from the $2p$ state to the $2t_{2g}$ (π^*) and $3e_g$ (σ^*) oxide levels, respectively.

A decrease in Ti valence, for example due to oxygen vacancies, has two effects on

Ti-$L_{3,2}$ ELNES: a) a systematic shift to lower energies of ~2 eV per valence state [146]; and b) the intensity ratios I_β/I_α, I_δ/I_γ and I_β/I_δ all trend to larger values [145, 146]. These changes are very sensitive indicators of change in Ti valence.

The experimental Ti-$L_{3,2}$ spectra from the three samples are shown in Fig. 3.17(a). Peak energies, extracted by fitting the data to four Lorentzian curves (Fig. 3.17(b)), as well as intensity ratios are listed in Table 3.2.

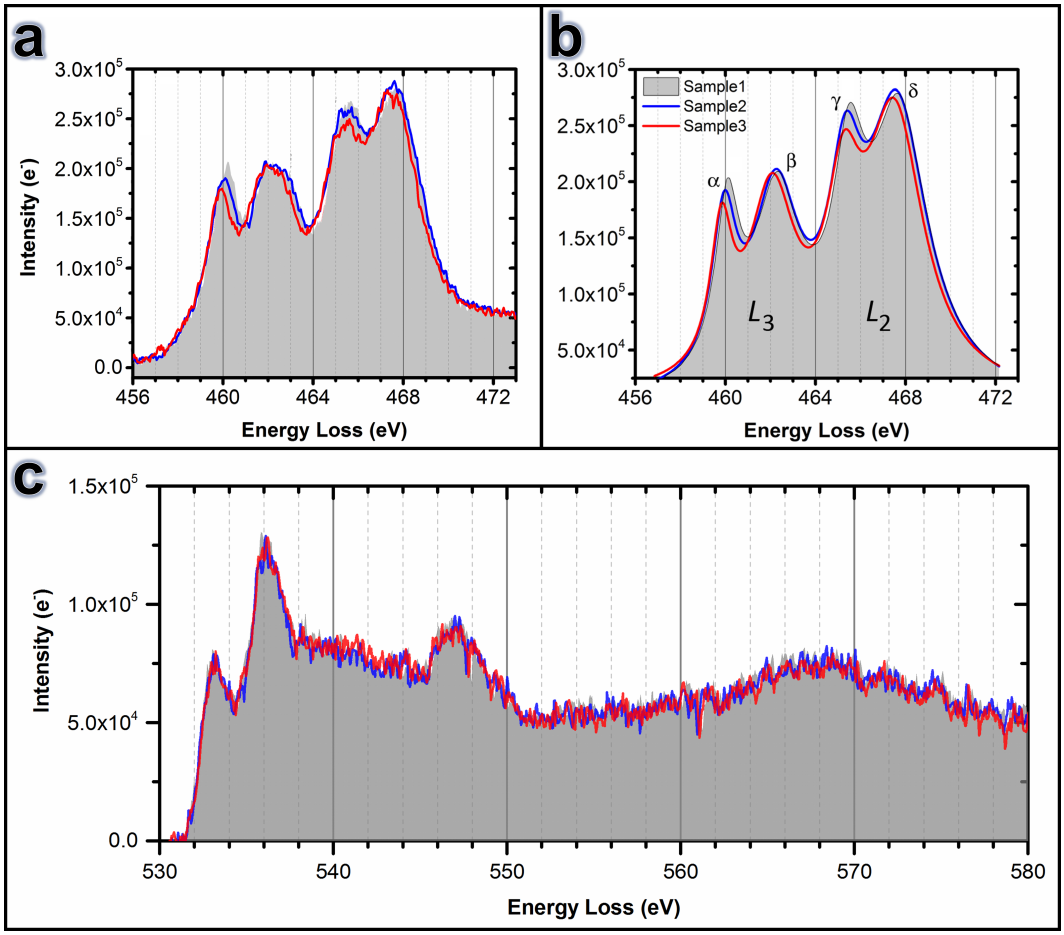

Figure 3.17: (a) Experimental EELS Ti-$L_{3,2}$ spectra of the three samples ($t/\Lambda = 0.30$). (b) Lorentzian curves fitted to the experimental EELS spectra shown in (a). (c) Experimental EELS O-K spectra of the three samples ($t/\Lambda = 0.30$).

A systematic shift in the Ti-$L_{3,2}$ edge to lower energies as well as an increase in the intensity ratios I_β/I_α, I_δ/I_γ and I_β/I_δ from sample 1 to 3 are observed (see also Fig. 3.18). However, as illustrated in Fig. 3.17(c), there is no detectable difference in the O-K spectra obtained from the samples. All of these indicators show that the Ti valence drops from sample 1 to sample 2 and still further for sample 3.

Table 3.2: Ti ELNES energies and intensity ratios for the three $Yb_2Ti_2O_7$ samples (t/Λ = 0.30).

		Sample 1	Sample 2	Sample 3
L_3	E_α	460.08 ± 0.01	459.94 ± 0.01	459.82 ± 0.01
	E_β	462.32 ± 0.02	462.23 ± 0.02	462.06 ± 0.02
	I_β/I_α	2.13 ± 0.13	2.33 ± 0.13	2.91 ± 0.17
L_2	E_γ	465.48 ± 0.02	465.32 ± 0.02	465.24 ± 0.02
	E_δ	467.74 ± 0.02	467.63 ± 0.02	467.52 ± 0.02
	I_δ/I_γ	2.64 ± 0.15	3.13 ± 0.19	2.96 ± 0.18

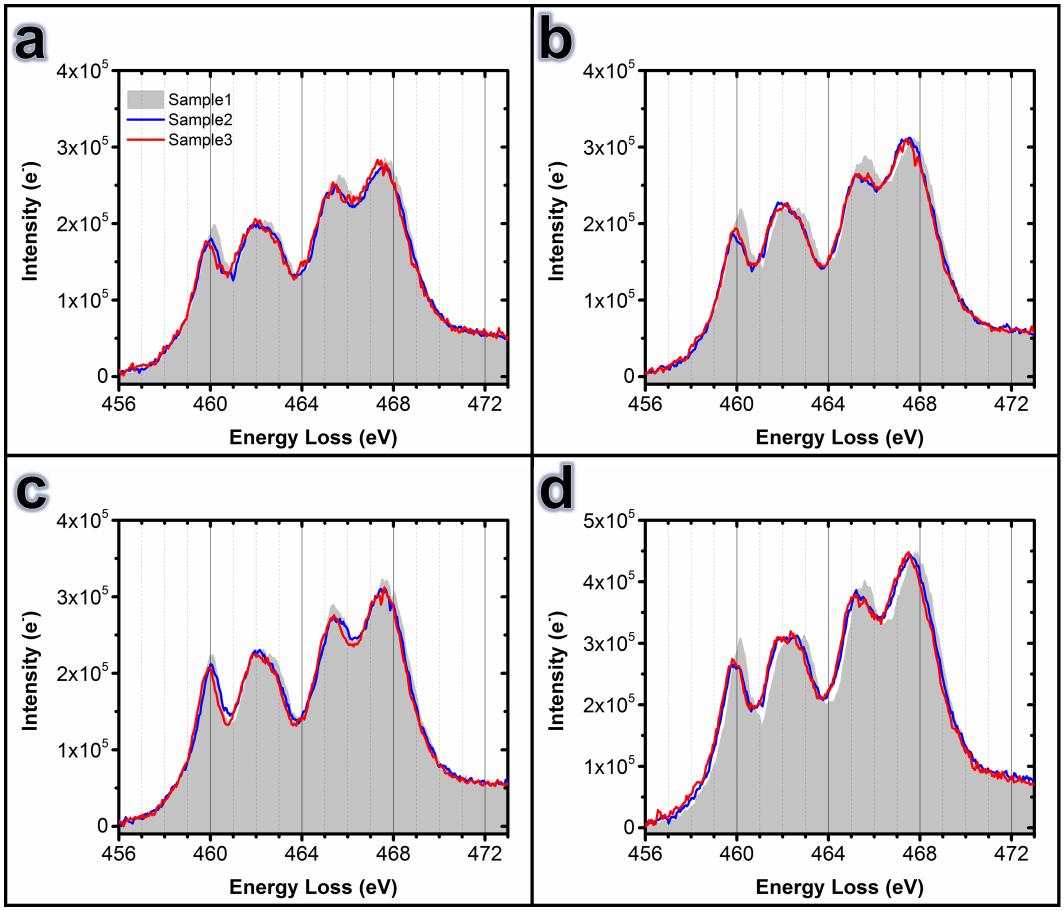

Figure 3.18: Experimental EELS Ti-$L_{3,2}$ spectra of the three samples acquired at different sample thickness; (a) $t/\Lambda = 0.31$, (b) $t/\Lambda = 0.37$, (c) $t/\Lambda = 0.42$ and (d) $t/\Lambda = 0.58$.

3.6 Discussion

The above results are in agreement with the previous studies of $Yb_2Ti_2O_7$ that found evidence for Yb stuffing onto Ti sites even in nominally stoichiometric material, and that more stuffing correlates with more diffuse peaks in specific heat

capacity. Ross et al. [38] discounted oxygen vacancies as the structural origin of the varying magnetic behaviour of $Yb_2Ti_2O_7$, based on the lack of change in materials subjected to long anneals in an oxygen-rich environment. However, here we find changes in Ti valence that indicate an increasing oxygen vacancy content as stuffing and/or cation site swapping increases from sample 1 to 3, and this correlates with the changes in magnetic behaviour. These apparently contradictory findings can be reconciled by noting that, on average, replacing two Ti^{4+} atoms by Yb^{3+} will be balanced by one O^{2-} vacancy if the Yb sub-lattice remains unchanged. Stuffing therefore may change the equilibrium oxygen stoichiometry in $Yb_2Ti_2O_7$, which is quite different to a non-equilibrium oxygen deficiency that can be remedied by annealing.

The EELS data (Figs. 3.17 and 3.18) thus show a correlation between magnetic properties and oxidation state. In order to link this to the differences in intensity profiles we observe in ADF-STEM data (Fig. 3.8), and the effects of stuffing, it is necessary to consider the position of the oxygen atoms in the crystal structure. One way to do this is to divide the crystal into regular tetrahedral and octahedral volumes (Fig. 3.19). Each cation sits at the vertex of six edge-sharing tetrahedra and six corner-sharing octahedra. These are shown for an Yb atom in Figs. 3.19(a) and (b); the octahedra are empty, while each tetrahedron contains an oxygen atom. There are two types of tetrahedron around an Yb atom, shown in coloured shading in Fig. 3.19(b); two tetrahedra are comprised of four Yb^{3+} ions, $4Yb$, with a Wyckoff b-site O^{2-} atom at their centres (green), while the remaining six (purple) have two Yb and two Ti atoms, $2Ti2Yb$, and a Wyckoff f-site O^{2-} atom, displaced well off-centre, close to the mid-point of the edge connecting the Ti atoms. A similar structure surrounds the Ti atoms, except in this case there are six $2Ti2Yb$ tetrahedra and two $4Ti$ tetrahedra, comprised of four Ti^{4+} ions with no oxygen atom inside.

Stuffing will change all eight tetrahedra that surround the affected site. A possible structure that results from replacing a Ti^{4+} atom with Yb^{3+} is shown in Fig. 3.19(d). The six $2Ti2Yb$ tetrahedra become $1Ti3Yb$ tetrahedra (purple) and the two $4Ti$ tetrahedra change to $3Ti1Yb$. No other ytterbium titanates have been documented that could be used as a guide to the structural changes that will result, but we note that Ti-O bond lengths are much shorter than Yb-O bond lengths ($\sim$1.95 Å vs. $\sim$2.3 Å) and Ti-O-Ti bond angles tend to be approximately 130°. Thus, oxygen atoms in the $1Ti3Yb$ tetrahedra will be displaced away from the stuffed atom towards the Ti atoms at the outer vertices of the orange tetrahedra in Fig. 3.19(d). Nevertheless, these changes still do not satisfy the normal oxygen bonding configurations with Ti^{4+} or Yb^{3+}. It therefore seems likely – and is indeed indicated by our EELS

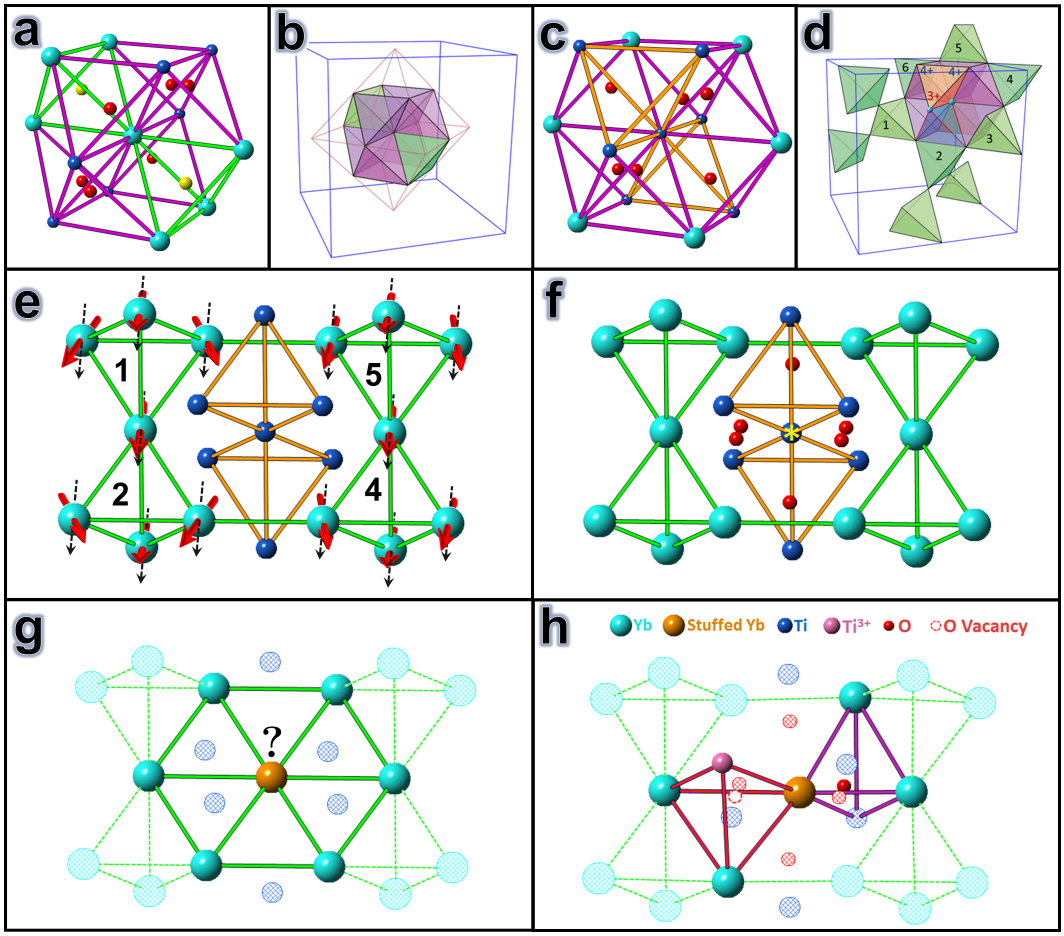

Figure 3.19: Cation tetrahedra in $Yb_2Ti_2O_7$. (a) Ball and stick model showing the eight cation tetrahedra that have a common vertex at an Yb atom. (b) The same tetrahedra, colour-coded as $2Ti2Yb$ (purple) and $4Yb$ (green). (c) Ball and stick model showing the eight cation tetrahedra that have a common vertex at a Ti atom. (d) The effect of stuffing an Yb^{3+} atom onto the Ti^{4+} site. The six $2Ti2Yb$ tetrahedra (purple) become $1Ti3Yb$ and the two $4Ti$ (orange) become $3Ti1Yb$. Stuffing produces an oxygen vacancy in one of the surrounding $1Ti3Yb$ tetrahedra (highlighted in red) and the conversion of an adjacent Ti atom from 4+ to 3+. The network of magnetic $4Yb$ tetrahedra are also shown, with six numbered $4Yb$ tetrahedra surrounding the stuffed atom site. (e) The Yb tetrahedra shown in (d) without any stuffing and possible all-in-all-out [47] (the left Yb tetrahedra) and two-in-two-out [47] (the right Yb tetrahedra) splayed ferromagnetic configurations (black arrows are along [1 0 0]). (f) Position of the oxygen atoms in the vicinity of the Ti atom (marked by a yellow star) before stuffing. (g) Frustrated triangular lattice of magnetic cations formed by replacing a Ti atom with Yb. (h) Formation an oxygen vacancy and reduction of a Ti^{4+} cation to Ti^{3+} as a consequence of stuffing.

results – that replacement of Ti^{4+} by Yb^{3+} will result in one of the adjacent Ti atoms reducing to Ti^{3+} with an accompanying vacancy in that $1Ti3Yb$ tetrahedron (highlighted red in Figs. 3.19(d) and (h)). Still further changes in structure are

possible such as static distortions of the cation framework, with the tetrahedron containing the oxygen vacancy expanding due to Coulomb repulsion. There are likely to be significant effects on the magnetic $4Yb$ tetrahedra that surround the stuffed atom; there are six nearby $4Yb$ tetrahedra, numbered in Fig. 3.19(d). We note that a study of oxygen deficient $Y_2Ti_2O_7$ [37] found that $4Y$ tetrahedra were much more likely to lose their oxygen atom and it is thus possible that the oxygen vacancy in the red tetrahedron moves into the adjacent $4Yb$ tetrahedron #2. In any case, tetrahedron #2 is most affected. It is clear from Figs. 3.19(e) and (g) that the replacement of a nonmagnetic Ti^{4+} cation by a magnetic Yb^{3+} can modify the nature of the magnetic exchange with the system through formation of the frustrated triangular lattice of magnetic cations. Furthermore, the introduction of a magnetic moment on the Ti site as a consequence of reduction of Ti^{4+} to magnetic Ti^{3+} as well as stuffing the Yb atom onto the Ti site will disrupt the magnetic order locally and may serve as pinning sites for magnetic defects (e.g. monopoles in spin ice) within the material [37].

The differences between the three samples examined here can be interpreted in terms of such structural rearrangements. As shown in Fig. 3.20, the [2 1 1] atom columns can be also pictured as chains of tetrahedra. For both the Yb and Ti atom columns the chain consists only of $2Ti2Yb$ tetrahedra, whereas $M1$ is made of alternating pairs of $2Ti2Yb$ and $4Yb$ tetrahedra and $M2$ is made of alternating pairs of $2Ti2Yb$ and $4Ti$ tetrahedra. There are 10 cations in the repeat motif in all cases, and each atom column type has a different Yb:Ti ratio in its tetrahedral chain.

In a stuffed material, the oxygen atom inside a tetrahedron will be affected by all four atoms at its vertices, which means that the oxygen atoms close to any given [2 1 1] atom column depend upon the chains of tetrahedra shown in Fig. 3.20, not just the atoms in the column. The oxygen atoms are therefore very sensitive to stuffing. Furthermore, the difference in Yb:Ti ratio for each chain means that each has a different sensitivity. Thus, using the same binomial statistics (Eq. 3.1) for a 45 nm thick TEM specimen, and e.g. 1% stuffing and no anti-stuffing, we find that only 30% of M columns and 50% of Ti columns are directly affected by stuffing (obviously, no Yb columns are affected). However, the nearby oxygen atoms are affected in around 67% of $M1$ columns, 77% of Ti columns, 89% of Yb columns and 92% of $M2$ columns. That is, the radial profiles of Yb and $M2$ columns should be more affected by stuffing than the Ti and $M1$ columns and this does indeed appear to be the case in Fig. 3.8. Furthermore, the structural rearrangements illustrated in Fig. 3.19 will tend to move oxygen atoms away from $M1$ columns more readily

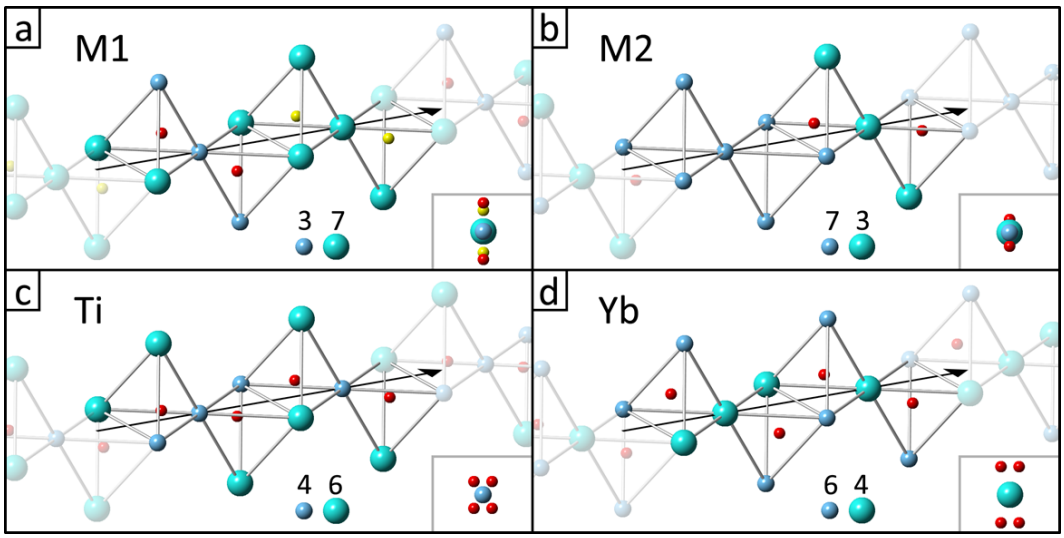

Figure 3.20: The four types of [2 1 1] atom columns in $Yb_2Ti_2O_7$, shown as a chain of cation tetrahedra. The black arrow indicates the direction of propagation of the electron beam. Partial transparency highlights the repeat motif of 10 cations; the number of Ti (dark blue) and Yb (light blue) atoms in the motif is given at the bottom of each panel. The [2 1 1] projection of each column is inset bottom right. Colour scheme is the same as Fig. 2.1.

than $M2$ columns, producing the changes in radial profile shown in Fig. 3.8.

Taken together, the modifications to the delicate balance of magnetic interactions, which result from the stuffing and changes in Ti valence that we have observed, will lead to a breakdown in the onset of long-range ferromagnetic order. These results are consistent with the magnetic properties of sample 3 (Fig. 2.2(a)) showing no clear transition in the specific heat down to 50 mK.

3.7 Summary

I have examined three samples of $Yb_2Ti_2O_7$, with different low-temperature specific heat capacity anomalies that indicate varying magnetic properties, using ac-STEM. I found direct evidence for stuffing of Yb onto Ti sites, using atomic resolution EDX of Ti atom columns that have anomalously bright contrast, in sample 3. I also observed Yb atom columns that have anomalously dark contrast, but were unable to use the well-known compositional sensitivity of ADF-STEM to extract the statistics of stuffing (or anti-stuffing) due to the confounding effects specimen thickness variations and/or surface damage. Nevertheless, we clearly observe the influence of oxygen atoms on these images, and by examining the radial intensity profile of cation columns we observe rather different behaviour of oxygen atoms near

to the cation columns for the three samples. The sensitivity of the different types of atom column in the [2 1 1] ADF-STEM images is explained by considering them as chains of tetrahedra with different Ti:Yb ratios. The changes are consistent with the rearrangement of oxygen atoms away from Yb that occupies Ti sites. Using Ti-$L_{3,2}$ ELNES, we find that these differences in ADF-STEM radial intensity profile are accompanied by changes in Ti valence number, indicating the presence of magnetic Ti^{3+} and oxygen vacancies. Samples that have more diffuse specific heat capacity anomalies have more stuffing, lower Ti valence numbers and more disordered oxygen sub-lattices.

I showed that variation in the low-temperature magnetic properties of $Yb_2Ti_2O_7$ is due to the flexibility in the structure of this material. In the next chapter I will show how the structure of ytterbium titanate tolerate a deviation from the nominal stoichiometry.

Chapter 4

Defects in non-stoichiometric ytterbium titanates

4.1 Introduction

Both theoretical [16] and experimental (by X-ray diffraction and neutron scattering) [38, 58] studies of the structure of non-stoichiometric pyrochlores have found that an excess of A cations produces oxygen vacancies as well as substitution of B cations by A cations while an excess of B cations causes the formation of A vacancies. Thus, the general formula of non-stoichiometric pyrochlore oxides for A or B excess may be written as $A_2(B_{2-2x}, A_{2x})O_{7-x}$ or $A_{2-2x}B_2O_7$, where x is the fractional excess of the cations, respectively. Here this proposal is examined by characterization of the atomic structure of two non-stoichiometric ytterbium titanate samples, one with 2.5% Yb excess and another with 2.5% Ti excess, using ac-STEM. The terms $Yb_{2.05}Ti_2O_{7+\xi}$ and $Yb_{1.95}Ti_2O_{7-\xi}$, where $0 \leq \xi \leq 0.075$ are used for the former and latter in this work, respectively.

4.2 $Yb_{1.95}Ti_2O_{7-\xi}$

Fig. 4.1 shows TEM images acquired from two different particles ($P1$ and $P2$) of $Yb_{1.95}Ti_2O_{7-\xi}$ sample before and after electron irradiation. The defect clusters shown in Fig. 4.1(b-d) are induced by 200 keV electron irradiation with a current density of $\sim$500 pAcm^{-2} at room temperature inside the microscope immaculately after beam concentration on the sample. Such defects were not formed by electron irradiation in either $Yb_{2.05}Ti_2O_{7+\xi}$ powder or $Yb_2Ti_2O_7$ single crystals.

As seen in ADF- and BF-STEM images of the induced defect clusters (Fig. 4.2),

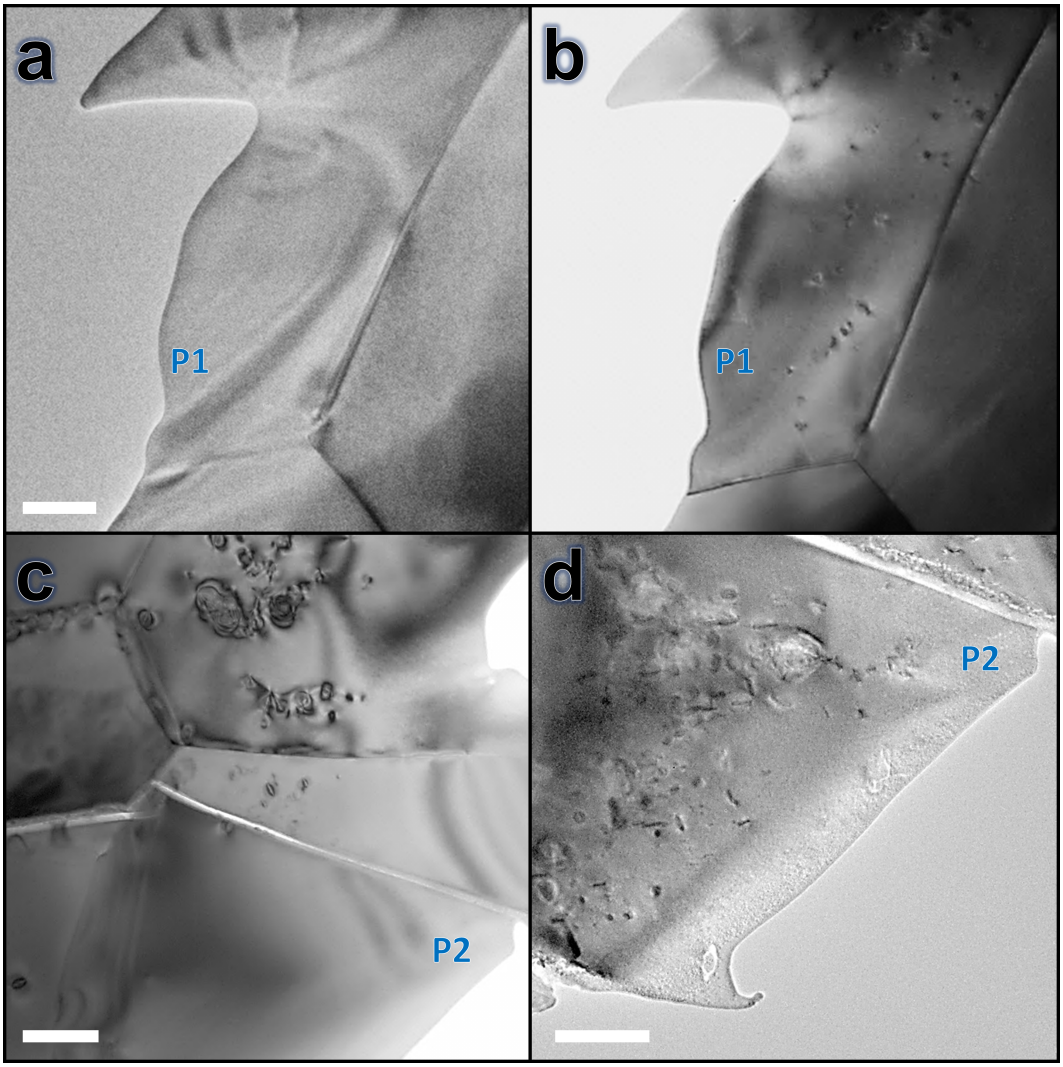

Figure 4.1: TEM images acquired from two particles ($P1$ and $P2$) of $Yb_{1.95}Ti_2O_{7-\xi}$ before, (a) and (c), as well as after, (b) and (d), electron irradiation with 200 keV electrons (scale bars are 200 nm).

although almost all the irradiation-induced defects in the $Yb_{1.95}Ti_2O_{7-\xi}$ sample have {1 1 1} habit planes – except from very few cases with {1 1 0} habit planes –, they are not all of the same type; a few have strain fields while the majority induce no (measurable) strain to the crystal. The defects appear as thin dark lines along $< 1\ 1\ 1 >$ directions in ADF-STEM images, typically several tens of nm in length. A slightly bright surrounding region, several tens of nm in size, is also visible in the lower magnification ADF-STEM image (see inset in Fig. 4.2(a)).

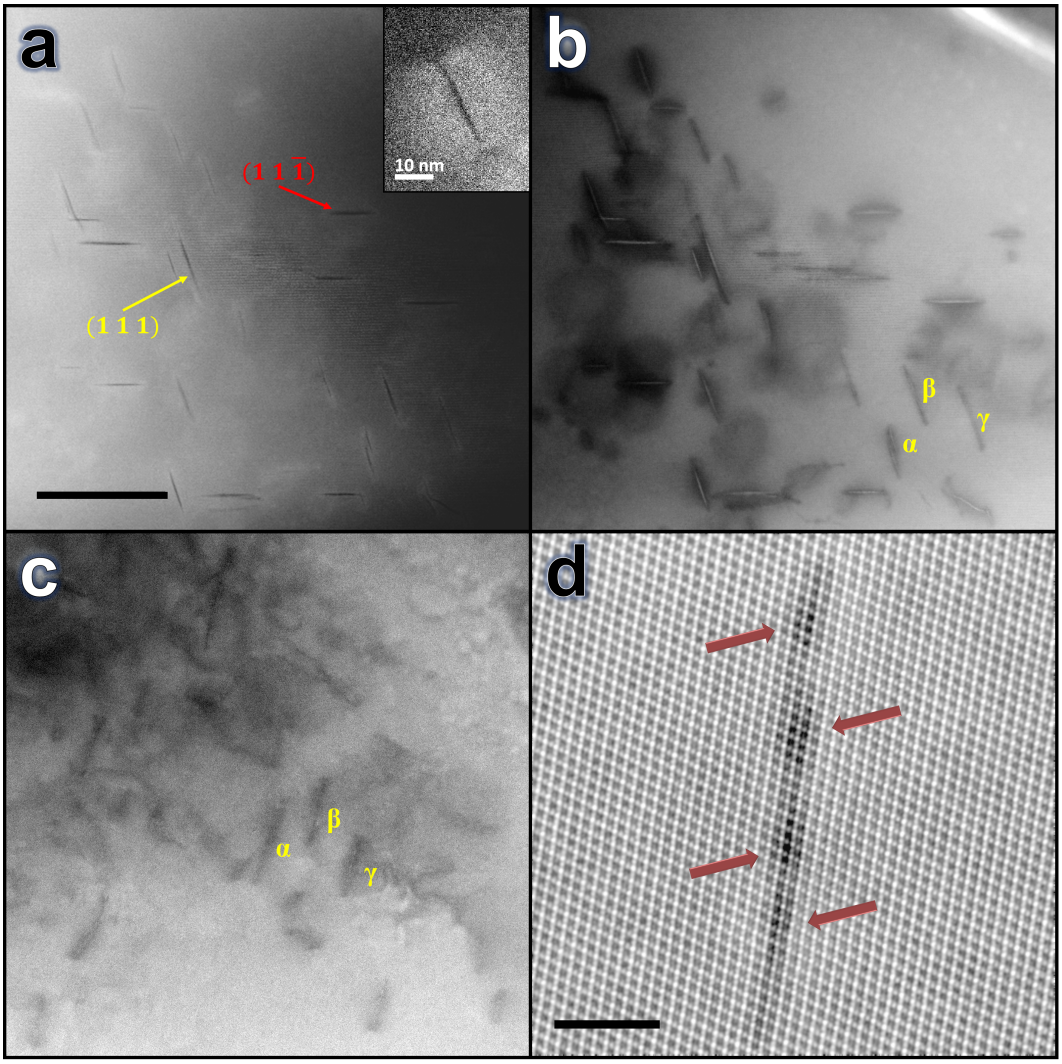

Figure 4.2: (a) ADF-, (b) BF-STEM images, viewed along [$\bar{1}$ 1 0], and (c) BF-STEM image, viewed along [$\bar{3}$ 2 1], of the planar defects in $Yb_{1.95}Ti_2O_{7-\xi}$ irradiated with 200 keV electrons (scale bar is 100 nm). (d) One of the defects in {1 1 1} planes at high magnification (scale bar is 5 nm).

4.2.1 Defects with no measurable strain

I observed that most of the defects with {1 1 1} habit planes (see also Fig. 4.3) are formed by a few tiny areas with dark contrast in ADF-STEM images as shown by the arrows in Fig. 4.2(d). These areas have sphere/disc shapes since they appears as lines in [$\bar{3}$ 2 1] (Fig. 4.2(c)) direction. Since contrast in ADF images is primarily proportional to mass-thickness, this indicates material that is either of much lower density, or is thinner, than the matrix. A faint "halo" of brighter material is visible around the defects, which may indicate denser material or changes in the secondary

contrast mechanism of electron channelling (static atomic displacements have been shown to result in increased ADF signal, e.g. [149]). However, no strain can be measured either along these defects or at their ends. These sphere/disc shaped areas could be vacancy clusters formed by an accumulation of migrant vacancies since the energy for vacancy (cation) diffusion drops during electron irradiation. This reduction in the diffusion energy results from a local increase in the temperature of the sample, since the heat generated by the electron irradiation is not easily conducted away, due to the poor thermal conductivity of the material which is $\sim$3 $WK^{-1}m^{-1}$ at room temperature [150] (thermal conductivity of copper at room temperature is 401 $WK^{-1}m^{-1}$ [151]). In some cases, the adjacent clusters grow and then form a disc shaped defect with a diameter of $\sim$50 nm. It can be confirmed that these defects have a disc shape with $< 1\ 1\ 1 >$ normal vectors since they appear as lines in both the $[\bar{1}\ 1\ 0]$ (Fig. 4.2(b)) and $[\bar{3}\ 2\ 1]$ (Fig. 4.2(c)) directions.

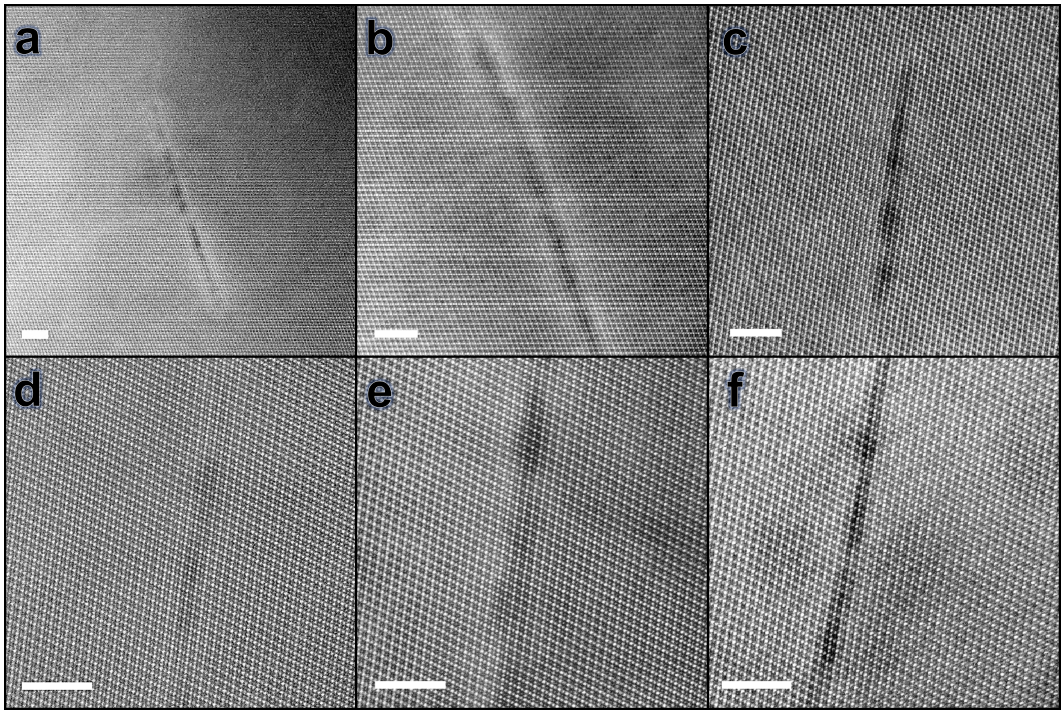

Figure 4.3: (a) ADF-STEM images, viewed along $[\bar{1}\ 1\ 0]$, of several planar defects exhibiting no measurable strain in $Yb_{1.95}Ti_2O_{7-\xi}$ irradiated with 200 keV electrons (scale bars are 5 nm).

Fig. 4.4(a) shows an ADF image, taken with an ADF detector inner angle of 4.6α, from one of the defects with $\{1\ 1\ 0\}$ habit planes. This defect is about eight $\{0\ 1\ 1\}$ atomic planes (planes between yellow dashed lines in Fig. 4.4(a)) thick, which is $\sim$1.5 nm. In Fig. 4.4(b), histograms of the mean integrated intensities from

Voronoi cells centred on each atom column in Fig. 4.4(a), reveal that all of the Ti, Yb and M atom columns outside the defect area are 6 to 7% more intense than the columns with the same nominal cation compositions (Ti*, Yb* and M^*) in the defect. Similarly, as shown in Fig. 4.5, all of the atom columns inside the defect area are less intense than the columns with the same nominal cation compositions outside the defect with {1 1 1} habit planes. That means there are a number of vacancies at both the Ti and Yb sites inside these defects.

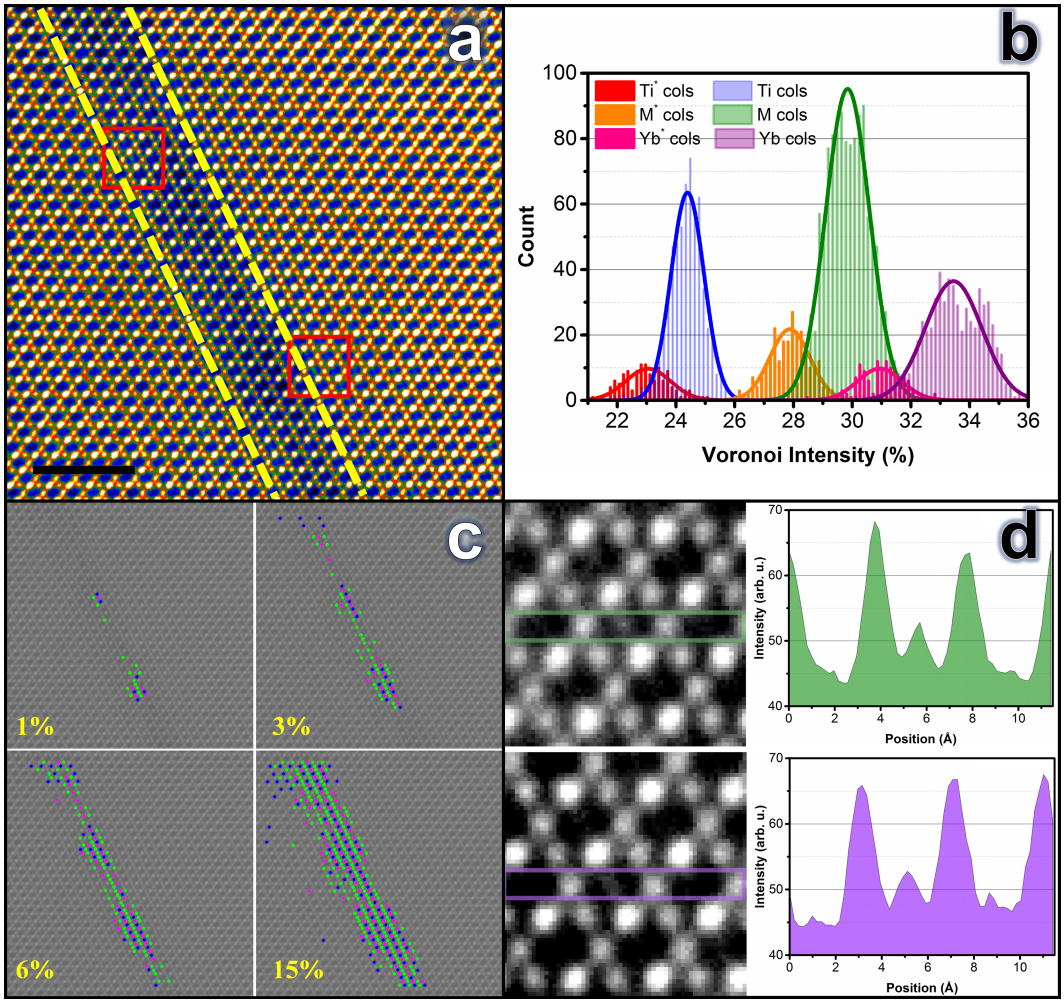

Figure 4.4: (a) ADF-STEM image taken with an ADF detector inner angle of ~4.6α from the defects with {0 1 1} habit planes viewed along [4 1 1] (scale bar is 2 nm), (b) histogram of the extracted mean integrated intensities from the ADF image shown in (a), using Voronoi cells centred on each atom column, (c) columns with intensities of the bottom 1, 3, 6 and 15 percent for each atom column are shown with solid circles, Ti in blue, Yb in pink and M in green and (d) anomalously bright Ti columns present in the areas marked by red squares in (a).

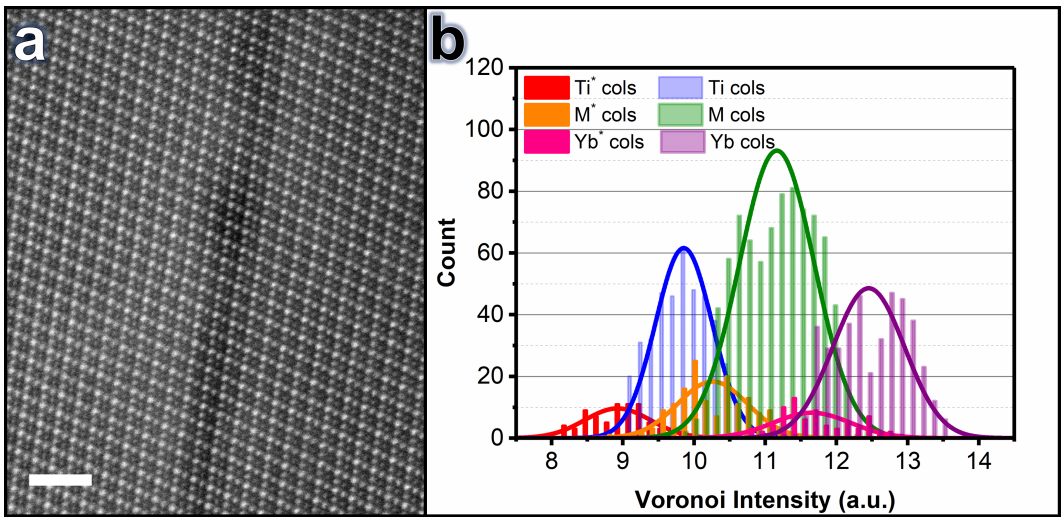

Figure 4.5: (a) ADF-STEM image taken with an ADF detector inner angle of $\sim$4.6α from the defects with {1 1 1} habit planes viewed along [$\bar{1}$ 1 0] (scale bar is 2 nm), (b) histogram of the extracted mean integrated intensities from the ADF image shown in (a), using Voronoi cells centred on each atom column.

In addition, there is a systematic variation in the intensity of the atom columns in the defect area shown in Fig. 4.4(a). For instance, the position of the columns with intensities of the bottom 1, 3, 6 and 15 percent for each atom column, shown in Fig. 4.4(c), reveal the fact that the defect originates from a couple of adjacent vacancy clusters and then they grow and joined together. Furthermore, EDX data presented in Fig. 4.6 show that both Ti and Yb signals have lower intensities in the defect area. In fact, since the relative intensities of the Yb and Ti atom columns are unchanged in both the ADF and EDX data, there has not been a transition to a disordered "defect fluorite" structure. This indicates that the defect is simply thinner material, i.e. a void, or a trench on the specimen surface. Interestingly, the material surrounding the defect shows clear evidence of site swapping between the cation sub-lattices as shown in Fig. 4.4(d). Occasional Ti sites have significantly brighter contrast than their neighbors, indicating the "stuffing" of Yb on Ti sites. However, the opposite type of site swapping, i.e. Ti on Yb site, is not observed. This does not preclude the existence of "anti-stuffing", because the fractional change in ADF contrast of a faint Ti column due to the addition of a heavy Yb atom is much larger than that for an intense Yb column due to the addition of a light Ti atom. The presence of Yb atoms on the Ti sites is consistent with the inward diffusion of vacancies to the defect area and consequently outward diffusion of the cations such as Yb from the area. Stanek et al. [16] found that a BO_2 excess in $A_2B_2O_7$ pyrochlores is expected to produce A^{3+} vacancies since they have lower energy than

interstitial B. Hence, the source of the migrated vacancies in the $Yb_{1.95}Ti_2O_{7-\xi}$ sample are Yb vacancies.

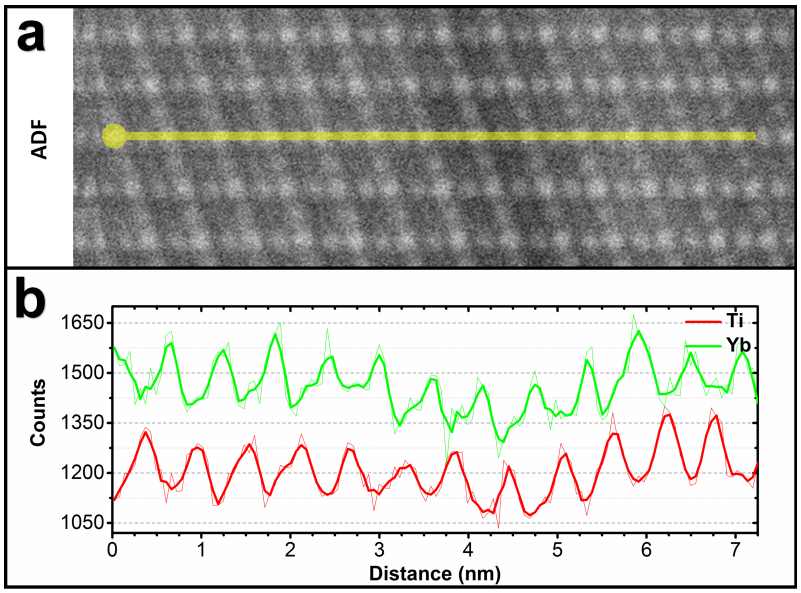

Figure 4.6: (a) ADF-STEM image taken from a defect with (1 1 1) habit plane. (b) The EDX line scan across the defect shown in (a).

4.2.2 Defects with measurable strain fields

In addition to the faults mentioned above that exhibit no measurable strain field, I observed some defects, as shown in Figs. 4.7 and 4.8(a), which induce antiphase boundaries in the {1 1 1} Kagome planes. Although the pyrochlore crystal structure is FCC cubic, the $1/2 < 1\ 1\ 0 >$ dislocations that would be expected in this lattice have large Burgers vectors; Mergen [152] was able to show that dislocations probably have Burgers vectors along $< 1\ 1\ 0 >$ but did not provide a definitive analysis, or investigate the dissociation into partials obvious in their TEM images. Hence, a detailed analysis is provided here to investigate dislocations in the pyrochlore structure.

Fourier filtered images for Fig. 4.8(a) obtained by choosing the 2 2 2 and $\overline{2}\ \overline{2}\ 2$ spots are shown in Figs. 4.8(c) and (d), respectively. The filtered images reveal that these defects are created by the insertion of extra ($\overline{2}\ \overline{2}\ 2$) and (2 2 2) half-planes. The strain distribution as obtained from GPA around the defects is shown in Figs. 4.8(d-f). Here, ε_{xx} and ε_{yy} contain only $[\overline{1}\ \overline{1}\ 2]$ and [1 1 1] components of the strain fields, respectively, and ε_{xy} shows the shear strain relative to these axes.

As shown in Figs. 4.8(d-f), there are convergence regions of strain ($\delta 1$, $\delta 2$, $\delta 3$ and

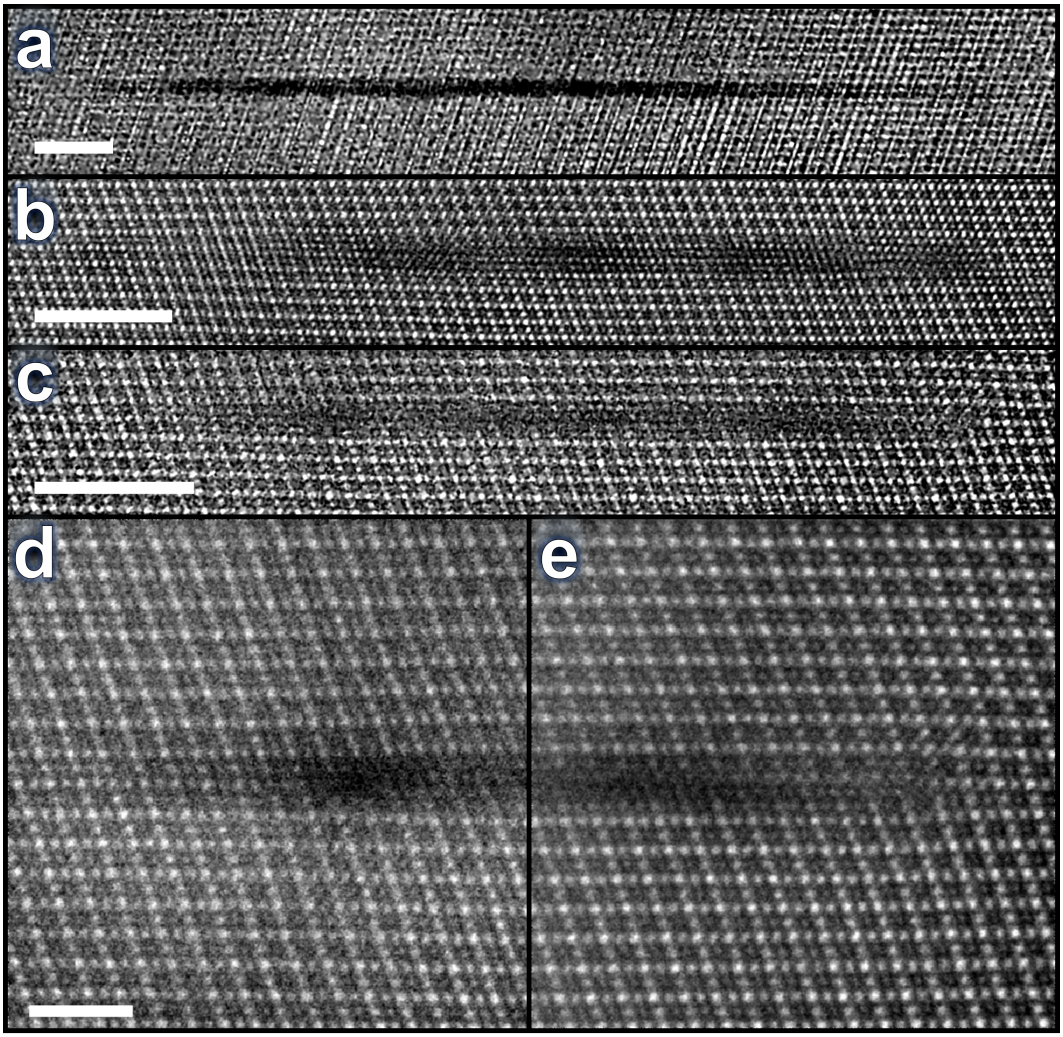

Figure 4.7: (a) (a), (b) and (c) ADF-STEM images, viewed along [$\overline{1}$ 1 0], of defects inducing antiphase boundary in the {1 1 1} planes (scale bars are 5 nm). ADF-STEM images obtained from the left and right ends of the defect displayed in (c) are presented in (d) and (e), respectively; scale bar in (d) is 2 nm.

$\delta 4$) at the positions where extra half-planes have been introduced. Although $\delta 1$ and $\delta 2$ cannot be clearly resolved at this magnification, as it is shown at a higher magnification (Fig. 4.9), they are separated from one other. Fig. 4.9(a) shows an ADF-STEM image obtained from the right core of the defect displayed in Fig. 4.8(a) at a higher magnification. It is clearly seen in the strain distributions around the right core of the defect, presented in Figs. 4.9(b-e), that $\delta 1$ and $\delta 2$ are separated from one other. Thus, each end of this defect is made of two dislocations. $\delta 2$ and $\delta 3$ are invisible in the strain field containing only [1 1 1] components (Figs. 4.8(f) and 4.9(d)) while $\delta 1$ and $\delta 4$ are invisible in the strain field containing only [1 1 $\overline{1}$]

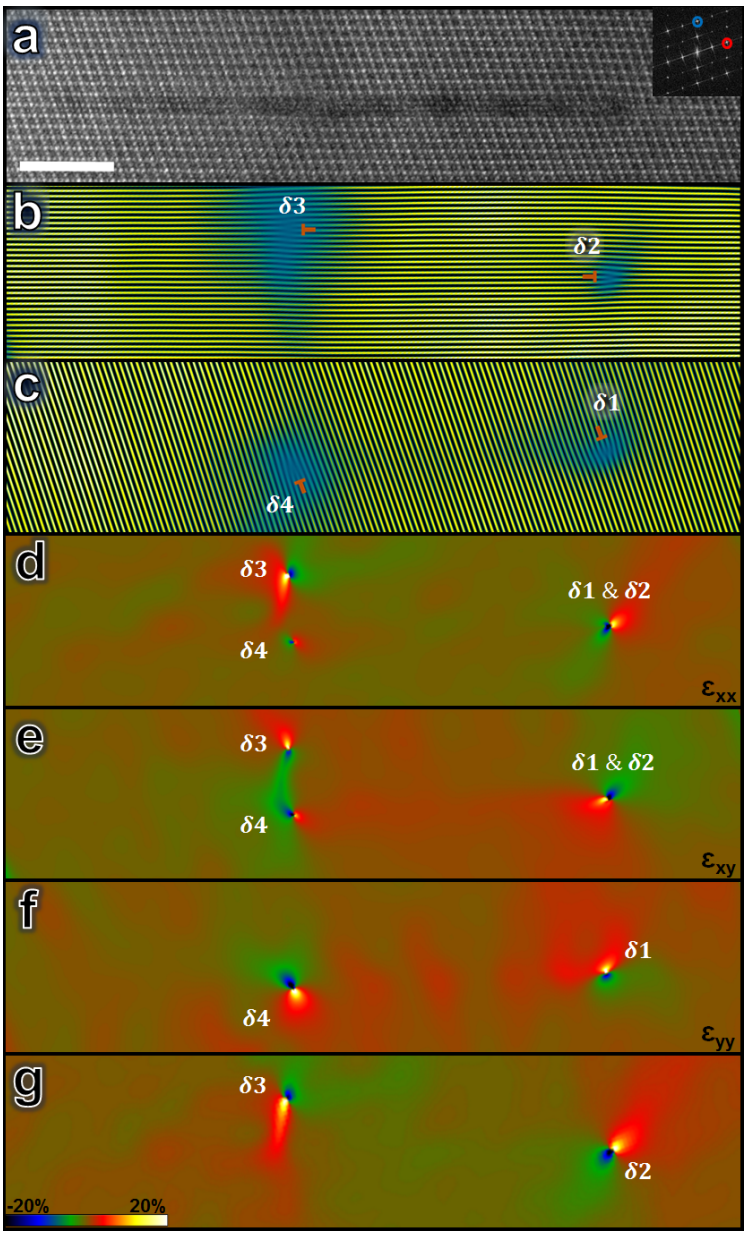

Figure 4.8: (a) ADF-STEM image from a defect inducing antiphase boundary in the {1 1 1} planes viewed along [1 $\overline{1}$ 0] (scale bar is 5 nm). Inset shows a Fourier transform of the image with the spots, (2 2 2) marked with a blue circle and ($\overline{2}$ $\overline{2}$ 2) marked with a red circle, used for GPA. (b) and (c) The Fourier filtered images for (a) obtained by choosing the (2 2 2) and ($\overline{2}$ $\overline{2}$ 2) spots, respectively. Strain distribution (d) ε_{xx} (e) ε_{xy} and (f) ε_{yy} around the defect; where ε_{xx} and ε_{yy} contain only [$\overline{1}$ $\overline{1}$ 2] and [1 1 1] component strain fields, respectively, and ε_{xy} contains both strain components. (g) Strain distribution containing only [1 1 $\overline{1}$] component.

components (see Figs. 4.8(g) and 4.9(e)). Therefore, the Burgers vectors of $\delta 1$ and $\delta 4$ are perpendicular to [1 1 $\overline{1}$] and those of $\delta 2$ and $\delta 3$ are perpendicular to [1 1 1].

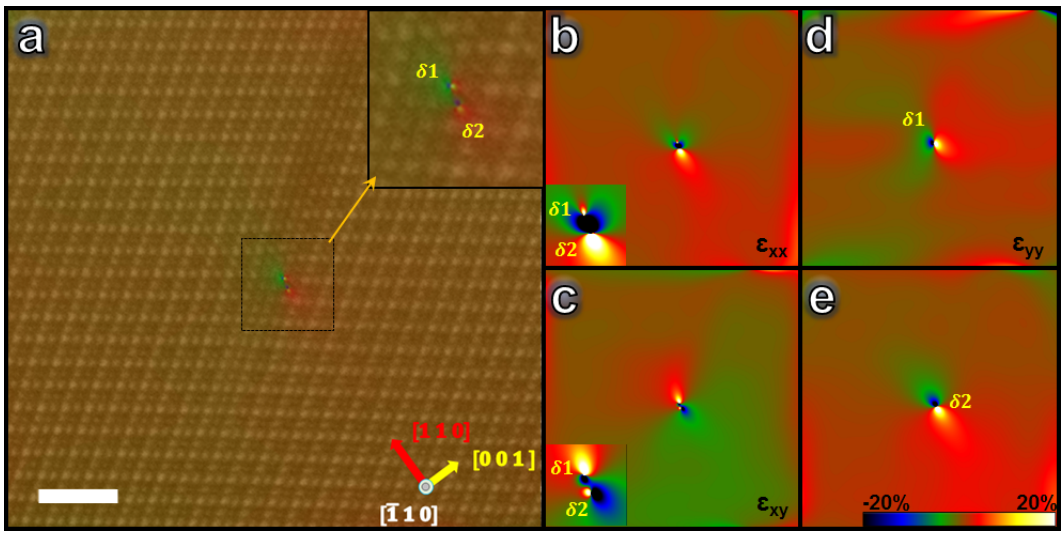

Figure 4.9: (a) An ADF-STEM image (scale bar is 2 nm) obtained from the right core of the defect displayed in Fig. 4.8(a). The strain distributions ε_{xx}, ε_{xy} and ε_{yy} in the ADF image are presented in (b), (c) and (d), respectively. (e) Strain distribution containing only $[1\ 1\ \bar{1}]$ components in the ADF image.

I am using GPA data to calculate the Burgers vector of the defect. The x- and y-components of the dislocation density tensor (a_x and a_y) calculated from the distortion fields obtained by applying GPA on Fig. 4.9(a) are presented in Figs. 4.10(a) and (b). As shown in the dislocation density tensor maps, the distance between the two dislocations, $\delta 1$ and $\delta 2$, is ~1.92 Å along the $[\bar{1}\ \bar{1}\ 0]$ direction in the ADF image. Surface integrals (i.e. b according to Eq. (2.10)) of the dislocation density tensor around the position of $\delta 1$ and $\delta 2$ calculated over several different area sizes are plotted in Figs. 4.10(c) and (d).

According to the surface integral plots, the projection of Burgers vector for the defect's right core is $1/4[\bar{1}\ \bar{1}\ 0]$. Given that $\delta 1$ and $\delta 2$ are perpendicular to $[1\ 1\ \bar{1}]$ and $[1\ 1\ 1]$ respectively, and the projection of their vector sum is $1/4[\bar{1}\ \bar{1}\ 0]$, $\delta 1$ and $\delta 2$ are equal to $1/8[\bar{1}\ \bar{1}\ \bar{2}]+c_1[1\ \bar{1}\ 0]$ and $1/8[\bar{1}\ \bar{1}\ 2]+c_2[1\ \bar{1}\ 0]$, respectively; where c_1 and c_2 are constants. In addition, the surface integral plots for the dislocation density tensor over small areas centred at the position of both $\delta 1$ and $\delta 2$ (Figs. 4.10(c) and (d)) also confirm that their projections are $1/8[\bar{1}\ \bar{1}\ \bar{2}]$ and $1/8[\bar{1}\ \bar{1}\ 2]$, respectively. It is worth mentioning that the same results have been calculated for other similar defects, see the resulting data displayed in Fig. 4.11.

The projection of the calculated Burgers vectors of the dislocations in Fig. 4.9(a) is displayed schematically in Fig. 4.12(a). Describing the dislocations and their effect in the FCC structure can be performed with the assistance of a Thompson

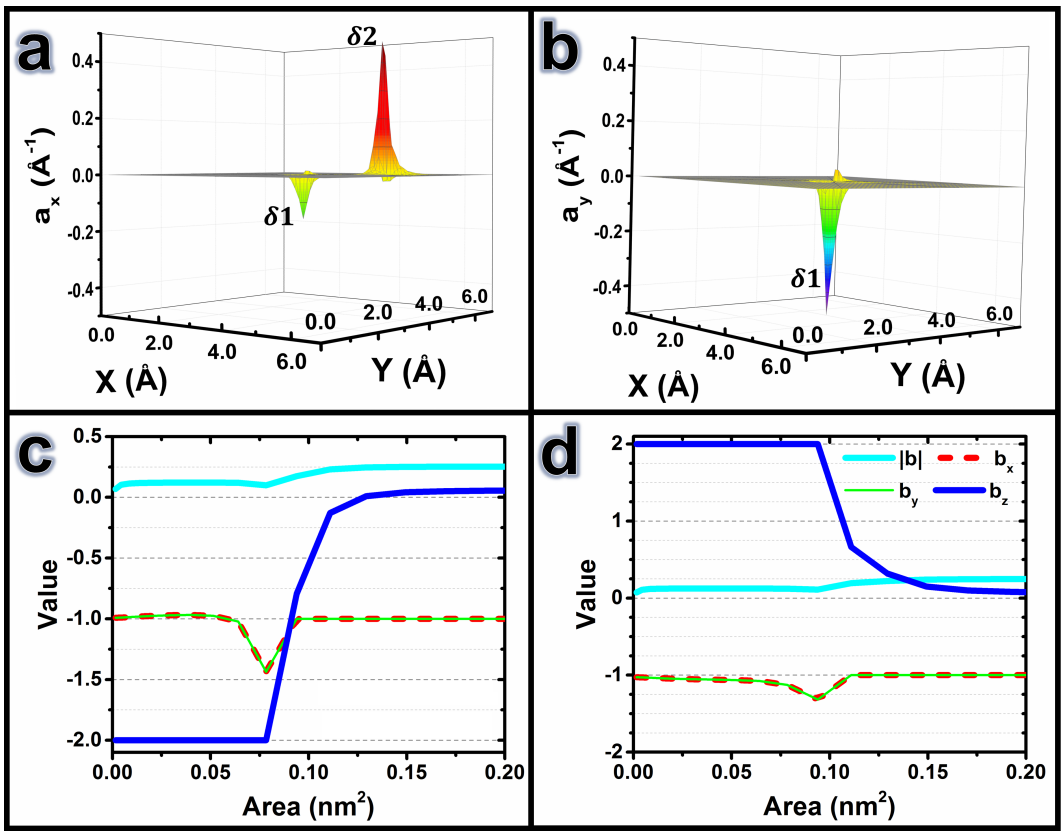

Figure 4.10: (a) x- and (b) y- components of the dislocation density tensor (a_x and a_y) calculated from distortion fields around the defect core shown in Fig. 4.9(a). The surface integral plots of the dislocation density tensor around (c) $\delta 1$ and (d) $\delta 2$ over different area sizes; here $\overrightarrow{b} = |b|[b_x\ b_y\ b_z]$.

tetrahedron and a double Thompson tetrahedron [153–155]. Here I use a tetrahedron and introduce an octahedron as a simple alternative for the double tetrahedron to describe the dislocations (Fig. 4.12(b-e)).

According to the tetrahedron displayed Figs. 4.12(c) and (e), the possible vectors for $\delta 1$, $\delta 2$ and their sum (defect vector) are $\overrightarrow{AG}$, $\overrightarrow{GD}$ and $\overrightarrow{AD}$ (or $\overrightarrow{AE}$, $\overrightarrow{ED}$ and $\overrightarrow{AD}$), respectively. But, such a configuration for the dislocations is not energetically favourable since the defect energy ($b^2 = a^2/8$) is half of the total energy of $\delta 1$ and $\delta 2$ ($b_{\delta 1}^2 + b_{\delta 2}^2 = a^2/8 + a^2/8 = a^2/4$) in this case. However, by considering the atoms position in an octahedron, $\delta 1$, $\delta 2$ and their vector sums can, apart from the possible vectors mentioned above, be $\overrightarrow{AE}$, $\overrightarrow{EF}$ and $\overrightarrow{AF}$ (or $\overrightarrow{BE}$, $\overrightarrow{ED}$ and $\overrightarrow{BD}$), respectively. This means that the defect with a Burgers vector of the type $1/2 < 1\ 0\ 0 >$, has been dissociated into two dislocations of the type $1/4 < 1\ 1\ 0 >$. It is worth mentioning that the defect energy will not change when this dislocation dissociation occurs

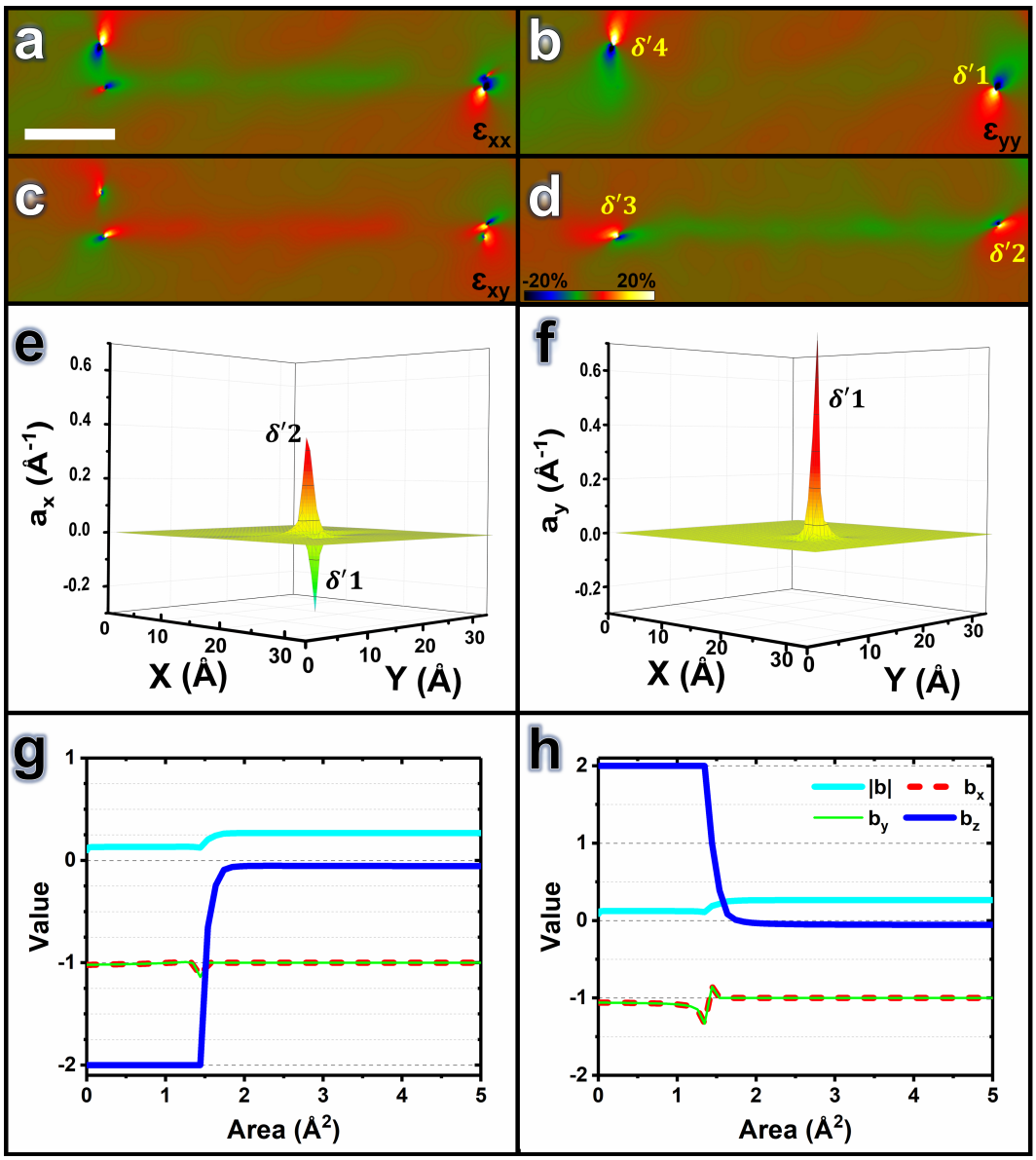

Figure 4.11: The strain distributions (a) ε_{xx}, (b) ε_{xy} and (c) ε_{yy} in the ADF image shown in Fig. 4.7.(e) $[\bar{1}\ \bar{1}\ \bar{1}]$ and (f) $[\bar{1}\ \bar{1}\ 1]$ components of the dislocation density tensor (a_x and a_y) calculated from distortion fields around the defect core shown in Fig. 4.7(e). (d) Strain distribution containing only $[1\ 1\ \bar{1}]$ components in the ADF image. The surface integral plots of the dislocation density tensor around (g) $\delta'1$ and (h) $\delta'2$ over different area sizes; here $\overrightarrow{b} = |b|[b_x\ b_y\ b_z]$.

$(b^2 = b_{\delta1}^2 + b_{\delta2}^2 = a^2/4)$. Thus, the actual Burgers vectors for $\delta1$, $\delta2$ and their sum are $1/4[0\ \bar{1}\ \bar{1}]$, $1/4[0\ \bar{1}\ 1]$ and $1/2[0\ \bar{1}\ 0]$ (or $1/4[\bar{1}\ 0\ \bar{1}]$, $1/4[\bar{1}\ 0\ 1]$ and $1/2[\bar{1}\ 0\ 0]$), respectively.

Accordingly, the defect is an extrinsic dislocation loop having both Frank and

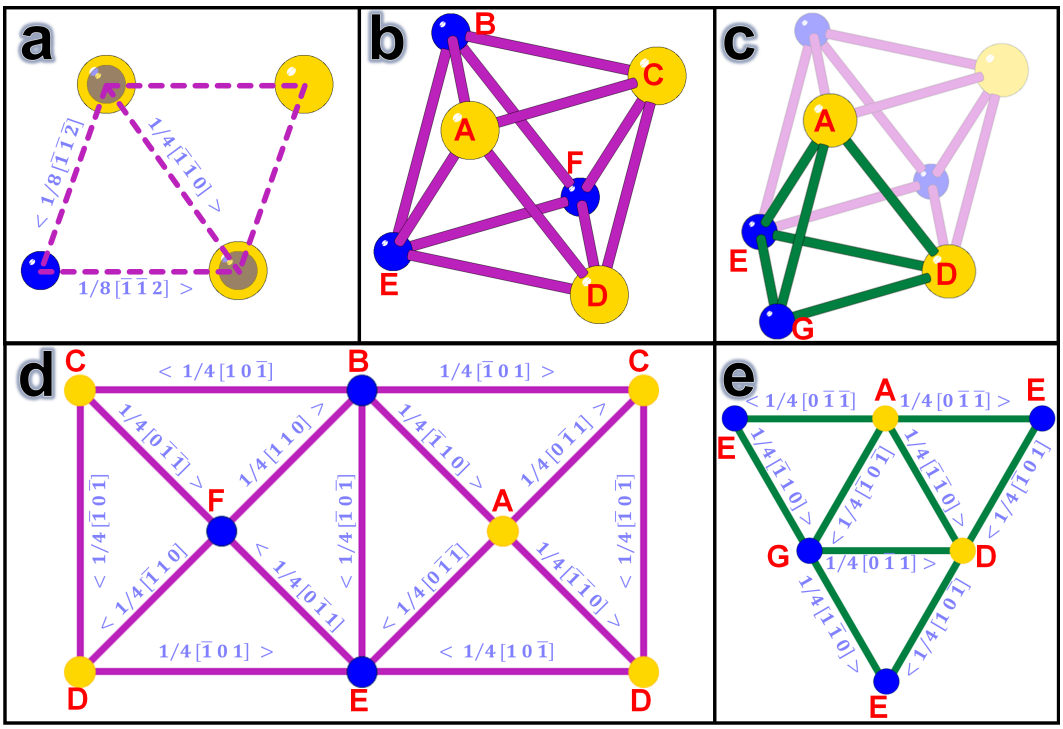

Figure 4.12: (a) Projections of the Burgers vectors for $\delta 1$ ($1/8[\bar{1}\ \bar{1}\ \bar{2}]$), $\delta 2$ ($1/8[\bar{1}\ \bar{1}\ 2]$) and their sum ($1/4[\bar{1}\ \bar{1}\ 0]$) viewed along $[1\ \bar{1}\ 0]$ in the $Yb_2Ti_2O_7$ crystal; the Yb and Ti atoms are shown in yellow and blue, respectively. (b) An octahedron in the $Yb_2Ti_2O_7$ structure formed by three Yb and three Ti atoms. (c) A tetrahedron in the $Yb_2Ti_2O_7$ structure. (d) and (e) Two-dimensional representations of the octahedron shown in (b) and tetrahedron shown in (c), respectively.

Shockley characteristics. As shown in Fig. 4.13(a), the stacking sequence $ABCABC$ of the $\{1\ 1\ 1\}$ planes is $ABC\boldsymbol{B}ABC$ in the defect region as a consequence of introduction of an extra $(\bar{2}\ \bar{2}\ 2)$ half-plane (marked with a bold orange B in the figure). On the other hand, an antiphase boundary has been induced in the $\{1\ 1\ 1\}$ planes as a consequence of gliding along $[\bar{1}\ \bar{1}\ \bar{2}]$. According to the atomic resolution EDX elemental maps data shown in Fig. 4.14, the extra $(\bar{2}\ \bar{2}\ 2)$ half-plane contains both Yb and Ti atoms. Furthermore, both the Yb and Ti Kagome $\{1\ 1\ 1\}$ planes (Figs. 4.14(c) and (d)) preserved their structure in the defect area until they meet the extra $(\bar{2}\ \bar{2}\ 2)$ half-plane where the antiphase boundary induced. That means the pyrochlore to defect fluorite transformation did not occur in the defect area.

In summary, EDX results presented in section 4.2.1 (Fig. 4.6) indicate a fraction of both the Ti and Yb atoms migrated from the defect area as a result of electron irradiation. It seems, electron irradiation, first produces platelets of vacancies (Fig. 4.2(d) and Fig. 4.4(a)) and then, in some cases, leads to further changes through precipitation of close-packed $\{1\ 1\ 1\}$ platelets of interstitial atoms (Fig. 4.8(a)). Electron

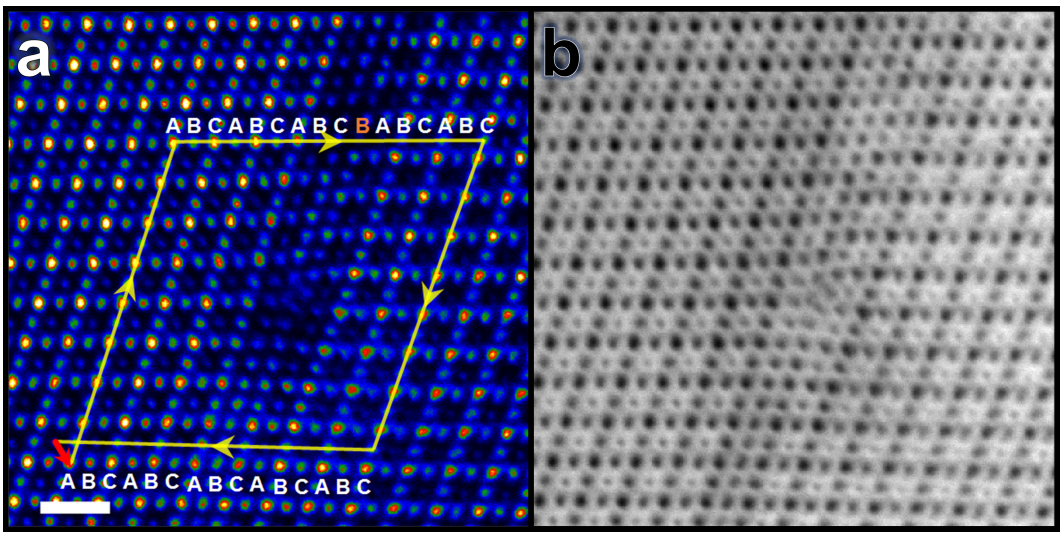

Figure 4.13: (a) An ADF-STEM image (scale bar is 1 nm) obtained from the right core of the defect displayed in Fig. 4.8(a) with overlaid Burgers circuit indicating the projection of the Burgers vector is $1/4[\bar{1}\ \bar{1}\ 0]$. (b) A BF-STEM image acquired simultaniuosly with (a).

irradiation probably produces oxygen Frenkel pairs and some sample charging due to Auger emission, which interact with the point defects already in the material due to its particular stoichiometry. How this produces the defects observed is still an open question. In addition, cations site swapping as a result of migration of vacancies is expected in the vicinity of the defect area. Stuffing Yb onto Ti sites was observed in the ADF data presented in Fig. 4.4(d) and are clearly visible in the EDX elemental maps (Fig. 4.14). However, any evidence of anti-stuffing of Ti onto Yb sites was not observed. That means Ti cations choose only the vacancies in the Ti sub-lattice to migrate from the defect area. In other words, the structure of this material also contains Ti vacancies.

4.3 $Yb_{2.05}Ti_2O_{7+\xi}$

4.3.1 STEM imaging

Fig. 4.15 shows ADF- and BF-STEM images obtain from the $Yb_{2.05}Ti_2O_{7+\xi}$ sample. In addition to the cation columns (Yb, Ti and M) observed in the STEM images obtained from $Yb_2Ti_2O_7$ (Fig. 4.16) and $Yb_{1.95}Ti_2O_{7-\xi}$ (Fig. 4.13) samples, I observed anomalous columns in the STEM images for $Yb_{2.05}Ti_2O_{7+\xi}$ (Fig. 4.15). According to the position of these columns in the $[1\ \bar{1}\ 0]$ direction, the atoms in these columns reside in both the $8b$ and $48f$ tetrahedral voids, in other words, on the oxygen sites located at the tetrahedral coordination formed by only Yb cations

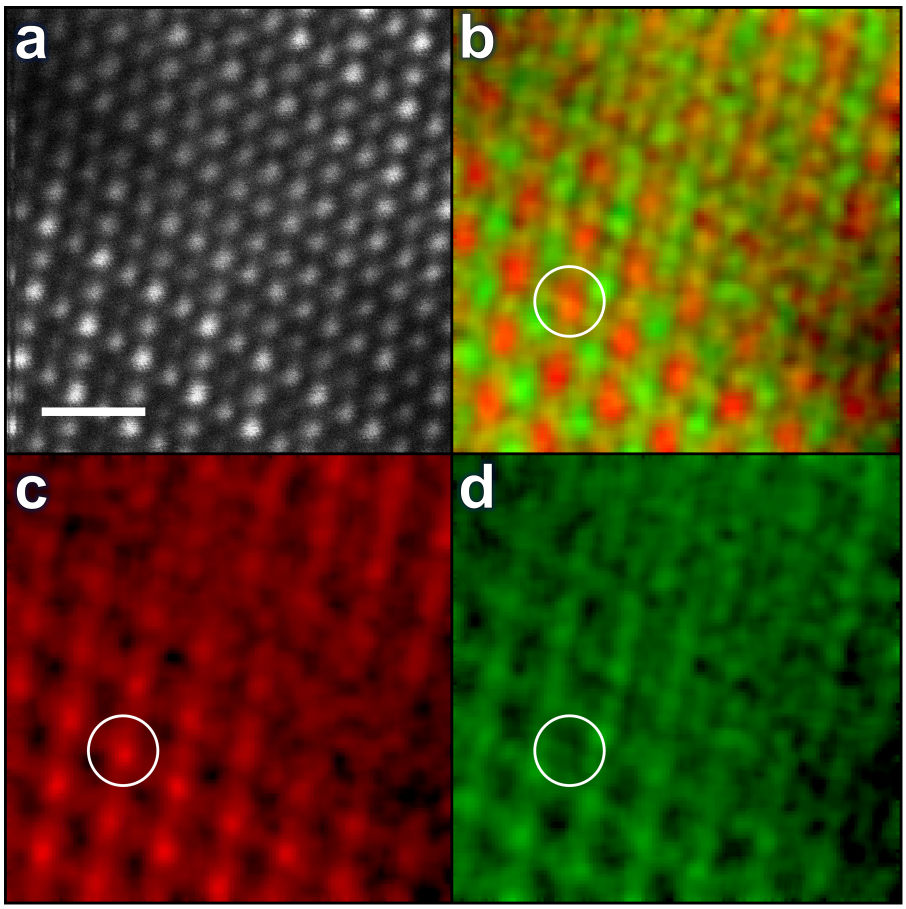

Figure 4.14: (a) ADF-STEM image across the defect shown in Fig. 4.8(a) (scale bar is 0.5 nm). (b) Atomic scale EDX map from (a); Ti and Yb signals shown in red and green, respectively. (c) Ti and (d) Yb EDX elemental maps from (a).

or two Yb and two Ti cations. However, although oxygen atoms can contribute in the ADF intensity (see Chapter 3 for more information), they must be invisible in the ADF images shown in Fig. 4.15 since with $Z = 8$ they cannot produce bright contrast in the ADF images from structures containing heavy cation columns ($Z_{Yb} = 70$ and $Z_{Ti} = 22$) [100–102]. Thus, these STEM results indicate either a fraction of the oxygen sites has been occupied by heavy atoms or there are interstitial heavy atoms in the vicinity of the oxygen columns which can enhance the electron channelling at the oxygen columns and consequently increase the electron scattering by those columns.

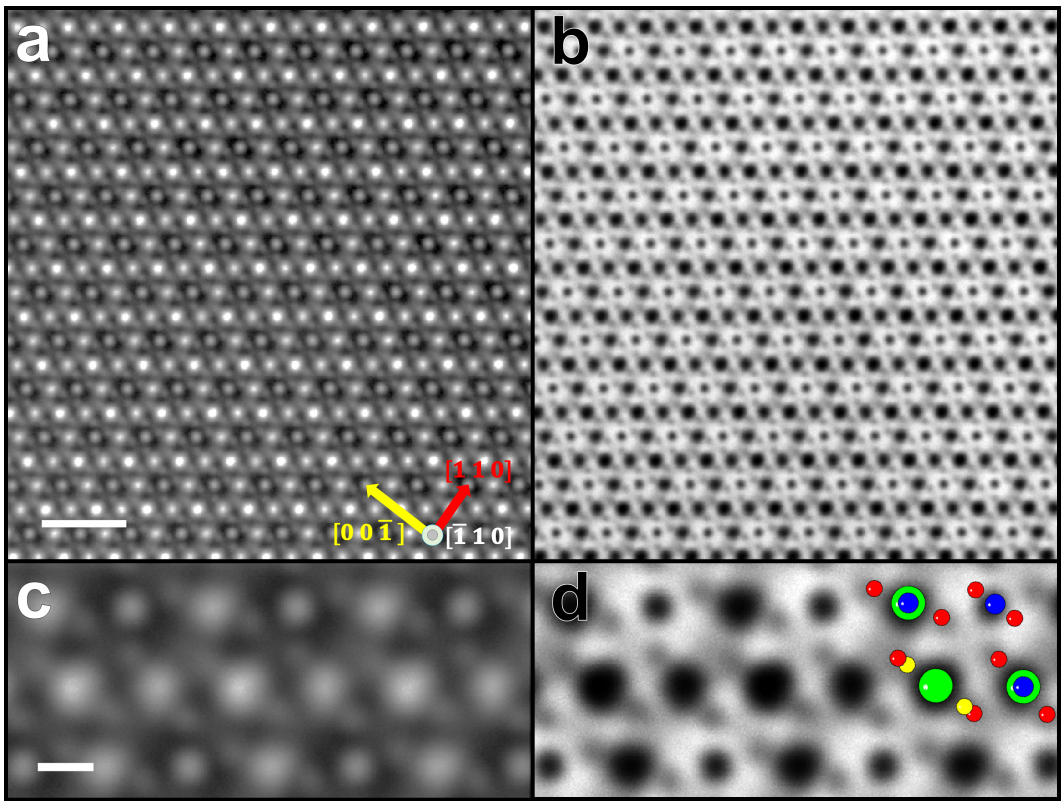

Figure 4.15: (a) ADF-STEM image (scale bar is 1 nm) taken with an ADF detector inner angle of ∼4.6α and (b) BF-STEM image acquired simultaneously with (a) from the $Yb_{2.05}Ti_2O_{7+\xi}$ sample along [1 $\bar{1}$ 0]. (c) and (d) ADF- and BF-STEM images from the sample at a higher magnification (scale bar is 2 Å). Positions of Ti, Yb, O (48f) and O (8b) are marked by the blue, green, red, and yellow circles, respectively.

4.3.2 EDX

Atomic resolution EDX was used to examine the $Yb_{2.05}Ti_2O_{7+\xi}$ sample. Fig. 4.17 shows an EDX line scan on Ti and Yb columns along [0 0 1] direction, made using Ti $K\alpha$ (4.51 keV) and Yb $L\alpha$ (7.41 keV) X-rays. As displayed in the line scan, the peaks for Yb signals are relatively broad and show shoulders or humps at about 0.2 nm along the [0 0 1] direction. I also observed the peak shoulders for Yb columns in the EDX map acquired from this sample (Fig. 4.18). While these results may indicate presence of interstitial Yb atoms in the structure of this material (e.g. in the octahedral voids), it is also possible that a small amount of specimen drift (∼0.2 nm) during acquisition introduced some signal from Yb atoms in the adjacent M columns. In addition, Yb or Ti signal was not detected at the position of those anomalous columns observed in the STEM images.

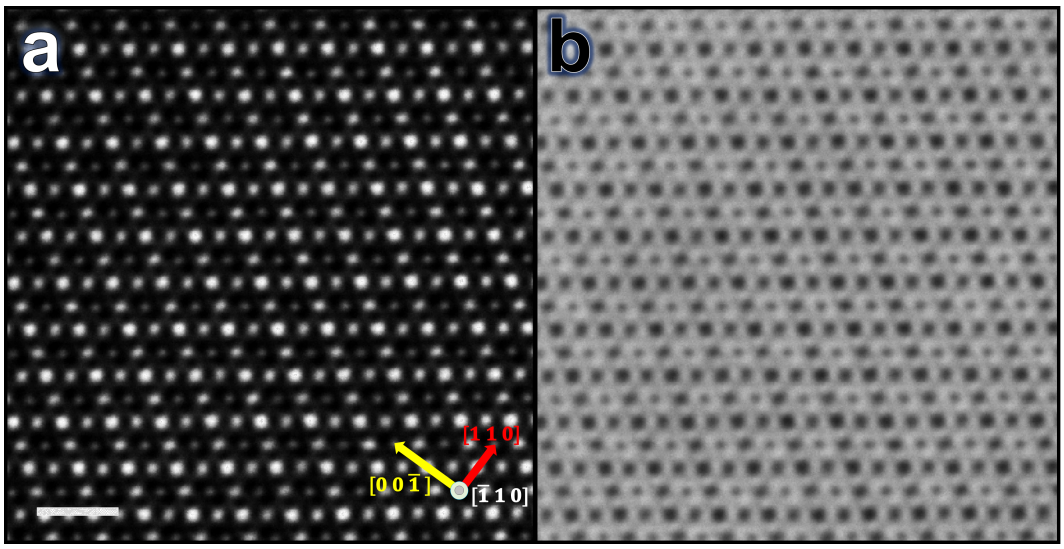

Figure 4.16: (a) ADF-STEM image (scale bar is 1 nm) taken with an ADF detector inner angle of $\sim 4.6\alpha$ and (b) BF-STEM image acquired simultaneously with (a) from a $Yb_2Ti_2O_7$ single crystal along [1 $\bar{1}$ 0].

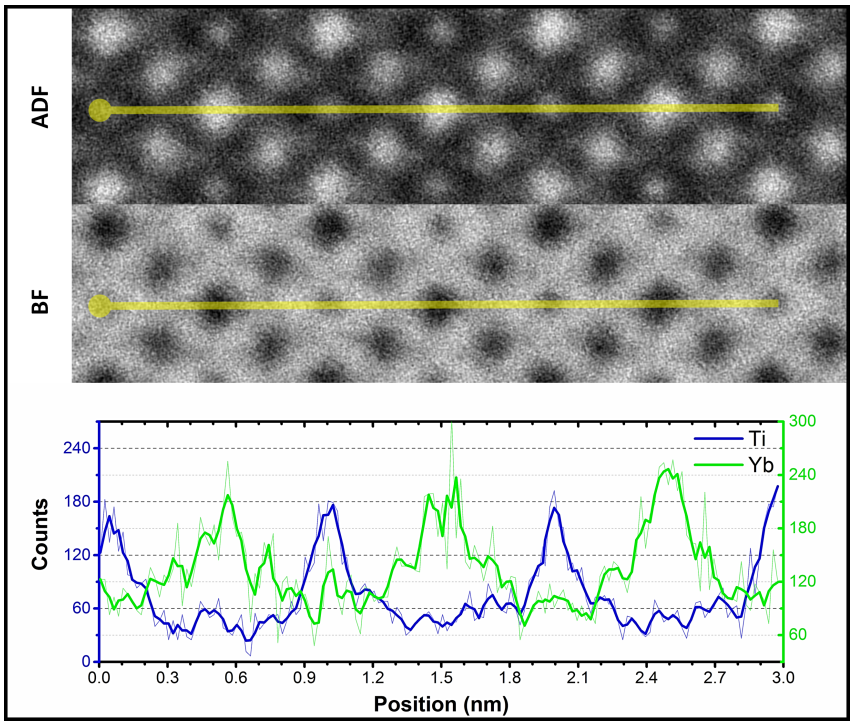

Figure 4.17: [1 $\bar{1}$ 0] ADF- and BF-STEM images as well as EDX analysis of the $Yb_{2.05}Ti_2O_{7+\xi}$ sample. Atomic scale EDX analysis along a line of Ti and Yb atom columns ([0 0 1]) showing shoulders or humps in the Yb signals.

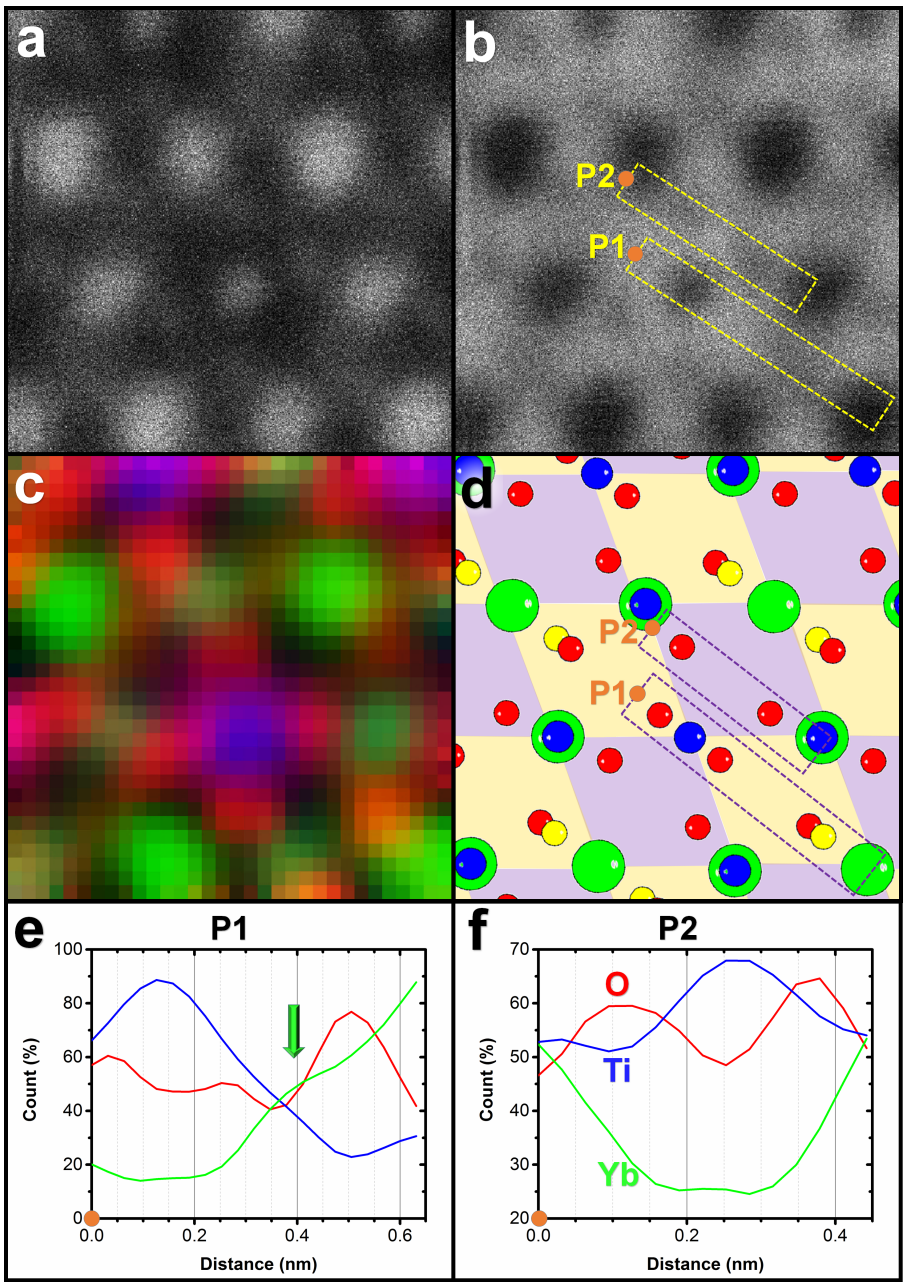

Figure 4.18: (a) and (b) ADF- and BF-STEM images taken from the $Yb_{2.05}Ti_2O_{7+\xi}$ sample along [1 $\bar{1}$ 0], respectively (images are 1 nm by 1 nm). (c) The corresponding atomic resolution EDX map for the STEM images shown in (a) and (b); here the Ti, Yb and O columns are colored in blue, green and red, respectively. (d) Schematic of the position of the atom columns in the STEM images as well as the EDX map; here the colour scheme is the same as in (c) but the O (8*b*) positions are shown in yellow. In addition, octahedral voids are filled in light yellow and purple. (e) and (f) Elemental EDX profiles along the $P1$ and $P2$ dashed rectangles displayed in (b), respectively.

4.3.3 EELS

Figs. 4.19(a) and (b) show an ADF-STEM and EELS map acquired simultaneously from the $Yb_{2.05}Ti_2O_{7+\xi}$ sample. As shown in the EELS maps (Figs. 4.19(b) and (d)) as well as the intensity profile (Fig. 4.19(g)), some of the octahedral voids, (areas filled in yellow in Fig. 4.19(c)), are occupied by Yb atoms. Figs. 4.19(b), (d) and (h) reveal that no Yb signal is detected from those octahedra filled in purple in Fig. 4.19(c).

ELNES spectra can be used to obtain information on the Ti-O bonding configurations [145–147]. In ytterbium titanate, as mentioned in Chapter 3, the Ti L_3 and L_2 edges both consist of two white lines, α and β for L_3 and γ and δ for L_2. For each edge, the first (α, γ) and second (β, δ) peaks are due to transitions from the $2p$ state to the $2t_{2g}$ (π^*) and $3e_g$ (σ^*) oxide levels, respectively. The experimental Ti-$L_{3,2}$ ELNES obtained from $Yb_2Ti_2O_7$ and $Yb_{2.05}Ti_2O_{7+\xi}$ are illustrated in Fig. 4.20(a). Peak energies, extracted by fitting the data to four Lorentzian curves (Fig. 4.20(b)), as well as intensity ratios, are listed in Table 4.1. The intensity ratios in $Yb_{2.05}Ti_2O_{7+\xi}$ I_α/I_β, I_δ/I_γ and I_β/I_δ are all larger than those observed for the $Yb_2Ti_2O_7$ sample, while both the L_3 and L_2 edges are shifted to lower energies in $Yb_{2.05}Ti_2O_{7+\xi}$. These indicators show that the Ti valence drops from $Yb_2Ti_2O_7$ to $Yb_{2.05}Ti_2O_{7+\xi}$. This drop in Ti valence state is probably a result of oxygen vacancies and/or stuffed Yb atoms on Ti sites [145, 146].

Table 4.1: Ti ELNES energies and intensity ratios for the $Yb_2Ti_2O_7$ single crystal and $Yb_{2.05}Ti_2O_{7+\xi}$ powder samples.

		$Yb_2Ti_2O_7$	$Yb_{2.05}Ti_2O_7$
L_3	E_α	459.99 ± 0.01	459.86 ± 0.01
	E_β	462.17 ± 0.02	462.09 ± 0.02
	I_β/I_α	2.31 ± 0.11	2.41 ± 0.16
L_2	E_γ	465.42 ± 0.02	465.28 ± 0.02
	E_δ	467.63 ± 0.02	467.51 ± 0.02
	I_δ/I_γ	2.41 ± 0.13	2.95 ± 0.19

The experimental LL EELS spectra for the $Yb_2Ti_2O_7$ and $Yb_{2.05}Ti_2O_{7+\xi}$ samples are presented in Fig. 4.21(a). Since ytterbium titanate consists of two separate sublattices of Yb_2O_3 and TiO_2, it is possible to identify LL peaks of this material by using LL spectra of the Yb and Ti oxides as references. As displayed in Fig. 4.21(b), the main structures for Yb_2O_3 are a strong bulk plasmon peak, Y_1, at about 16.3 eV [156, 157] and two peaks, Y_2 and Y_3, related to the $5p$ to $5d$ transitions (Yb

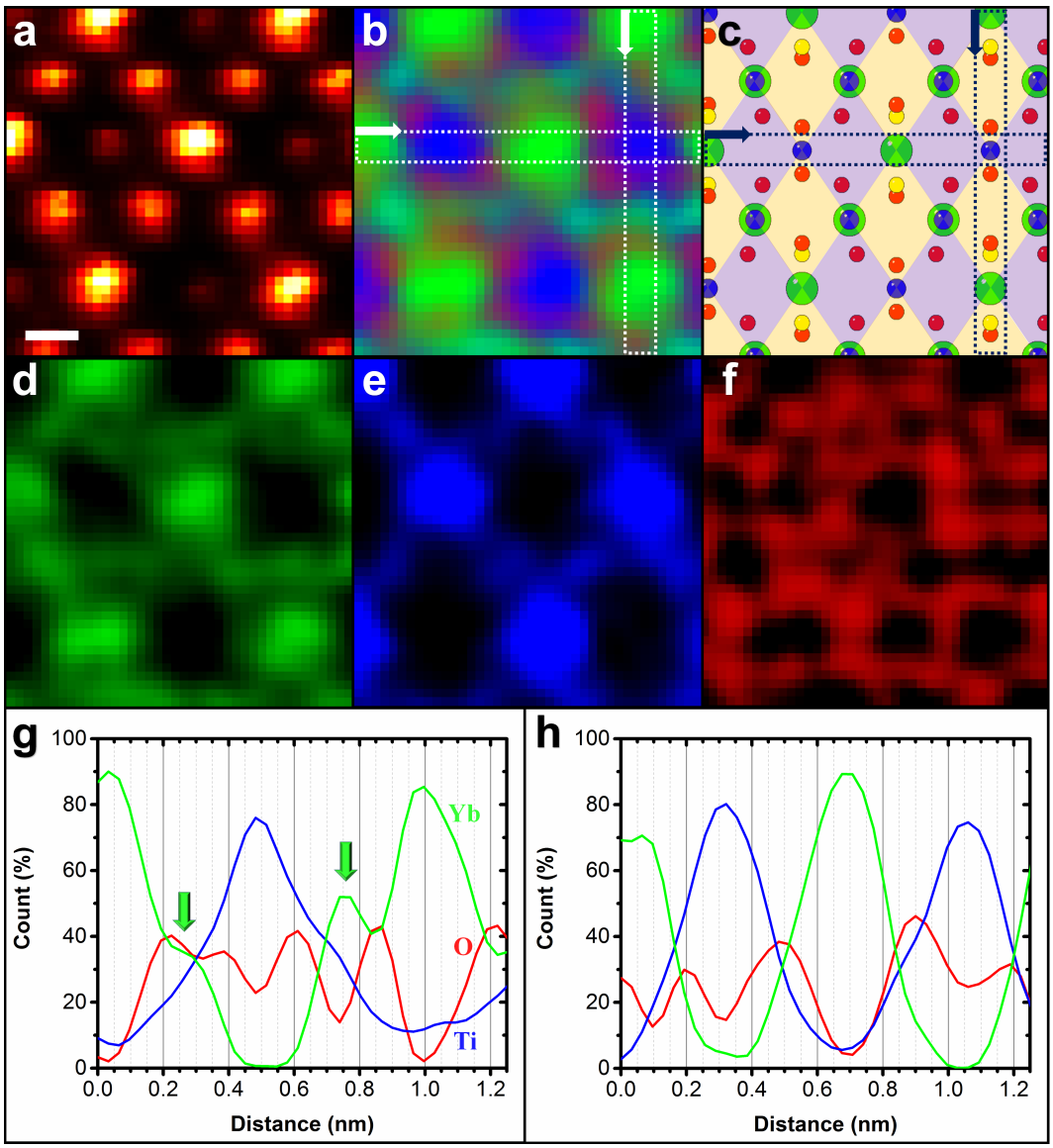

Figure 4.19: (a) HAADF image taken from the $Yb_{2.05}Ti_2O_{7+\xi}$ sample along [1 $\bar{1}$ 0] (scale bar is 2 Å). (b) Atomic resolution EELS map ($t/\Lambda = 0.29$) acquired simultaneously with (a); here the Ti, Yb and O columns are colored in blue, green and red, respectively. (c) Schematic of the position of the atom columns in (a) and (b); here the colour scheme is the same as in (b) but the O ($8b$) positions are shown in yellow. (d) Yb, (e) Ti and (f) O EELS maps of (a). (g) and (h) Elemental EELS profiles along the vertical and horizontal dashed rectangles displayed in (b), respectively.

$O_{2,3}$-edges) [156, 157]. On the other hand, TiO_2 exhibits four distinct peaks in the LL region; these peaks are due to O2p (valence band) to Ti3d (T_1), bulk plasmon (T_2), O2p (valence band) to Ti4sp (T_3) and Ti3p resonance (T_4) at energy losses of 6.6, 11.8, 25.7 and 46 eV, respectively [158]. All the peaks observed in the LL

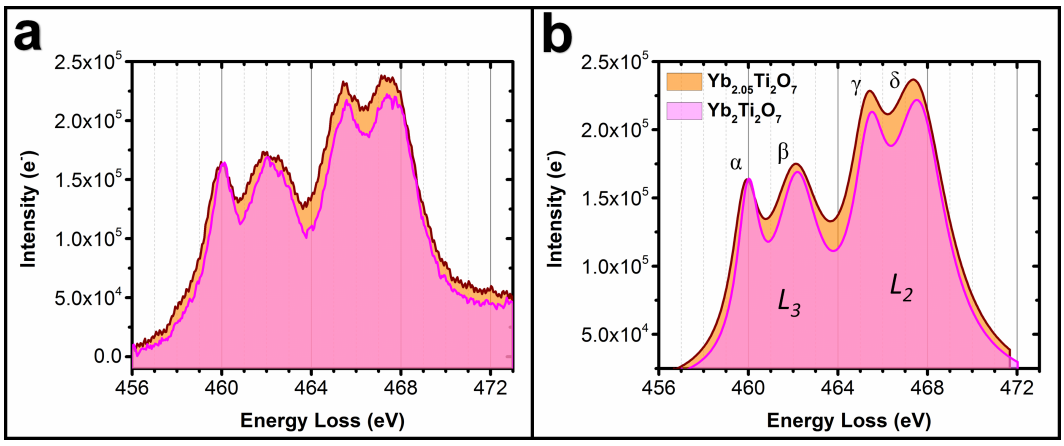

Figure 4.20: (a) Ti $L_{3,2}$ EELS spectra of the $Yb_2Ti_2O_7$ and $Yb_{2.05}Ti_2O_{7+\xi}$ samples (t/Λ = 0.41). (b) Lorentzian curves fitted to the EELS spectra shown in (a).

spectra for both the Ti and Yb oxides are presented in the experimental spectra of ytterbium titanate samples. However, $Yb_{2.05}Ti_2O_{7+\xi}$ exhibits an extra peak, Y_0, shown by a grey arrow in Fig. 4.21(a), at ~2.5 eV. This peak, as Gorschluter et al. [157] reported, could be due to an inhomogeneous oxidation of Yb_2O_3 sub-lattice in $Yb_{2.05}Ti_2O_{7+\xi}$.

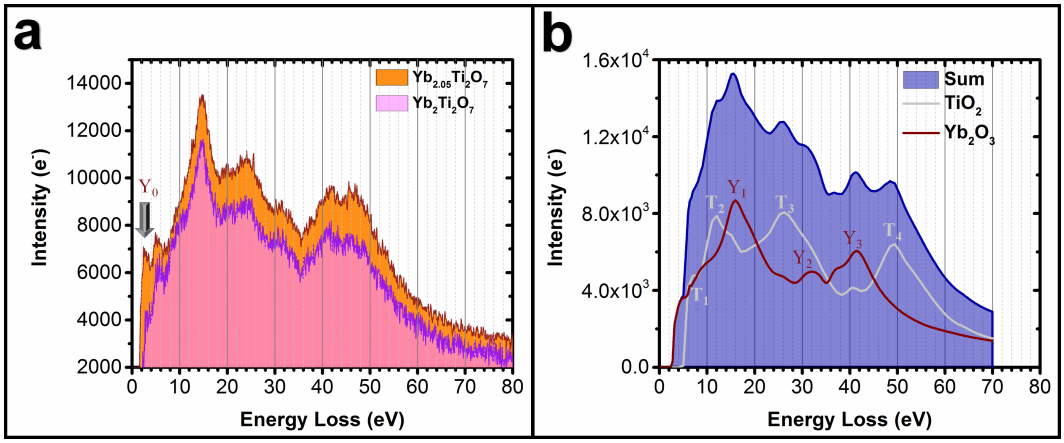

Figure 4.21: (a) LL spectra from the $Yb_2Ti_2O_7$ and $Yb_{2.05}Ti_2O_{7+\xi}$ samples ($t/\Lambda = 0.41$). (b) LL spectra for TiO_2 and Yb_2O_3 as well as their superposition obtained from the Gatan EELS atlas [159, 160].

4.3.4 Discussion

Anomalous columns are clearly observed in the STEM images for $Yb_{2.05}Ti_2O_{7+\xi}$ (Fig. 4.15) indicating that either a fraction of the oxygen sites has been occupied by

heavy atoms or that there are interstitial heavy atoms in the vicinity of the oxygen columns which can enhance the electron channelling at the oxygen columns and consequently increase the electron scattering by those columns. One could argue against these proposals by asking why, if heavy atoms occupy the oxygen sites or are very close to the centre of the oxygen atoms in the [1 1 0] viewing direction, are not the oxygen columns in the vicinity of Ti columns visible? The fact that the oxygen columns around the Ti columns cannot be seen can be explained by noting that, in the [1 1 0] direction, there are half the number of occupied oxygen sites around the Ti columns as compared to the sites around the Yb or M columns. This is due to the fact that half of the closest tetrahedral voids around the Ti columns are formed by only Ti cations which are not occupied by the oxygen atoms. This means that while there are n oxygen sites around the Yb or M columns, there are only $n/2$ oxygen sites around the Ti columns. Hence, stuffing heavy atoms on the oxygen sites or the presence of heavy interstitial atoms may not sufficiently enhance the electron scattering to make the O columns close to the Ti columns visible in the STEM images.

The results from atomic resolution EDX and atomic resolution EELS maps (Figs. 4.18 and 4.19), show that the Yb atoms are not on the oxygen sites and support the proposal that there are interstitial Yb atoms in the vicinity of the oxygen columns in the $Yb_{2.05}Ti_2O_{7+\xi}$ sample. Detection of Yb interstitial atoms in ytterbium titanate indicates cation Frenkel defects can be stable in the titanate pyrochlres. I note, however, that interstitial Yb atoms were only observed in the octahedra filled in yellow in Fig. 4.19(c) and not in the ones filled in purple. Although all the octahedral voids are surrounded by the same configuration of Ti, Yb and O atoms (Fig. 4.22(a)) in ytterbium titanate, as displayed schematically in Figs. 4.22(d) and (e), there are two different types of octahedron chains when the crystal is viewed along the [1 1 0] direction.

One type ($O1$), shown in Fig. 4.22(d), is formed by an alternate repetition of the octahedron shown in Fig. 4.22(b) and its rotation about the vertical axes by 180 degrees. The second type ($O2$) which is displayed in Fig. 4.22(d) is made up of an alternate stacking of the octahedron shown in Fig. 4.22(c) and its rotation about the horizontal axes by 180 degrees. Since there are more oxygen atoms on one side of each octahedron e.g. down the side of the octahedron shown in Fig. 4.22(a), this variation in the arrangement of the octahedra causes a difference in the concentration of oxygen around these octahedron chains. In the $O1$ chains, all the octahedra are configured in such a way that the side with a higher concentration of O is always located one side of the chains (e.g. down side of the chain in Fig. 4.22(d)).

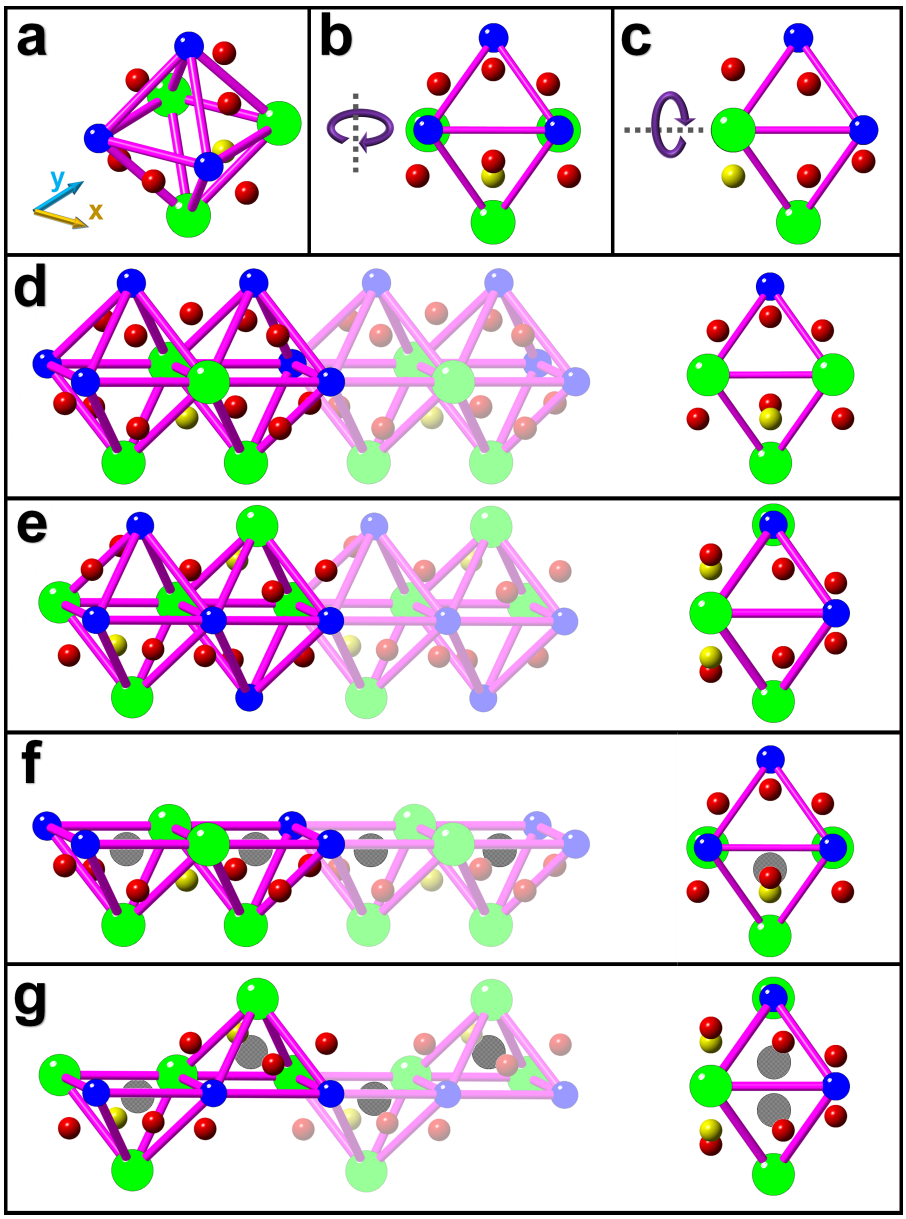

Figure 4.22: (a) Configuration of the Ti, Yb and O atoms around an octahedral void in ytterbium titanate. (b) and (c) Atomic positions around the octahedral void shown (a) when viewed along x and y, respectively. (d) Left: a chain of octahedra, $O1$, formed by alternate repetition of the octahedron shown in (b) and its rotation about the vertical axes by 180 degrees; right: $O1$ when viewed along [1 1 0]. (e) Left: a chain of octahedra, $O2$, made of alternate repetition of the octahedron shown in (c) and its rotation about the horizontal axes by 180 degrees; right: $O2$ when viewed along [1 1 0]. (f) and (g) Preferred side of the octahedra for the interstitial Yb atoms to reside (shown in gray) in the $O1$ and $O2$ chains, respectively.

Therefore, as shown schematically in Fig. 4.22(f) all the interstitial Yb cations would reside on one side of the $O1$ chains, that is the side with a higher concentration of oxygen. However, the areas with high concentrations of oxygen are equally located in both sides of the $O2$ chains (Fig. 4.22(e)). In the $O2$ chains, depending on which octahedron void is occupied, the interstitial Yb cation would move toward the upper or lower side of the chains (Fig. 4.22(g)). Thus, all the interstitial Yb cations in the $O1$ chains would be aligned in a single column along the [1 1 0] direction while those in the $O2$ chains would reside in two separate columns. This is consistent with the EELS map results. In fact, detection of the Yb cations inside the $O1$ chains (filled in yellow in Fig. 4.19(c)) is due to the presence of these cations, which may be few in number along a single column, can enhance drastically the EELS signal for Yb. In contrast, since the interstitial cations reside in two separate columns inside the $O2$ chains (filled in purple in Fig. 4.19(c)), the number of cations aligned in a single column inside these chains is about a half the number of cations detected in the Yb columns inside the $O1$ chains. This explains why the Yb cations were not detected in the $O2$ chains. On the other hand, the configurations for the interstitials shown in Figs. 4.22(f) and (g), with Yb cations close to oxygen columns, make the oxygen columns visible in the ADF-STEM provided in Fig. 4.15. The above mentioned proposal for the position of interstitial Yb atoms was examined by image simulations and the resulting data are presented in Fig. 4.23. As shown in Fig. 4.23(b), presence of the Yb interstitials in the octahedral voids increases the electron scattering by the adjacent oxygen columns and, therefore, makes those columns visible in the ADF images.

The presence of these Yb interstitials in the octahedral voids of the $Yb_{2.05}Ti_2O_{7+\xi}$ sample requires the introduction of more oxygen atoms into the structure ($\xi = 0.075$) or a reduction in the valence states of their nearby Ti/Yb cations ($\xi = 0$) or a combination of the two ($0 < \xi < 0.075$). The Ti-$L_{3,2}$ ELNES shows that Ti cations in this sample have lower valence numbers in comparison to those in $Yb_2Ti_2O_7$. In addition, LL spectra acquired from the $Yb_{2.05}Ti_2O_{7+\xi}$ sample showed Yb is partially oxidized in this sample. Although these results indicate that the Yb interstitials reduce their nearby cations at least to some extent, charge balance may also require the presence of O interstitials in this sample. Hence, the parameter ξ may not be exactly zero.

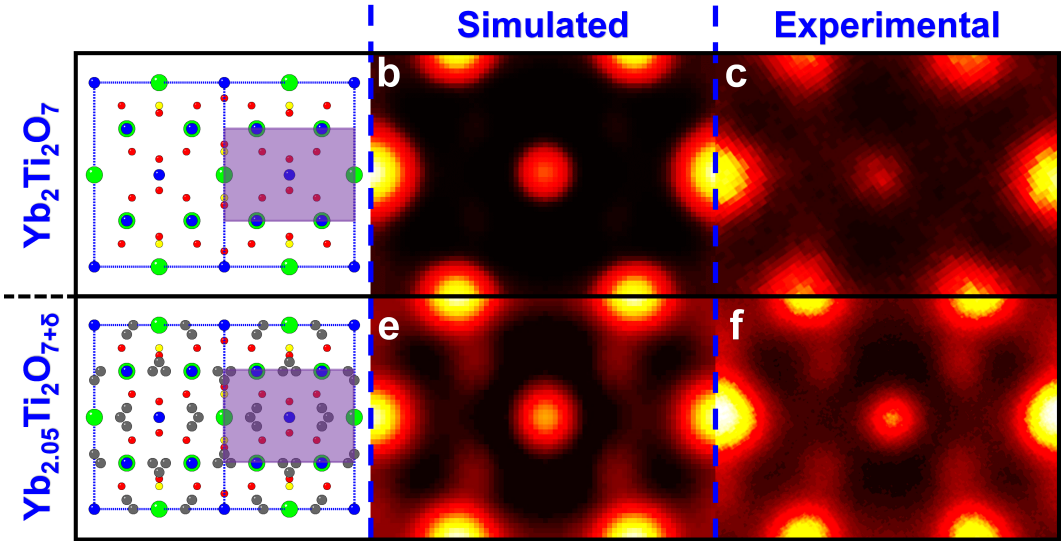

Figure 4.23: (a) Schematic of the position of the atom columns in a unit-cell of a perfect $Yb_2Ti_2O_7$ crystal viewd along the [1 1 0] direction (colour scheme is the same as Fig. 4.22). (b) The simulated ADF-STEM image (by QSTEM; thickness of 34 nm) and (c) experimental ADF-STEM image of the area highlited in purple shown in (a). (d) Schematic of the position of the atom columns in a unit-cell proposed for the $Yb_{2.05}Ti_2O_{7+\xi}$ crystal viewd along the [1 1 0] direction; the Yb interstitials (occupancy of 0.0052) are located at the fractional coordinates of 1/4, 1/4, 3/10 (colour scheme is the same as Fig. 4.22). (e) The simulated ADF-STEM image (by QSTEM; thickness of 34 nm) and (f) experimental ADF-STEM image of the area highlited in purple shown in (d).

4.4 Summary

The excess of Ti cations gives rise to the formation of Yb vacancies in ytterbium titanate (e.g. $Yb_{1.95}Ti_2O_{7-\xi}$). This is consistent with the theoretical studies of Stanek et al. [16]. The results indicate that the presence of ~2.5% Yb vacancies, which reduces the activation energy for cation migration in ytterbium titanate, paves the way for the formation of anti-site defects as well as dislocations during electron irradiation. This may mean that the susceptibility to amorphization in the pyrochlore oxides can be reduced in general by introducing a small number of vacancies at the A sites. In addition, electron-induced defects in $Yb_{1.95}Ti_2O_{7-\xi}$ were characterized using in-house program, BurgersVectors. It was demonstrated that $1/2 < 1\ 0\ 0 >$ dislocations, dissociating into $1/4 < 1\ 1\ 0 >$ dislocations can be formed in the pyrochlore structure.

Atomic resolution EDX and EELS results showed that a fraction of octahedral voids in $Yb_{2.05}Ti_2O_{7+\xi}$ are occupied by Yb cations. Such a solution for excess Yb (A site) has not been considered in the previous theoretical studies of non-stoichiometric

$A_2B_2O_7$ pyrochlores [16]. In addition, I cast doubt on the previous X-ray diffraction results suggesting that the lattice swelling in the titanate pyrochlores, induced as a result of deviation from stoichiometry or ion irradiation, is related *only* to the anti-site defects [17–19].

Chapter 5

Conclusions and future work

The main aim of this thesis was to explain unusual low-temperature magnetic behaviour of pyrochlore $Yb_2Ti_2O_7$. Ytterbium titanate is one of the most intriguing members of the pyrochlore titanate family of frustrated magnetic materials. Unlike some other members of this family, experimental efforts to establish the ground state and correlate this to the structural features of this material have been made difficult by the fact that different samples of the same material are found to exhibit completely different results – with no satisfactory explanation of the links between subtle structural variations. This is the case even for material produced through nominally identical synthesis routes, as is the case in this study.

In chapter 3, I used aberration-corrected STEM to study this material at the atomic scale, and have developed new methods to analyse the resulting data that can be extended to other pyrochlores, dilute compounds and compounds containing a mix of light and heavy elements. Additionally, I used X-ray analysis with atomic resolution to show for the first time that "stuffing" of Yb atoms onto Ti sites in the lattice can be observed directly, and also used EELS to link this to Ti valence state. In combination these different techniques, which have been developed for the first time here, or have not been applied to the study of these materials, I showed correlations between stuffing, oxygen vacancies and Ti valence state that can be related to the low-temperature magnetic behaviour of this material.

On the other hand, atomic structure of non-stoichiometric ytterbium titanate with Ti or Yb excess was investigated in chapter 4. Experimental results, consistent with the theoretical studies of Stanek et al. [16], showed Ti excess was compensated by formation of Yb vacancies in $Yb_{1.95}Ti_2O_{7-\xi}$. Although formation of vacancies on the B site has not been previously reported in the structure of non-stoichiometric pyrochlores with B excess, the results indicated that structure of $Yb_{1.95}Ti_2O_{7-\xi}$

contains Ti vacancies. Furthermore, formation of extended defects under 200 kV electron irradiation was observed in Ti-rich material, in particular with 2.5 at.% excess Ti. While dislocations in pyrochlore structure have not been studied in detail in literature, detailed investigation presented in chapter 4 showed that $1/2 < 1\ 0\ 0 >$ dislocations, dissociating into $1/4 < 1\ 1\ 0 >$ dislocations, can be formed in the pyrochlore structure.

In addition, Yb interstitials were directly observed using atomic resolution EDX and EELS in Yb-rich ytterbium titanate, $Yb_{2.05}Ti_2O_{7+\xi}$. While previous theoretical and experimental works suggested that extra A cations in the pyrochlore structure stuffed onto B sites [17–19], this study demonstrated that extra Yb can be accommodated in the octahedral voids. Therefore, since the pyrochlore structure of ytterbium titanate can accommodate Yb interstitials, cation Frenkel defects – e.g. as a result of ion irradiation – could be stable in this structure. That is in contrast to the results reported by Li et al. [17] indicated cation Frenkel defects cannot be stable in titanate pyrochlores. Moreover, Ti-$L_{3,2}$ ELNES analysis proved that Ti cations could have valance number lower that 4+ in $Yb_{2.05}Ti_2O_{7+\xi}$. This means that the excess positive charge induced by Yb interstitials can be balanced by not only introduction of oxygen interstitials [16] but also reduction in the Ti valance state.

The methods described here can readily be applied to other pyrochlore systems where a similar sensitivity to structural defects, including stuffing [13], has recently been shown to lead to significant differences in the magnetic behaviour, for example, the magnetic ground state of the spin liquid candidate $Tb_2Ti_2O_7$ [161] and magnetic monopole dynamics in spin ice $Dy_2Ti_2O_7$ [162]. Studies of this kind should also prove useful in understanding the physics of other frustrated magnets where defects or low levels of doping rapidly modify the physics; examples include triangular lattice magnets such as $CuFeO_2$ and $RbFe(MoO_4)_2$, and order-disorder transitions that occur in several lattice motifs. More generally, such methods could play a valuable role in the study of emergent phenomena, including superconductivity and magnetism, both in the bulk and at interfaces, when defects are known to be important.

Finally, although the experimental studies presented in this thesis relieved that the exotic low temperature magnetic properties of $Yb_2Ti_2O_7$ is due to stuffing Yb atoms on the Ti sites as well as presence of defect in the oxygen sublattice, they are not quantitatively shown the degree of stuffing or the density of defects in the samples. Hence, it would be an interesting work to quantitatively link the level of defect density in this material to its low temperature magnetic properties by applying experimental quantitative STEM and EELS as well as theoretical studies using

density functional theory (DFT) methods. Furthermore, the experimental results shown in chapter 4 indicated that the structure of ytterbium titanate can tolerate cation vacancies as well as interstitial Yb atoms, however, the maximum amount of the cation vacancies and interstitial atoms that the crystal of this material is able to tolerate are still unknown. Therefore, atomic structure study of ytterbium titanate with several different levels of cation deficiency ($Yb_{2\pm x}Ti_2O_{7\pm\xi}$ where $x < 0.05$) as a future work is recommended.

Bibliography

[1] A. V. Krasheninnikov and K. Nordlund. Ion and electron irradiation-induced effects in nanostructured materials. *Journal of Applied Physics*, 107(1):071301, 2010.

[2] M. A. Subramanian, G. Aravamudan, and G. V. S. Rao. Oxide pyrochlores - a review. *Progress in Solid State Chemistry*, 15(2):55–143, 1983.

[3] S. W. Jiang, Y. R. Li, R. G. Li, N. D. Xiong, L. F. Tan, X. Z. Liu, and B. W. Tao. Dielectric properties and tunability of cubic pyrochlore $Bi_{1.5}MgNb_{1.5}O_7$ thin films. *Applied Physics Letters*, 94(16):162908, 2009.

[4] E. K. Michael and S. Trolier-McKinstry. Bismuth pyrochlore thin films for dielectric energy storage. *Journal of Applied Physics*, 118(5):054101, 2015.

[5] M. Mirsaneh, B. E. Hayden, E. Furman, S. Perini, M. T. Lanagan, and I. M. Reaney. High dielectric tunability in lead niobate pyrochlore films. *Applied Physics Letters*, 100(8):082901, 2012.

[6] S. Gaur, D. J. Haynes, and J. J. Spivey. Rh, Ni, and Ca substituted pyrochlore catalysts for dry reforming of methane. *Applied Catalysis a-General*, 403(1-2): 142–151, 2011.

[7] S. H. Oh, R. Black, E. Pomerantseva, J. H. Lee, and L. F. Nazar. Synthesis of a metallic mesoporous pyrochlore as a catalyst for lithium-O_2 batteries. *Nature Chemistry*, 4(12):1004–1010, 2012.

[8] J. H. Ke, A. S. Kumar, J. W. Sue, S. Venkatesan, and J. M. Zen. Catalysis and characterization of a rugged lead ruthenate pyrochlore membrane catalyst. *Journal of Molecular Catalysis a-Chemical*, 233(1-2):111–120, 2005.

[9] J. M. Zen, A. S. Kumar, and H. P. Chen. Lead ruthenate pyrochlore formed in clay for sensitive determination of dopamine. *Electroanalysis*, 15(20):1584–1588, 2003.

[10] J. Lian, L. M. Wang, K. Sun, and R. C. Ewing. In situ TEM of radiation effects in complex ceramics. *Microscopy Research and Technique*, 72(3):165–181, 2009.

[11] P. Poml, M. Menneken, T. Stephan, D. R. D. Niedermeier, T. Geisler, and A. Putnis. Mechanism of hydrothermal alteration of natural self-irradiated and synthetic crystalline titanate-based pyrochlore. *Geochimica Et Cosmochimica Acta*, 71(13):3311–3322, 2007.

[12] Jason S. Gardner, Michel J. P. Gingras, and John E. Greedan. Magnetic pyrochlore oxides. *Reviews of Modern Physics*, 82(1):53–107, 2010.

[13] G. C. Lau, B. D. Muegge, T. M. McQueen, E. L. Duncan, and R. J. Cava. Stuffed rare earth pyrochlore solid solutions. *Journal of Solid State Chemistry*, 179(10):3126–3135, 2006.

[14] J. Lian, L. Wang, J. Chen, K. Sun, R. C. Ewing, J. M. Farmer, and L. A. Boatner. The order-disorder transition in ion-irradiated pyrochlore. *Acta Materialia*, 51(5):1493–1502, 2003.

[15] J. Lian, J. Chen, L. M. Wang, R. C. Ewing, J. M. Farmer, L. A. Boatner, and K. B. Helean. Radiation-induced amorphization of rare-earth titanate pyrochlores. *Physical Review B*, 68(13):134107, 2003.

[16] C. R. Stanek, L. Minervini, and R. W. Grimes. Nonstoichiometry in $A_2B_2O_7$ pyrochlores. *Journal of the American Ceramic Society*, 85(11):2792–2798, 2002.

[17] Y. H. Li, B. P. Uberuaga, C. Jiang, S. Choudhury, J. A. Valdez, M. K. Patel, J. Won, Y. Q. Wang, M. Tang, D. J. Safarik, D. D. Byler, K. J. McClellan, I. O. Usov, T. Hartmann, G. Baldinozzi, and K. E. Sickafus. Role of antisite disorder on preamorphization swelling in titanate pyrochlores. *Physical Review Letters*, 108(19):195504, 2012.

[18] D. Y. Yang, C. G. Liu, K. Q. Zhang, Y. Xia, L. J. Chen, H. Liu, and Y. H. Li. 2.7 MeV Ar^{11+} ion irradiation induced structural evolution in $Lu_2(Ti_{2-x}Lu_x)O_{7-x/2}$ pyrochlores. *Journal of Nuclear Materials*, 466:496–501, 2015.

[19] D. Y. Yang, C. P. Xu, E. G. Fu, J. Wen, C. G. Liu, K. Q. Zhang, Y. Q. Wang, and Y. H. Li. Structure and radiation effect of Er-stuffed pyrochlore $Er_2(Ti_{2-x}Er_x)O_{7-x/2}$ (x=0–0.667). *Nuclear Instruments & Methods*

in Physics Research Section B-Beam Interactions with Materials and Atoms, 356:69–74, 2015.

[20] M.S. Dresselhaus and R. Kalish. *Ion Implantation in Diamond, Graphite and Related Materials*. Springer Berlin Heidelberg, 1992.

[21] J. F. Ziegler. Stopping of energetic light ions in elemental matter. *Journal of Applied Physics*, 85(3):1249–1272, 1999.

[22] K. Yasunaga, K. Yasuda, S. Matsumura, and T. Sonoda. Electron energy-dependent formation of dislocation loops in CeO_2. *Nuclear Instruments and Methods in Physics Research Section B: Beam Interactions with Materials and Atoms*, 266(12):2877–2881, 2008.

[23] H. Y. Xiao, F. Gao, and W. J. Weber. Threshold displacement energies and defect formation energies in $Y_2Ti_2O_7$. *Journal of Physics: Condensed Matter*, 22(41):415801, 2010.

[24] Jacob Shamblin, Cameron L. Tracy, Rodney C. Ewing, Fuxiang Zhang, Weixing Li, Christina Trautmann, and Maik Lang. Structural response of titanate pyrochlores to swift heavy ion irradiation. *Acta Materialia*, 117:207–215, 2016.

[25] L. Minervini, R. W. Grimes, and K. E. Sickafus. Disorder in pyrochlore oxides. *Journal of the American Ceramic Society*, 83(8):1873–1878, 2000.

[26] M. Lang, J. Lian, J. M. Zhang, F. X. Zhang, W. J. Weber, C. Trautmann, and R. C. Ewing. Single-ion tracks in $Gd_2Zr_{2-x}Ti_xO_7$ pyrochlores irradiated with swift heavy ions. *Physical Review B*, 79(22):224105, 2009.

[27] S. T. Bramwell and M. J. P. Gingras. Spin ice state in frustrated magnetic pyrochlore materials. *Science*, 294(5546):1495–1501, 2001.

[28] A. P. Ramirez. Magic moments. *Nature*, 421(6922):483–483, 2003.

[29] L. Balents. Spin liquids in frustrated magnets. *Nature*, 464(7286):199–208, 2010.

[30] E. Ising. Beitrag zur theorie des ferromagnetismus. *Zeitschrift fur Physik*, 31 (1):253–258, 1925.

[31] L. Pauling. The structure and entropy of ice and of other crystals with some randomness of atomic arrangement. *Journal of the American Chemical Society*, 57(12):2680–2684, 1935.

[32] J. E. Greedan. Frustrated rare earth magnetism: Spin glasses, spin liquids and spin ices in pyrochlore oxides. *Journal of Alloys and Compounds*, 408: 444–455, 2006.

[33] J. N. Reimers, J. E. Greedan, and M. Sato. The crystal-structure of the spin-glass pyrochlore, $Y_2Mo_2O_7$. *Journal of Solid State Chemistry*, 72(2):390–394, 1988.

[34] H. D. Zhou, C. R. Wiebe, A. Harter, N. S. Dalal, and J. S. Gardner. Unconventional spin glass behavior in the cubic pyrochlore $Mn_2Sb_2O_7$. *Journal of Physics-Condensed Matter*, 20(32):325201, 2008.

[35] H. Yamamura, H. Nishino, K. Kakinuma, and K. Nomura. Electrical conductivity anomaly around fluorite-pyrochlore phase boundary. *Solid State Ionics*, 158(3-4):359–365, 2003.

[36] Michael W. Gaultois, Phillip T. Barton, Christina S. Birkel, Lauren M. Misch, Efrain E. Rodriguez, Galen D. Stucky, and Ram Seshadri. Structural disorder, magnetism, and electrical and thermoelectric properties of pyrochlore $Nd_2Ru_2O_7$. *Journal of Physics-Condensed Matter*, 25(18):186004, 2013.

[37] G. Sala, M. J. Gutmann, D. Prabhakaran, D. Pomaranski, C. Mitchelitis, J. B. Kycia, D. G. Porter, C. Castelnovo, and J. P. Goff. Vacancy defects and monopole dynamics in oxygen-deficient pyrochlores. *Nature Materials*, 13(5): 488–493, 2014.

[38] K. A. Ross, Th Proffen, H. A. Dabkowska, J. A. Quilliam, L. R. Yaraskavitch, J. B. Kycia, and B. D. Gaulin. Lightly stuffed pyrochlore structure of single-crystalline $Yb_2Ti_2O_7$ grown by the optical floating zone technique. *Physical Review B*, 86(17):174424, 2012.

[39] Kate A. Ross, Lucile Savary, Bruce D. Gaulin, and Leon Balents. Quantum excitations in quantum spin ice. *Physical Review X*, 1(2):021002, 2011.

[40] A. Yaouanc, P. Dalmas de Reotier, C. Marin, and V. Glazkov. Single-crystal versus polycrystalline samples of magnetically frustrated $Yb_2Ti_2O_7$: Specific heat results. *Physical Review B*, 84(17):172408, 2011.

[41] H.W.J. Blte, R.F. Wielinga, and W.J. Huiskamp. Heat-capacity measurements on rare-earth double oxides $R_2M_2O_7$. *Physica*, 43(4):549–568, 1968.

[42] Y. Yasui, M. Soda, S. Iikubo, M. Ito, M. Sato, N. Hamaguchi, T. Matsushita, N. Wada, T. Takeuchi, N. Aso, and K. Kakurai. Ferromagnetic transition of pyrochlore compound $Yb_2Ti_2O_7$. *Journal of the Physical Society of Japan*, 72 (11):3014–3015, 2003.

[43] Lieh-Jeng Chang, Shigeki Onoda, Yixi Su, Ying-Jer Kao, Ku-Ding Tsuei, Yukio Yasui, Kazuhisa Kakurai, and Martin Richard Lees. Higgs transition from a magnetic coulomb liquid to a ferromagnet in $Yb_2Ti_2O_7$. *Nature Communications*, 3:992, 2012.

[44] Lieh-Jeng Chang, Martin R. Lees, Isao Watanabe, Adrian D. Hillier, Yukio Yasui, and Shigeki Onoda. Static magnetic moments revealed by muon spin relaxation and thermodynamic measurements in the quantum spin ice $Yb_2Ti_2O_7$. *Physical Review B*, 89(18):184416, 2014.

[45] E. Lhotel, S. R. Giblin, M. R. Lees, G. Balakrishnan, L. J. Chang, and Y. Yasui. First-order magnetic transition in $Yb_2Ti_2O_7$. *Physical Review B*, 89(22): 224419, 2014.

[46] J. Gaudet, K. A. Ross, E. Kermarrec, N. P. Butch, G. Ehlers, H. A. Dabkowska, and B. D. Gaulin. Gapless quantum excitations from an ice-like splayed ferromagnetic ground state in stoichiometric $Yb_2Ti_2O_7$. *Physical Review B*, 93(6):064406, 2016.

[47] A. Yaouanc, P. D. de Reotier, L. Keller, B. Roessli, and A. Forget. A novel type of splayed ferromagnetic order observed in $Yb_2Ti_2O_7$. *Journal of Physics-Condensed Matter*, 28(42):426002, 2016.

[48] M. J. P. Gingras and P. A. McClarty. Quantum spin ice: a search for gapless quantum spin liquids in pyrochlore magnets. *Reports on Progress in Physics*, 77(5):056501, 2014.

[49] R. Applegate, N. R. Hayre, R. R. P. Singh, T. Lin, A. G. R. Day, and M. J. P. Gingras. Vindication of $Yb_2Ti_2O_7$ as a model exchange quantum spin ice. *Physical Review Letters*, 109(9):097205, 2012.

[50] K. A. Ross, L. R. Yaraskavitch, M. Laver, J. S. Gardner, J. A. Quilliam, S. Meng, J. B. Kycia, D. K. Singh, Th Proffen, H. A. Dabkowska, and B. D. Gaulin. Dimensional evolution of spin correlations in the magnetic pyrochlore $Yb_2Ti_2O_7$. *Physical Review B*, 84(17):174442, 2011.

[51] R. M. D'Ortenzio, H. A. Dabkowska, S. R. Dunsiger, B. D. Gaulin, M. J. P. Gingras, T. Goko, J. B. Kycia, L. Liu, T. Medina, T. J. Munsie, D. Pomaranski, K. A. Ross, Y. J. Uemura, T. J. Williams, and G. M. Luke. Unconventional magnetic ground state in $Yb_2Ti_2O_7$. *Physical Review B*, 88(13):134428, 2013.

[52] J. A. Hodges, P. Bonville, A. Forget, A. Yaouanc, P. de Reotier, G. Andre, M. Rams, K. Krolas, C. Ritter, P. C. M. Gubbens, C. T. Kaiser, P. J. C. King, and C. Baines. First-order transition in the spin dynamics of geometrically frustrated $Yb_2Ti_2O_7$. *Physical Review Letters*, 88(7):077204, 2002.

[53] J. S. Gardner, G. Ehlers, N. Rosov, R. W. Erwin, and C. Petrovic. Spin-spin correlations in $Yb_2Ti_2O_7$: A polarized neutron scattering study. *Physical Review B*, 70(18):180404, 2004.

[54] K. A. Ross, J. P. C. Ruff, C. P. Adams, J. S. Gardner, H. A. Dabkowska, Y. Qiu, J. R. D. Copley, and B. D. Gaulin. Two-dimensional kagome correlations and field induced order in the ferromagnetic XY pyrochlore $Yb_2Ti_2O_7$. *Physical Review Letters*, 103(22):227202, 2009.

[55] Lucile Savary and Leon Balents. Coulombic quantum liquids in spin-1/2 pyrochlores. *Physical Review Letters*, 108(3):037202, 2012.

[56] L. D C Jaubert, Owen Benton, Jeffrey G. Rau, J. Oitmaa, R. R P Singh, Nic Shannon, and Michel J. P Gingras. Are multiphase competition and order by disorder the keys to understanding $Yb_2Ti_2O_7$? *Physical Review Letters*, 115 (26):267208, 2015.

[57] J. Robert, E. Lhotel, G. Remenyi, S. Sahling, I. Mirebeau, C. Decorse, B. Canals, and S. Petit. Spin dynamics in the presence of competing ferromagnetic and antiferromagnetic correlations in $Yb_2Ti_2O_7$. *Physical Review B*, 92(6):064425, 2015.

[58] Kristen Baroudi, Bruce D. Gaulin, Saul H. Lapidus, Jonathan Gaudet, and R. J. Cava. Symmetry and light stuffing of $Ho_2Ti_2O_7$, $Er_2Ti_2O_7$, and $Yb_2Ti_2O_7$ characterized by synchrotron x-ray diffraction. *Physical Review B*, 92(2):024110, 2015.

[59] W.J. Croft. *Under the Microscope: A Brief History of Microscopy*. World Scientific, 2006.

[60] H.C. King. *The History of the Telescope*. Dover Books on Astronomy Series. Dover Publications, 1955. ISBN 9780486432656.

[61] E.M. Slayter and H.S. Slayter. *Light and Electron Microscopy*. Cambridge University Press, 1992.

[62] D.B. Williams and C.B. Carter. *Transmission Electron Microscopy: A Textbook for Materials Science*. Springer, 2009.

[63] K. Chang. Nobel laureates pushed limits of microscopes. *The New York Times*, 08 October 2014. Available: `https://www.nytimes.com/2014/10/09/science/nobel-prize-chemistry.html`.

[64] G. Huszka, H. Yang, and M. A. M. Gijs. Microsphere-based super-resolution scanning optical microscope. *Optics Express*, 25(13):15079–15092, 2017.

[65] Louis De Broglie. Recherches sur la thorie des quanta. *Annales de Physique*, 3:22–128, 1925.

[66] M. Knoll and E. Ruska. Das elektronenmikroskop. *Zeitschrift fr Physik*, 78 (5):318–339, 1932.

[67] K. Peck. What microscopes do you use to see microbes?, 2013. URL `http://penpals.web.unc.edu/2013/04/14/what-microscopes-do-you-use-to-see-microbes/`.

[68] B. Fultz and J.M. Howe. *Transmission Electron Microscopy and Diffractometry of Materials*. Springer Berlin Heidelberg, 2012.

[69] Sergei A. Aseyev, Peter M. Weber, and Anatoli A. Ischenko. Ultrafast electron microscopy for chemistry, biology and material science. *Journal of Analytical Sciences, Methods and Instrumentation*, 3(1):30–53, 2013.

[70] O. Scherzer. Uber einige fehler von elektronenlinsen. *Zeitschrift fr Physik*, 101:593–603, 1936.

[71] B.L. Rickman and W.A. Schroeder. Circumventing Scherzer's theorem: Large numerical aperture objective lenses for pulsed electron microscopy. *Microscopy and Microanalysis*, 20(S3):948–949, 2014.

[72] Knut W. Urban, Chun-Lin Jia, Lothar Houben, Markus Lentzen, Shao-Bo Mi, and Karsten Tillmann. Negative spherical aberration ultrahigh-resolution imaging in corrected transmission electron microscopy. *Philosophical Transactions of the Royal Society A: Mathematical, Physical and Engineering Sciences*, 367(1903):3735–3753, 2009.

[73] Rolf Erni, Marta D. Rossell, and Philip N. H. Nakashima. Optimization of exit-plane waves restored from HRTEM through-focal series. *Ultramicroscopy*, 110(2):151–161, 2010.

[74] Dorin Geiger, Hannes Lichte, Martin Linck, and Michael Lehmann. Electron holography with a Cs-corrected transmission electron microscope. *Microscopy and Microanalysis*, 14(1):68–81, 2008.

[75] R. Erni. *Aberration-corrected Imaging in Transmission Electron Microscopy: An Introduction*. Imperial College Press, 2010.

[76] J. Kirkland. *Advanced Computing in Electron Microscopy*. Springer, 2010.

[77] O. Scherzer. The theoretical resolution limit of the electron microscope. *Journal of Applied Physics*, 20(1):20–29, 1949.

[78] Peter Goodhew. *General Introduction to Transmission Electron Microscopy (TEM)*, pages 1–19. John Wiley & Sons, Ltd, 2011.

[79] Peter J. Goodhew, F. J. Humphreys, and R. Beanland. *Electron microscopy and analysis*. Taylor & Francis, London; New York, 2001.

[80] J. Y. Liu. Scanning transmission electron microscopy and its application to the study of nanoparticles and nanoparticle systems. *Journal of Electron Microscopy*, 54(3):251–278, 2005.

[81] Gordon Tatlock. *Introduction to Electron Optics*, pages 21–38. John Wiley & Sons, Ltd, 2011.

[82] Christoph Koch. *Determination of core structure periodicity and point defect density along dislocations*. Ph.d. thesis, 2002.

[83] Ian MacLaren and Quentin M. Ramasse. Aberration-corrected scanning transmission electron microscopy for atomic-resolution studies of functional oxides. *International Materials Reviews*, 59(3):115–131, 2014.

[84] P. Hartel, H. Rose, and C. Dinges. Conditions and reasons for incoherent imaging in STEM. *Ultramicroscopy*, 63(2):93–114, 1996.

[85] Ryo Ishikawa, Andrew R. Lupini, Scott D. Findlay, and Stephen J. Pennycook. Quantitative annular dark field electron microscopy using single electron signals. *Microscopy and Microanalysis*, 20(1):99–110, 2014.

[86] Young-Min Kim, Jun He, Michael D. Biegalski, Hailemariam Ambaye, Valeria Lauter, Hans M. Christen, Sokrates T. Pantelides, Stephen J. Pennycook, Sergei V. Kalinin, and Albina Y. Borisevich. Probing oxygen vacancy concentration and homogeneity in solid-oxide fuel-cell cathode materials on the subunit-cell level. *Nature Materials*, 11(10):888–894, 2012.

[87] Kangbo Lu, Erwan Sourty, and Joachim Loos. Annular dark-field scanning transmission electron microscopy (ADF-STEM) tomography of polymer systems. *Journal of Electron Microscopy*, 59(6):S39–S44, 2010.

[88] Deli Wang, Huolin L. Xin, Robert Hovden, Hongsen Wang, Yingchao Yu, David A. Muller, Francis J. DiSalvo, and Hector D. Abruna. Structurally ordered intermetallic platinum-cobalt core-shell nanoparticles with enhanced activity and stability as oxygen reduction electrocatalysts. *Nature Materials*, 12(1):81–87, 2013.

[89] Ryo Ishikawa, Andrew R. Lupini, Scott D. Findlay, Takashi Taniguchi, and Stephen J. Pennycook. Three-dimensional location of a single dopant with atomic precision by aberration-corrected scanning transmission electron microscopy. *Nano Letters*, 14(4):1903–1908, 2014.

[90] Chunming Huang, Sanfeng Wu, Ana M. Sanchez, Jonathan J. P. Peters, Richard Beanland, Jason S. Ross, Pasqual Rivera, Wang Yao, David H. Cobden, and Xiaodong Xu. Lateral heterojunctions within monolayer $MoSe_2$-WSe_2 semiconductors. *Nature Materials*, 13(12):1096–1101, 2014.

[91] P.W. Hawkes and J.C.H. Spence. *Science of Microscopy*. Springer, 2007.

[92] James M. LeBeau, Scott D. Findlay, Leslie J. Allen, and Susanne Stemmer. Standardless atom counting in scanning transmission electron microscopy. *Nano Letters*, 10(11):4405–4408, 2010.

[93] H. Kauko, C. L. Zheng, Y. Zhu, S. Glanvill, C. Dwyer, A. M. Munshi, B. O. Fimland, A. T. J. van Helvoort, and J. Etheridge. Compositional analysis of GaAs/AlGaAs heterostructures using quantitative scanning transmission electron microscopy. *Applied Physics Letters*, 103(23):232111, 2013.

[94] A. De Backer, A. De Wael, J. Gonnissen, G. T. Martinez, A. Beche, K. E. MacArthur, L. Jones, P. D. Nellist, S. Van Aert, and Iop. *Quantitative annular dark field scanning transmission electron microscopy for nanoparticle atom-counting: What are the limits?*, volume 644 of *Journal of Physics Conference Series*, page 012034. 2015.

[95] B. D. Esser, A. J. Hauser, R. E. A. Williams, L. J. Allen, P. M. Woodward, F. Y. Yang, and D. W. McComb. Quantitative STEM imaging of order-disorder phenomena in double perovskite thin films. *Physical Review Letters*, 117(17):176101, 2016.

[96] L. Jones and Iop. *Quantitative ADF STEM: acquisition, analysis and interpretation*, volume 109 of *IOP Conference Series-Materials Science and Engineering*, page 012008. 2016.

[97] G. T. Martinez, A. Rosenauer, A. De Backer, J. Verbeeck, and S. Van Aert. Quantitative composition determination at the atomic level using model-based high-angle annular dark field scanning transmission electron microscopy. *Ultramicroscopy*, 137:12–19, 2014.

[98] D. V. S. Rao, R. Sankarasubramanian, K. Muraleedharan, T. Mehrtens, A. Rosenauer, and D. Banerjee. Quantitative strain and compositional studies of $In_xGa_{1-x}As$ epilayer in a gaas-based pHEMT device structure by TEM techniques. *Microscopy and Microanalysis*, 20(4):1262–1270, 2014.

[99] S. Van Aert, J. Verbeeck, R. Erni, S. Bals, M. Luysberg, D. Van Dyck, and G. Van Tendeloo. Quantitative atomic resolution mapping using high-angle annular dark field scanning transmission electron microscopy. *Ultramicroscopy*, 109(10):1236–1244, 2009.

[100] Koji Kimoto, Toru Asaka, Takuro Nagai, Mitsuhiro Saito, Yoshio Matsui, and Kazuo Ishizuka. Element-selective imaging of atomic columns in a crystal using STEM and EELS. *Nature*, 450(7170):702–704, 2007.

[101] Na Li, Kui Du, Gang Liu, Yingpeng Xie, Guangmin Zhou, Jing Zhu, Feng Li, and Hui-Ming Cheng. Effects of oxygen vacancies on the electrochemical performance of tin oxide. *Journal of Materials Chemistry A*, 1(5):1536–1539, 2013.

[102] D. A. Muller, N. Nakagawa, A. Ohtomo, J. L. Grazul, and H. Y. Hwang. Atomic-scale imaging of nanoengineered oxygen vacancy profiles in $SrTiO_3$. *Nature*, 430(7000):657–661, 2004.

[103] Weigang Lu, Britain Bruner, Gilberto Casillas, Sergio Mejia-Rosales, Patrick J. Farmer, and Miguel Jose-Yacaman. Direct oxygen imaging in titania nanocrystals. *Nanotechnology*, 23(33):335706, 2012.

[104] C. Ophus, J. Ciston, J. Pierce, T. R. Harvey, J. Chess, B. J. McMorran, C. Czarnik, H. H. Rose, and P. Ercius. Efficient linear phase contrast in scanning transmission electron microscopy with matched illumination and detector interferometry. *Nature Communications*, 7:10719, 2016.

[105] H. Rose. Phase contrast in scanning transmission electron microscopy. *Optik*, 39(4):416–436, 1974.

[106] E. Okunishi, I. Ishikawa, H. Sawada, F. Hosokawa, M. Hori, and Y. Kondo. Visualization of light elements at ultrahigh resolution by STEM annular bright field microscopy. *Microscopy and Microanalysis*, 15:164–165, 2009.

[107] S. D. Findlay, N. Shibata, H. Sawada, E. Okunishi, Y. Kondo, and Y. Ikuhara. Dynamics of annular bright field imaging in scanning transmission electron microscopy. *Ultramicroscopy*, 110(7):903–923, 2010.

[108] R. Ishikawa, E. Okunishi, H. Sawada, Y. Kondo, F. Hosokawa, and E. Abe. Direct imaging of hydrogen-atom columns in a crystal by annular bright-field electron microscopy. *Nature Materials*, 10(4):278–281, 2011.

[109] Yuren Wen, Tongtong Shang, and Lin Gu. Analytical ABF-STEM imaging of li ions in rechargeable batteries. *Microscopy*, 66(1):25–38, 2017.

[110] S.J. Pennycook and P.D. Nellist. *Scanning Transmission Electron Microscopy: Imaging and Analysis*. Springer New York, 2011.

[111] L. J. Allen, A. J. D'Alfonso, B. Freitag, and D. O. Klenov. Chemical mapping at atomic resolution using energy-dispersive x-ray spectroscopy. *Mrs Bulletin*, 37(1):47–52, 2012.

[112] M. W. Chu, S. C. Liou, C. P. Chang, F. S. Choa, and C. H. Chen. Emergent chemical mapping at atomic-column resolution by energy-dispersive x-ray spectroscopy in an aberration-corrected electron microscope. *Physical Review Letters*, 104(19):196101, 2010.

[113] A. J. D'Alfonso, B. Freitag, D. Klenov, and L. J. Allen. Atomic-resolution chemical mapping using energy-dispersive x-ray spectroscopy. *Physical Review B*, 81(10):100101, 2010.

[114] G. Kothleitner, M. J. Neish, N. R. Lugg, S. D. Findlay, W. Grogger, F. Hofer, and L. J. Allen. Quantitative elemental mapping at atomic resolution using x-ray spectroscopy. *Physical Review Letters*, 112(8):085501, 2014.

[115] Ray F Egerton. *Electron Energy Loss Spectroscopy in the Electron Microscope*. Springer US, 3 edition, 2011.

[116] R. F. Klie, I. Arslan, and N. D. Browning. Atomic resolution electron energy-loss spectroscopy. *Journal of Electron Spectroscopy and Related Phenomena*, 143(23):105–115, 2005.

[117] M. Danaie, D. Kepaptsoglou, Q. M. Ramasse, C. Ophus, K. R. Whittle, S. M. Lawson, S. Pedrazzini, N. P. Young, P. A. J. Bagot, and P. D. Edmondson. Characterization of ordering in A-site deficient perovskite $Ca_{1-x}La_{2x}/3TiO_3$ using STEM/EELS. *Inorganic Chemistry*, 55(19):9937–9948, 2016.

[118] E. A. Mortsell, S. Wenner, P. Longo, S. J. Andersen, C. D. Marioara, and R. Holmestad. Elemental electron energy loss mapping of a precipitate in a multi-component aluminium alloy. *Micron*, 86:22–29, 2016.

[119] F. Q. Tao, C. Genevois, F. Q. Lu, X. J. Kuang, F. Porcher, L. J. Li, T. Rang, W. B. Li, D. Zhou, and M. Ailix. First 14-layer twinned hexagonal perovskite $Ba_{14}Mn_{1.75}Ta_{10.5}O_{42}$: Atomic-scale imaging of cation ordering. *Chemistry of Materials*, 28(13):4686–4696, 2016.

[120] Matthew L. Hand, Martin C. Stennett, and Neil C. Hyatt. Rapid low temperature synthesis of a titanate pyrochlore by molten salt mediated reaction. *Journal of the European Ceramic Society*, 32(12):3211–3219, 2012.

[121] Warwick Microscopy webpage. `http://www2.warwick.ac.uk/fac/sci/physics/research/condensedmatt/microscopy/em-rtp/instruments/jeol_arm200f/`, .

[122] B. Schaffer. Stackbuilder (on image update) plugin for digital micrograph. `http://digitalmicrograph-scripting.tavernmaker.de/HowToScript_index.htm`.

[123] James M. LeBeau and Susanne Stemmer. Experimental quantification of annular dark-field images in scanning transmission electron microscopy. *Ultramicroscopy*, 108(12):1653–1658, 2008.

[124] Andreas Rosenauer, Katharina Gries, Knut Mller, Angelika Pretorius, Marco Schowalter, Adrian Avramescu, Karl Engl, and Stephan Lutgen. Measurement of specimen thickness and composition in using high-angle annular dark field images. *Ultramicroscopy*, 109(9):1171–1182, 2009.

[125] Oxford Instruments webpage. https://www.oxford-instruments.com/products/microanalysis/energy-dispersive-x-ray-systems-eds-edx/eds-for-tem, .

[126] Gatan Microscopy Suite Software. http://www.gatan.com/products/tem-analysis/gatan-microscopy-suite-software.

[127] R. F. Egerton, F. Wang, M. Malac, M. S. Moreno, and F. Hofer. Fourier-ratio deconvolution and its bayesian equivalent. *Micron*, 39(6):642–647, 2008.

[128] Huai-Ruo Zhang, Ray F. Egerton, and Marek Malac. Local thickness measurement through scattering contrast and electron energy-loss spectroscopy. *Micron*, 43(1):8–15, 2012.

[129] T. Malis, S. C. Cheng, and R. F. Egerton. EELS log-ratio technique for specimen-thickness measurement in the TEM. *Journal of Electron Microscopy Technique*, 8(2):193–200, 1988.

[130] A. Rosenauer and M. Schowalter. *STEMSIM-a New Software Tool for Simulation of STEM HAADF Z-Contrast Imaging*, volume 120 of *Springer Proceedings in Physics*, pages 169–172. 2008.

[131] B. D. Forbes, A. J. D'Alfonso, S. D. Findlay, D. Van Dyck, J. M. LeBeau, S. Stemmer, and L. J. Allen. Thermal diffuse scattering in transmission electron microscopy. *Ultramicroscopy*, 111(12):1670–1680, 2011.

[132] R. F. Loane, P. Xu, and J. Silcox. Thermal vibrations in convergent-beam electron diffraction. *Acta Crystallographica Section A*, 47(3):267–278, 1991.

[133] T. Mehrtens, K. Muller, M. Schowalter, D. Z. Hu, D. M. Schaadt, and A. Rosenauer. Measurement of indium concentration profiles and segregation efficiencies from high-angle annular dark field-scanning transmission electron microscopy images. *Ultramicroscopy*, 131:1–9, 2013.

[134] Andreas Rosenauer, Thorsten Mehrtens, Knut Mueller, Katharina Gries, Marco Schowalter, Parlapalli Venkata Satyam, Stephanie Bley, Christian Tessarek, Detlef Hommel, Katrin Sebald, Moritz Seyfried, Juergen Gutowski, Adrian Avramescu, Karl Engl, and Stephan Lutgen. Composition mapping in ingan by scanning transmission electron microscopy. *Ultramicroscopy*, 111(8): 1316–1327, 2011.

[135] Marco Schowalter, Ingo Stoffers, Florian F. Krause, Thorsten Mehrtens, Knut Mueller, Malte Fandrich, Timo Aschenbrenner, Detlef Hommel, and Andreas Rosenauer. Influence of static atomic displacements on composition quantification of AlGaN/GaN heterostructures from HAADF-STEM images. *Microscopy and Microanalysis*, 20(5):1463–1470, 2014.

[136] V. Grillo, E. Carlino, and F. Glas. Influence of the static atomic displacement on atomic resolution Z-contrast imaging. *Physical Review B*, 77(5):054103, 2008.

[137] D. Hull and D. J. Bacon. *Chapter 1 - Defects in Crystals*, pages 1–20. Butterworth-Heinemann, Oxford, 2011.

[138] M. J. Hytch, E. Snoeck, and R. Kilaas. Quantitative measurement of displacement and strain fields from HREM micrographs. *Ultramicroscopy*, 74(3): 131–146, 1998.

[139] J. Kioseoglou, G. P. Dimitrakopulos, P. Komninou, T. Karakostas, and E. C. Aifantis. Dislocation core investigation by geometric phase analysis and the dislocation density tensor. *Journal of Physics D-Applied Physics*, 41(3): 035408, 2008.

[140] Y. Wang, X. P. Liu, and G. W. Qin. Investigation of misfit dislocations in alpha-Fe_2O_3/alpha-Al_2O_3 interface by geometric phase analysis and dislocation density tensor analysis. *Materials Characterization*, 106:308–316, 2015.

[141] J. F. Nye. Some geometrical relations in dislocated crystals. *Acta Metallurgica*, 1(2):153–162, 1953.

[142] S. Kret, P. Dluzewski, P. Dluzewski, and E. Sobczak. Measurement of dislocation core distribution by digital processing of high-resolution transmission electron microscopy micrographs: a new technique for studying defects. *Journal of Physics-Condensed Matter*, 12(49):10313–10318, 2000.

[143] J. J. P. Peters, R. Beanland, M. Alexe, J. W. Cockburn, D. G. Revin, S. Y. Y. Zhang, and A. M. Sanchez. Artefacts in geometric phase analysis of compound materials. *Ultramicroscopy*, 157:91–97, 2015.

[144] J. J. P. Peters. Strain++. `http://jjppeters.github.io/Strainpp/`.

[145] E. Eberg, A. T. J. van Helvoort, R. Takahashi, M. Gass, B. Mendis, A. Bleloch, R. Holmestad, and T. Tybell. Electron energy loss spectroscopy investigation

of Pb and Ti hybridization with O at the $PbTiO_3/SrTiO_3$ interface. *Journal of Applied Physics*, 109(3):034104, 2011.

[146] E. Stoyanov, F. Langenhorst, and G. Steinle-Neumann. The effect of valence state and site geometry on Ti L_3,L_2 and O-K electron energy-loss spectra of Ti_xO_y phases. *American Mineralogist*, 92(4):577–586, 2007.

[147] J. M. Zhang, A. Visinoiu, F. Heyroth, F. Syrowatka, M. Alexe, D. Hesse, and H. S. Leipner. High-resolution electron energy-loss spectroscopy of $BaTiO_3/SrTiO_3$ multilayers. *Physical Review B*, 71(6):064108, 2005.

[148] L. A. Grunes, R. D. Leapman, C. N. Wilker, R. Hoffmann, and A. B. Kunz. Oxygen-K near-edge fine-structure - an electron-energy-loss investigation with comparisons to new theory for selected 3D transition-metal oxides. *Physical Review B*, 25(12):7157–7173, 1982.

[149] M. Herrera, Q. M. Ramasse, D. G. Morgan, D. Gonzalez, J. Pizarro, A. Yáñez, P. Galindo, R. Garcia, M.-H. Du, S. B. Zhang, M. Hopkinson, and N. D. Browning. Atomic scale high-angle annular dark field STEM analysis of the N configuration in dilute nitrides of GaAs. *Physical Review B*, 80:125211, 2009.

[150] Y. Tokiwa, T. Yamashita, M. Udagawa, S. Kittaka, T. Sakakibara, D. Terazawa, Y. Shimoyama, T. Terashima, Y. Yasui, T. Shibauchi, and Y. Matsuda. Possible observation of highly itinerant quantum magnetic monopoles in the frustrated pyrochlore $Yb_2Ti_2O_7$. *Nature Communications*, 7:10807, 2016.

[151] Thermal conductivity of common materials and gases. `http://www.engineeringtoolbox.com/thermal-conductivity-d_429.html`.

[152] A. Mergen. Dislocations in BZS and PMN pyrochlores. *Crystallography Reports*, 46(5):810–812, 2001.

[153] D. Hull and D. J. Bacon. *Chapter 5 - Dislocations in Face-centered Cubic Metals*, pages 85–107. Butterworth-Heinemann, Oxford, 2011.

[154] M.N. Shetty. *Dislocations and mechanical behaviour of materials*. PHI Learning, 2013.

[155] Y. T. Zhu, X. L. Wu, X. Z. Liao, J. Narayan, L. J. Kecskes, and S. N. Mathaudhu. Dislocation-twin interactions in nanocrystalline fcc metals. *Acta Materialia*, 59(2):812–821, 2011.

[156] N. Jiang, S. Ye, and J. R. Qiu. Electron energy-loss spectroscopy study of Yb doped ZnO. *Journal of Applied Physics*, 108(8):083535, 2010.

[157] A. Gorschluter, R. Stiller, and H. Merz. Dipole forbidden f-f excitation in ytterbium oxide. *Surface Science*, 251:272–275, 1991.

[158] G. G. Fuentes, I. G. Mancheno, F. Balbas, C. Quiros, J. F. Trigo, F. Yubero, E. Elizalde, and J. M. Sanz. Dielectric properties of Ti, TiO_2 and TiN from 1.5 to 60 ev determined by reflection electron energy loss spectroscopy (REELS) and ellipsometry. *Physica Status Solidi a-Applied Research*, 175(1):429–436, 1999.

[159] Gatan EELS Atlas. EEL spectra for Yb_2O_3 thin film. `http://www.eels.info/atlas/ytterbium`, .

[160] Gatan EELS Atlas. EEL spectra for TiO_2 thin film. `http://www.eels.info/atlas/titanium`, .

[161] M. Ruminy, L. Bovo, E. Pomjakushina, M. K. Haas, U. Stuhr, A. Cervellino, R. J. Cava, M. Kenzelmann, and T. Fennell. Sample independence of magnetoelastic excitations in the rare-earth pyrochlore $Tb_2Ti_2O_7$. *Physical Review B*, 93(14):144407, 2016.

[162] H. M. Revell, L. R. Yaraskavitch, J. D. Mason, K. A. Ross, H. M. L. Noad, H. A. Dabkowska, B. D. Gaulin, P. Henelius, and J. B. Kycia. Evidence of impurity and boundary effects on magnetic monopole dynamics in spin ice. *Nature Physics*, 9(1):34–37, 2013.